The Dissertation Committee for Jagruti Jagadish Pattadkal certifies that this is the approved version of the following Dissertation:

Computations In The Early Visual System In The Mouse

Committee:

Nicholas J. Priebe, Supervisor

Richard Aldrich

Ila Fiete

Alexander Huk

J. Anthony Movshon

Computations In The Early Visual System In The Mouse

by

Jagruti Jagadish Pattadkal

Dissertation

Presented to the Faculty of the Graduate School of

The University of Texas at Austin

in Partial Fulfillment

of the Requirements

for the Degree of

Doctor of Philosophy

The University of Texas at Austin

August 2019

To my family and friends

Acknowledgements

Over the time of this thesis, I have been very fortunate to receive the love and support of many people and I wish I were more eloquent to satisfactorily express my thanks to all. Here is an attempt to count my blessings.

This work and everything else I have worked on these past few years could not have been possible without the wonderful mentorship of Nicholas. It has been a real privilege to be his student and he is an inspiration in and outside of science. Since the beginning of my time in his lab, he has really encouraged me to be open in pursuing research questions and provided several opportunities to do so. As a consequence, I have had the pleasure to work on a variety of questions, including many that did not become a part of this thesis, and I am thankful for all that experience. A side effect of doing many experiments is that many of them tend to fail. At all those times, he is ready with his unique sense of humor to get a laugh out of us, and I am thankful for all those jokes, even the ones I didn't laugh at. I am also thankful for his patience with my mistakes as I am slowly fumbling my way through science, for his enthusiasm about ideas and data, and above all for looking out for me in and out of the lab. I hope this thesis and my work in the future makes you proud, if only a little bit.

I have also had the pleasure to be surrounded by a great group of people in this lab. Much of my work during my time has been on the marmosets and especially for that, I want to thank Allison Laudano. She has been a great source of help with all the animal care and thanks to her, the only things I need to worry about is me doing the experiments and surgeries, she manages the rest. I would also like to thank Carrie Barr, Devon Greer and Chris Lee for everything they do

or did to facilitate the experiments. It saves me many hours and I am very thankful for all your help. A special thanks to my office mates and friends, Veronica and Dylan, who are always ready to lend an ear to everything I say, no matter the content. I also want to thank Jason and Baowang, for all their support and advice. Thanks to all of you for always being ready to help and for making the lab a fun place. I also want to mention the past students in the lab, Ben Scholl, Andrew TAN, Sari Andoni. They have taught me my first mouse surgeries and were there to cheer for me when I got my first cell. I am grateful for everything they have taught me and Ben especially, for being a co-conspirator in some of the projects. I have truly enjoyed working with you all.

I am very grateful to my committee, Rick Aldrich, Ila Fiete, Alex Huk and Tony Movshon, for their advice, time and interest in my work. I have learnt a lot from you, and you are all a big source of inspiration to me. I also want to thank all my collaborators. David Hansel and Carl van Vreeswijk have been long-standing collaborators and our work with them has helped to shape my perspective on mouse visual cortex computations. My more recent work with the marmosets has provided me with the opportunity to explore the basis for computations at the neuronal population level. Boris Zemelman's expertise in molecular tools is crucial for me to be able do these experiments and Ila's advice is helping us to navigate through these data. Guillaume Masson's advice has also been very useful in setting up the ocular following paradigms for the marmosets. I also want to thank Alex Huk and his lab crew for generously collecting part of the data for another piece of project studying marmoset smooth pursuit behavior.

I am also thankful to my rotation labs in the program, with Eyal Seidemann and Alex Huk, I had a great time learning about vision in my short stints in both

labs. A big thank you to the Institute for Neuroscience for creating such a wonderful welcoming and encouraging environment for all of us to thrive in. I also want to thank all my batchmates, for being such great company through grad school.

I am thankful to all the administrative staff in the program, especially Krystal Phu and Chris Weatherly for their efficient support. I am also thankful for the services of the machine shop at UT, many of the experiments I am able to do in the marmosets would not have been possible without the tools they can generate for us.

I am very grateful to have received the generous support of HHMI international predoctoral fellowship as well as support from UT Graduate School and the Center for Learning and Memory in various forms during my time as a graduate student.

I am indebted to my undergraduate institute IISER, Pune, for creating in me a love for scientific research. I am especially grateful to my undergrad mentor, Dr. Aurnab Ghose and Prof. Subhedar, for encouraging and guiding my interest in neuroscience.

Finally, I want to thank all my friends and family for their continued support, company and encouragement, without which this would not have been possible. All members of The Herd, I am really glad to have your years of friendship and it's a constant source of joy and support to me. To my family, especially my parents and my sister, no amounts of words can express my thanks. They have encouraged me to be better at what I do from a young age and stood by my choices, and I just want to say thanks for everything you do.

Abstract

Computations In The Early Visual System In The Mouse

Jagruti Jagadish Pattadkal, Ph. D.

The University of Texas at Austin, 2019

Supervisor: Nicholas J. Priebe

In this dissertation, I have explored the mechanisms underlying the selectivity of different visual features in the mouse. I have compared these mechanisms to the canonical mechanisms for extracting these features. In chapter 2, I have demonstrated existence of nonclassical receptive fields in which the orientation preference can depend on the spatial frequency, in the mouse visual cortex. I have compared the experimental data with a model based on random connectivity between cells which predicts existence of such receptive fields. In chapter 3, I have studied the input differences between V1 neurons with varying degrees of linearity in spatial summation. I have demonstrated evidence of connectivity which deviates from the standard hierarchical connectivity model. I show that nonlinear cells in the mouse V1 can receive thalamic input which can itself be nonlinear and also orientation selective. In chapter 4, I have studied the development of binocular disparity tuning and using monocular deprivation. I show that disparity selectivity in the mouse is reduced following contralateral eye deprivation during critical period. This effect is due to a disruption of existing disparity selectivity in the circuit following deprivation, as we observe no

difference in degree of selectivity between adult animals and young mice before critical period. This disruption may be due to formation of new inputs which disrupt the matching between left and right eye existing inputs. We provide evidence for this by demonstrating a reduction in spatial acuity for the open eye inputs following deprivation. Across all of these studies, I demonstrate multiple instances in which the mouse pathways differ from the classical early visual pathways. But I also find evidence for a distinctive connectivity, similar to the classical models. My thesis highlights the diversity in circuit computations which leads to the processing outcomes that are shared across the mammalian species.

Table of Contents

List of Tables

List of Figures

Chapter 1: Introduction

A fundamental goal of systems neuroscience is to be able to describe the processing of sensory information, and the means by which it is used to guide behavior. In the visual system, the representation of our visual environment is systematically transformed in a hierarchical fashion. The focus of the early visual system, as deduced from the response selectivity of individual neurons in different stages of the circuit, is to decompose complex images into basic components. These basic components include contrast, orientation, motion, texture, and depth, the representations of which are used by successive stages to generate more complex representations. The response to the incoming stimulus, influenced by context, is then passed on to downstream visual areas which build on these representations.

In the case of visual system of carnivores and primates, the compartmentalization of visual functions provides an opportunity to study the mechanisms that underlie these visual transformations. Indeed, the identification of these transformations and means by which they are carried out have historically been described in species like cats and macaques (Hubel and Wiesel, 1962, 1977). As more and more species are being explored, the generality of the functional hierarchy of visual processing has been questioned. Some functional aspects are conserved across the different mammalian species. For example, orientation selectivity is observed in a wide range of species, as are motion and

depth sensitivity (Heimel et al., 2005; Niell and Stryker, 2008; Van Hooser et al., 2013; Scholl et al., 2017).

While these functional properties exist across species, determining whether common mechanisms underlie their emergence is unclear. Different animals across the mammalian evolutionary tree have developed distinct circuits in response to the evolutionary pressures each species has faced. These differences may lead to the adoption of different circuit schemes to implement the same computations. In this dissertation, I study the circuit computations of two specific visual features: orientation selectivity and binocular disparity selectivity. The focus of this dissertation is on the mouse visual system and I explore the differences in the mechanisms that underlie computations that may arise from the configuration of the mouse visual system. The reason to study these computations in the mouse is because of the availability of genetic tools to manipulate mouse circuits. This makes the system particularly amenable to studying the mechanisms underlying various computations. The mouse cortex is also accessible to performing population scale recordings with imaging, and this allows us to study the diversity in the responses and compare responses across the population simultaneously. It is also possible to do these measurements at different stages of development, and perform developmental manipulations, like monocular deprivation, in these animals. Given all these advantages, and the existence of some feature selectivities, which are shared with carnivores and primates, the mouse system is well suited to compare the implementation of these computations. In chapter 2 of the thesis, I look at the differences in

orientation selectivity of mice in comparison to the classical models and suggest an alternate model and provide some experimental evidence in support of it. In chapter 3, I study the means of generating simple and complex cells in the mouse visual pathway and how they differ from the classical patterns observed in carnivores. In chapter 4, I take advantage of the distinct features of the mouse visual pathway to address specific questions about the development of cortical binocularity in young animals. Below is an introduction to these issues before the main chapters.

EMERGENCE OF ORIENTATION SELECTIVITY

The classical model of orientation selectivity

Visual processing begins in the retina, where visual information is initially transduced by photoreceptors. The output of the retina, retinal ganglion cells, have circular receptive fields with center surround organization in cats (Kuffler, 1953) and primates. Based on sensitivity to a visual stimulus being turned on or off, these cells are classified as ON-center or OFF-center. Retinal ganglion cells project to the lateral geniculate nucleus (LGN) of the thalamus. The basic scheme of circular center/surround, ON/OFF receptive fields is maintained in LGN relay cells (Hubel and Wiesel, 1961). The LGN relay cells then project to the input layer of primary visual cortex (V1), layer 4, where orientation selectivity first appears in cat visual cortex (Hubel and Wiesel, 1962), Hubel and Wiesel proposed a model for the emergence of orientation selectivity in which the convergence of ON and OFF thalamic inputs onto cortical cells generates an elongated receptive field with spatially offset ON and OFF regions. These cells

with oriented receptive fields in V1 are termed simple cells, as they exhibit offset ON and OFF regions and the shape of their receptive field determines their preference for orientation. Experimental support for this model comes from studies showing a match of receptive fields of thalamic relay cells that converge onto target simple cells (Bullier et al., 1982; Reid and Alonso, 1995; Alonso et al., 2001). The ON-OFF organization of inputs not only contributes to the orientation selectivity of single cells but can also lead to columnar organization (Jin et al., 2011).

Hubel and Wiesel also described another class of cells called complex cells, which also exhibit orientation selectivity. The difference between these two functional cell classes, simple cells and complex cells, is based on the relative overlap of ON and OFF receptive subfields. Simple cells have segregated ON and OFF subfields, this causes them to have a selectivity for the location of the stimulus within the receptive field (spatial phase). Complex cells have overlapping ON and OFF subfields which gives them spatial invariance. The majority of the cells in the input layer 4 of cat V1 are simple cells, consistent with the Hubel and Wiesel hierarchical model. The feedforward connectivity model that Hubel and Wiesel also proposed a circuit to explain the emergence of complex receptive fields. These were generated in the model by summing inputs from simple cells with same orientation preference but different spatial preference, thereby generating a spatially invariant responses that remain orientation selective, as observed in complex cells. Using a linear systems analysis approach has demonstrated that complex cells receptive fields may be

decomposed into multiple linear subfields, consistent with hierarchical model (Movshon et al., 1978b, a). Further evidence for this hierarchy was also provided by demonstrating that monosynaptic connections exist from simple cells in layer 4 to complex cells (Alonso and Martinez, 1998) and that inactivation of layer 4 simple cells also silenced the complex cells (Martinez and Alonso, 2001).

This hierarchical scheme of connectivity proposed that simple and complex cells are two distinct levels of processing in the cortex on the basis of distinct synaptic input. The connectivity pattern, however, is not so distinct between simple and complex cells. Mechler and Ringach, 2002, presented a model where a unimodal input distribution could generate the dichotomy in spike responses to make simple and complex cells, when followed by a rectification (Mechler and Ringach, 2002). Priebe et al 2004 experimentally confirmed that the dichotomy between simple and complex cells arose from a unimodal membrane potential response distribution indicating that the difference in simple and complex cells is one of degree instead of class (Priebe et al., 2004).

Under the hierarchical connectivity model, the role of feedforward thalamic inputs is to generate the orientation tuning responses with linear spatial summation, as observed in simple cells. The role of recurrent cortical inputs is to maintain this orientation selectivity by summing across orientation selective inputs and generate spatial invariance, as observed in complex cells. Cortical inactivation experiments have been used to dissect the role of feedforward thalamic inputs. Cortical cooling or electrical shock experiments demonstrate that

the orientation selectivity of the thalamic input matches the selectivity when the cortex is intact. Most V1 cells that receive monosynaptic input from the LGN are simple cells. A small fraction of complex cells, however, has been reported to receive direct monosynaptic LGN inputs (Ferster and Lindström, 1983; Hirsch et al., 1998). How these inputs onto complex cells contribute to the orientation selectivity of the recipient cortical cells remains unknown. Models have been used to explore the regime where both simple and complex cells receive thalamic inputs, but recurrent connections alone are responsible for complex receptive fields. These models utilize a continuum of thalamic and recurrent connections and increasing the recurrent connections lead to cells becoming less simple and more complex (Chance et al., 1999; Tao et al., 2004; Yunzab et al., 2019).

Orientation selectivity in mice

Neurons in mouse V1 also display orientation selectivity, though it is weaker than observed in primates and carnivores (Drager, 1975; Scholl et al., 2013). Within the rodent visual cortex, orientation selective cells are not organized in a columnar fashion but show a salt and pepper arrangement (Ohki et al., 2005), but it is possible that these neurons display some organization on a smaller local scale (Ringach et al., 2016; Scholl et al., 2016). The lack of large-scale columnar organization, however, does not imply a lack of specificity in recurrent connections. Multiple studies based on simultaneous intracellular recordings (Ko et al., 2011; Cossell et al., 2015) as well as electron microscopy (Lee et al., 2016) have demonstrated a higher connection probability between excitatory cells with similar response profiles. In mice both simple and complex

cells are distributed across cortical layers (Niell and Stryker, 2008; Van den Bergh et al., 2010), whereas in carnivores or primates the functional cell classes vary by layer (Ringach et al., 2002; Martinez et al., 2005).

The basis for mouse orientation selectivity may also rely on a functionally distinct set of thalamic inputs than that observed in cats and primates. Thalamic relay cells in the mouse LGN exhibit a diverse set of selectivities, including orientation and direction selectivity (Piscopo et al., 2013; Scholl et al., 2013) whereas only a weak degree of orientation and direction selectivity exists in the LGN of cats and primates (Daniels et al., 1977; Lee et al., 1979; Scholl et al., 2013). We know that loss of directionally tuned retinal ganglion cells leads to changes in the representation of motion in V1 (Hillier et al., 2017), demonstrating that selectivity of LGN relay cells impacts the response selectivity of some V1 cells. It is possible therefore possible for orientation-tuned thalamic cells to pass on their selectivity to their V1 targets. Experimental observations of the tuning of thalamic boutons or axons in cortical layers have reached opposite conclusions. One study, by Sun et al, 2016, imaged thalamic axon boutons within layer 4 of the V1 and found about half of them to have significant orientation and direction tuning (Sun et al., 2016). Another study, by Kondo and Ohki, 2016, imaging LGN axons and found layer 4 projecting axons to be less orientation tuned (Kondo and Ohki, 2016). Finally, another study examined the aggregate thalamic inputs following optogenetic cortical silencing and concluded that inputs to layer 4 simple cells could not arise from individually tuned thalamic cells (Lien and

Scanziani, 2013). The issue about contribution of orientation selective LGN cells to cortical orientation selectivity thus remains unsettled.

Moving further up in the hierarchy, the contribution of recurrent inputs has been shown to faithfully match the thalamic information, with thalamic inputs providing on average one third of the total excitation (Li et al., 2013; Lien and Scanziani, 2013). Multiple mechanisms may be contributing to the orientation and direction tuning within the mouse V1, some of which may inherit tuning from the LGN while others may involve de novo generation of selectivity within the cortex. These studies indicate that there may exist connectivity schemes different than the one suggested by Hubel and Wiesel to generate orientation tuning in the mouse V1.

In chapter 2 of this dissertation, I will analyze predictions of one such alternate connectivity model that may underlie orientation tuning in mice. Hansel and van Vreeswijk, 2012, had presented a model where orientation selectivity in L2/3 could be inherited from L4 even if the recurrent and feedforward (L4 to L2/3) connections were random and not selective for the orientation (Hansel and van Vreeswijk, 2012). Their work demonstrated that random connectivity did not disrupt orientation tuning that already exists within the network. They have now extended the model which can also explain emergence of orientation selectivity in the network based on random connectivity from non-selective LGN cells and recurrent inputs. The model makes specific prediction for orientation-tuned

responses of mouse V1 cells. I test these predictions experimentally and compare them to the model expectation in chapter 2.

Given that the connections within the mouse cortex are not as functionally organized, the mechanisms underlying the transformation from simple to complex cell receptive fields may be distinct from that reported in carnivores and primates. If the bulk of LGN inputs to the cortex are individually untuned, then in order to construct spatially invariant orientation tuned complex cell would require recurrent connections from simple cells with same orientation preference but different spatial preferences. On the other hand, if cortical cells are able to receive inputs from tuned LGN cells, it is possible to construct a complex receptive field based on LGN inputs. In chapter 3 of this thesis, I analyze the contribution of thalamic and recurrent inputs to the generation of simple and complex cells in mouse V1, combining intracellular recordings with optogenetics.

DEVELOPMENT OF BINOCULAR INTEGRATION

Experience dependent plasticity

Studying the development of selectivity can often inform us about the circuits compute these features. One classic example of such experience-dependent plasticity is the ocular dominance plasticity during the critical period. Neurons in the visual cortex of animals with receptive field in the binocular zone can receive inputs from both eyes to varying degrees. The ocular dominance (OD), a measure of the relative strength of inputs a neuron receives from the two eyes, normally peaks near 0, indicating that many neurons receive balanced

inputs from the eyes (Wiesel and Hubel, 1963a; Wiesel and Hubel, 1965; Hubel et al., 1977). The distribution of OD can be perturbed using monocular deprivation (MD) during the critical period. Following MD of one eye, the OD shifts away from input from those eyes and moves towards being dominated by inputs from the open eye (Wiesel and Hubel, 1963b; Hubel and Wiesel, 1970; Hubel et al., 1977). MD not only shifts the OD distribution toward more monocularity, but also leads to a loss in binocular disparity selectivity of these neurons (Sclar et al., 1986). Disparity tuning is the ability of neurons to be sensitive to spatial offsets between retinal images of the two eyes (Pettigrew et al., 1968) and it can be used to infer depths of objects in the world (Uka and DeAngelis, 2004). This property relies on inputs from both eyes for appropriate integration. Whereas ocular dominance is a metric that measures inputs from each eye, since it is measured monocularly, it does not test how the inputs from the two eyes are integrated.

Looking at the effects of MD on binocular disparity tuning provides us information about how the change in circuits alters the binocular integration. In case of cats and primates, loss of binocularity following MD, as measured with OD, also leads to a loss in binocular disparity tuning of these neurons (Sclar et al., 1986). This loss of disparity tuning may reflect the absence of input from the closed eye, or a disruption of the spatial structure of this binocular input required for disparity measurements. We will take advantage of the distinct structure of the binocularity in mice to address how MD disrupts binocular integration.

Binocularity in mouse V1

The ocular dominance distribution has also been measured across binocular zone neurons in mouse V1. In contrast to carnivores and primates this distribution is biased to contralateral eye inputs (Gordon and Stryker, 1996). When exposed to contralateral eye MD during the critical period, the OD shifts away from contralateral eye inputs and towards ipsilateral eye inputs causes a paradoxical increase in binocularity, as assayed by OD (Gordon and Stryker, 1996; Hanover et al., 1999). We used MD in mice to study how OD and disparity selectivity are related. If the degree of disparity selectivity depends on the relative weight of inputs from the two eyes, MD in mice should increase disparity selectivity. On the other hand, disparity selectivity in mice may depend on a precise spatial alignment of inputs coming from the two eyes. I demonstrate that despite the fact that MD increases binocularity, it is accompanied by a decline in disparity selectivity, indicating that the weight of input between the two eyes is not as critical as the spatial alignment of those inputs.

Chapter 2: Emergent orientation selectivity from random networks in mouse visual cortex[1] [2]

SUMMARY

The connectivity principles underlying the emergence of orientation selectivity in primary visual cortex (V1) of mammals lacking an orientation map (such as rodents and lagomorphs) are poorly understood. We present a computational model in which random connectivity gives rise to orientation selectivity that matches experimental observations. The model predicts that mouse V1 neurons should exhibit intricate receptive fields in the two-dimensional frequency domain, causing a shift in orientation preferences with spatial frequency. We find evidence for these features in mouse V1 using calcium imaging and intracellular whole-cell recordings.

INTRODUCTION

Since its initial description by Hubel and Wiesel (Hubel and Wiesel, 1962), orientation selectivity has served as a platform for studying neocortical computations (Priebe and Ferster, 2012). V1 neurons in primates and carnivores are characterized not only by their preference for the orientation of bars or edges, but also that the preference for a bar or edge of a specific orientation is invariant to the spatial structure of the object displayed. For example, a V1 neuron which

[1]The model presented in this chapter is the work of David Hansel, Carl van Vreeswijk and German Mato. It is presented in this thesis for completeness. Author claims no credit for the model aspect of the chapter.

[2]Published in Cell Reports (2018):
Emergent orientation selectivity from random networks in mouse visual cortex
Pattadkal J. J., Mato G., van Vreeswijk, Priebe N. J.*, and Hansel D. H.*
*: contributed equally

responds best to a vertical orientation should maintain that orientation preference despite changes in the width or movement of a presented bar (De Valois et al., 1982; Webster and De Valois, 1985; Jones et al., 1987).

Orientation selectivity emerges in V1 of primates and carnivores where a functional organization for this selectivity is also observed: neurons are organized in a columnar fashion with shared orientation preference across cortical layers and smooth changes in selectivity along the V1 surface (Hubel and Wiesel, 1977). This functional architecture is the product of the spatial arrangement of ON and OFF thalamocortical inputs that innervate V1 (Kremkow et al., 2016; Lee et al., 2016a) and of the vertical bias of intracortical connectivity (Song et al., 2005). These spatially offset ON and OFF afferents converge on individual V1 neurons to generate receptive fields that are orientation-tuned (Alonso et al., 2001) and well-described by Gabor functions (Jones and Palmer, 1987) (Fig. 2.1A).

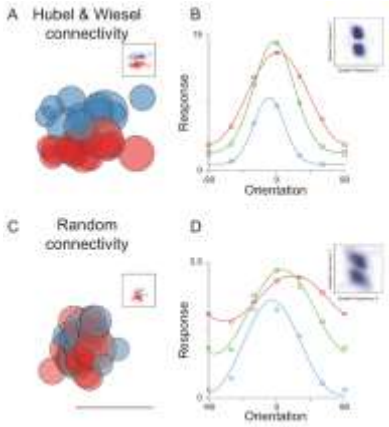

Figure 2.1: Receptive fields, random connectivity, spatial frequency tuning and orientation tuning.

A. Hubel and Wiesel connectivity in which ON (red) and OFF (blue) thalamocortical afferents, with spatial receptive fields indicated by each circle, converge onto a neuron in primary visual cortex. The summation of these afferent receptive fields generates a Gabor like receptive field in visual cortex (inset). B. Orientation preference does not change with spatial frequency for such receptive fields. Tuning curves of the temporal modulation of the response for tow (red) medium (green) and high spatial frequencies are plotted. In frequency space these receptive fields maintain a peak response at a consistent angle that points toward the origin at the midpoint of the graph (inset). C. Random connectivity from the LGN in which ON and OFF thalamocortical neurons with similar spatial receptive fields converge on cortical neurons also generates orientation selectivity in the temporal modulation of the response. The summation of LGN neuron receptive fields shows oriented profiles (inset). Scale bar indicates 35 degrees. D. Orientation preference shifts for random connectivity as spatial frequency changes. Orientation tuning curves are plotted as in B. In frequency space these receptive fields tilt in a manner that does not project back to the origin. (Fig 2.1 continued)

Such a functional architecture for orientation selectivity, however, is not common to all mammals: V1 of rodents and lagomorphs lack it but their neurons are still orientation selective (Drager, 1975; Murphy and Berman, 1979; Metin et al., 1988; Girman et al., 1999). This raises the question of what connectivity rules guide afferent and intracortical circuitry to generate orientation selectivity in mammals that lack a functional architecture for orientation selectivity (Ohki and Reid, 2007).

We recently showed in a model of rodent V1 that layer 2/3 can inherit orientation selectivity from orientation selective neurons in layer 4 even if recurrent as well as feedforward (L4 to L2/3) connectivity is random (Hansel and van Vreeswijk, 2012). In this model the L2/3 network operates in a ‘balanced’ regime (van Vreeswijk and Sompolinsky, 1996, 1998), in which excitatory and

inhibitory inputs, are both strong, and roughly cancel each other (Hansel and van Vreeswijk, 2012; Pehlevan and Sompolinsky, 2014).

In this report we address the question of whether orientation selectivity can emerge in rodent V1 from random connectivity. We present a strongly recurrent model of the rodent V1 network in which neurons receive inputs from randomly chosen non-selective LGN cells. The model does not necessitate sparse connectivity to generate selectivity, as is required in previous random network-based models of orientation tuning (von der Malsburg, 1973; Soodak, 1987; Ringach, 2004). Remarkably, orientation selectivity emerges in this network despite the lack of a Gabor like structure of the thalamocortical input with well segregated ON and OFF subfields. Furthermore, orientation selectivity in this network is robust to changes in the number of inputs. A key prediction of this model is that the orientation selectivity of V1 neurons may vary with the spatial content of the presented stimulus (Miller, 2016). It thus predicts that in mouse V1 neuron receptive fields in the frequency domain are intricate, containing dependencies between orientation and spatial frequency, in stark contrast to observations made in primates and carnivores, and predictions of Gabor receptive fields (De Valois et al., 1982; Webster and De Valois, 1985; Jones et al., 1987). To test these predictions, we quantified in mouse V1 the degree to which orientation preference is linked to the stimulus spatial frequency using a combination of electrophysiological and imaging measurements. In agreement with our model we found that orientation preference depends strongly on spatial frequency.

RESULTS

To contrast different circuitry that could give rise to cortical orientation selectivity we constructed two model V1 neurons that receive input from the thalamus. In one model the V1 neuron receives ON and OFF thalamic inputs that are sampled on the basis of a Gabor filter: ON and OFF inputs have spatial preferences elongated along the preferred orientation axis and are spatially segregated (Fig. 2.1A). The temporally modulated component (F1) of the response is largest to horizontally oriented drifting gratings regardless of the spatial frequency (Fig. 2.1B). We also constructed a model V1 neuron that receives ON and OFF inputs with nearby spatial preferences (dispersion SD, 7 degrees), which are randomly intermixed (Fig. 2.1C). Remarkably, this random connectivity model also exhibits orientation selectivity in the F1 component of the response. It emerges from the imbalances in ON and OFF inputs onto the target neuron. Unlike the ordered receptive field neuron, however, the preferred orientation of the F1 response of the cell changes with the stimulus spatial frequency. At high spatial frequency the F1 responses of the model neuron are largest for stimuli oriented at 30 degrees while at low spatial frequency responses are largest at -10 degrees (Fig. 2.1D). This shift in orientation preference is a product of the random connectivity onto the neuron: the imbalances of ON and OFF thalamic inputs are different as spatial scale changes, causing shifts in orientation preference.

Orientation selectivity emerges in a model of rodent V1 with random wiring

To study whether orientation selectivity in mouse V1 could result from random connectivity we constructed a large-scale conductance-based spiking

network model of V1 (Fig. 2.2) in which cortical neurons receive feedforward excitation from randomly chosen thalamic relay cells as well as other cortical cells of similar retinotopic preferences (Fig. 2.2B; see Methods). Previously it has been shown that orientation selectivity can emerge on the basis of random inputs alone (von der Malsburg, 1973; Soodak, 1987; Ringach, 2004). Orientation selectivity arises in these models because of asymmetries in the spatial preferences of the sparse inputs that converge onto a cortical neuron. As the number of convergent inputs increases, however, the selectivity declines because the tuned temporally modulated component of the LGN input decreases relative to the time averaged untuned component. To surmount this dependence of orientation selectivity on the number of inputs we employ a network model in which excitatory and inhibitory inputs are strong but balanced (van Vreeswijk and Sompolinsky, 1996, 1998) such that the mean and variance of the net input is on the order of the distance to threshold (Fig. 2.2 E).

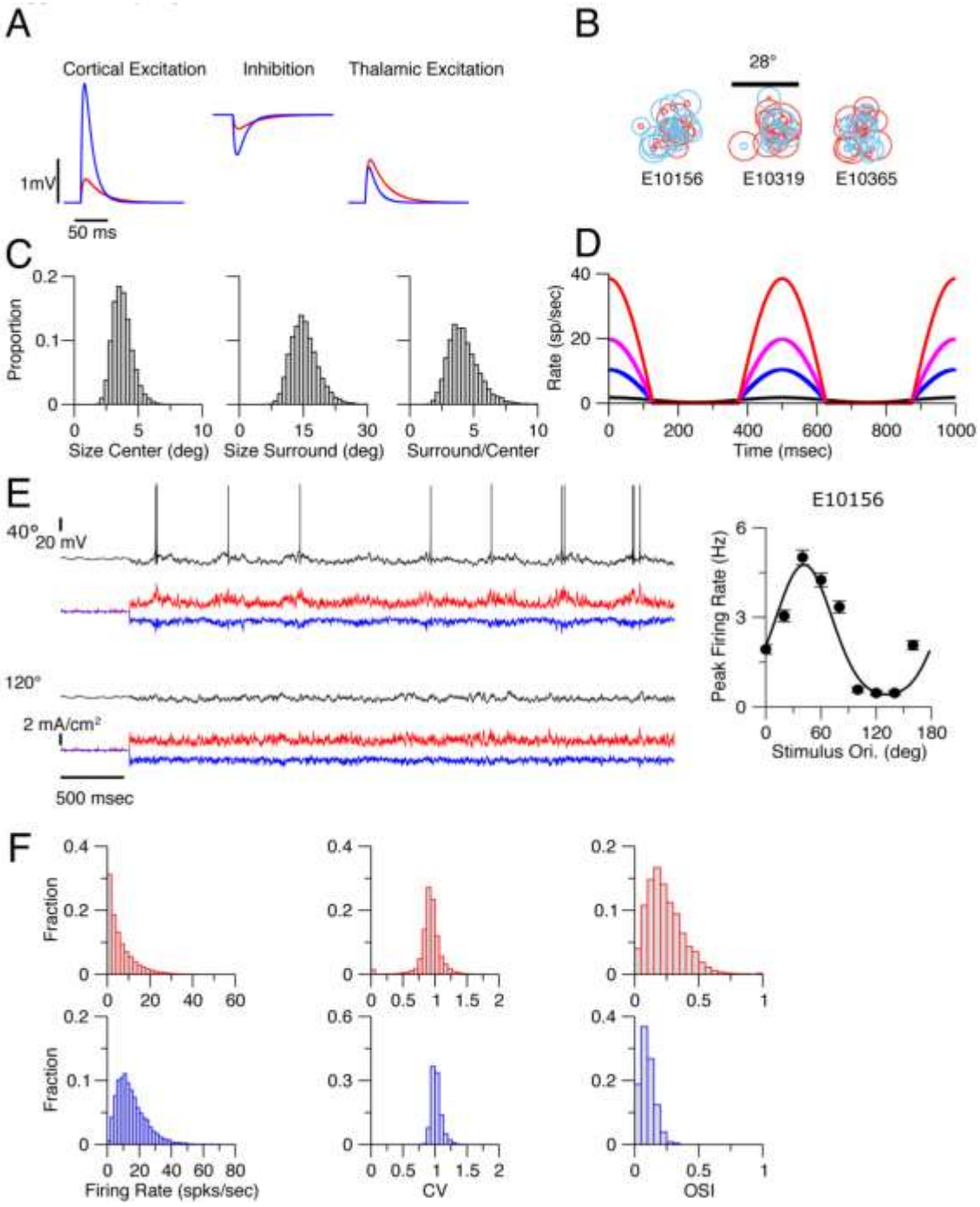

Figure 2.2: Large scale spiking model of V1 in balanced regime.

Parameters are as in Tables S1 and S2. A. PSPs for the cortical excitation (left), the cortical inhibition (middle) and the thalamic excitation (right). Red: PSPs for excitatory postsynaptic neuron. Blue: PSPs for inhibitory postsynaptic neuron. B. Receptive fields of thalamic neurons presynaptic to three representative cortical neurons. Thalamic neurons have circular receptive fields modeled as a difference of Gaussian describing OFF and ON subfields (see Methods). Red: ON subfield. Blue: OFF subfield. The radii of the plotted circles are the standard deviation (SD) of the corresponding Gaussians. C. Histograms of the radii of center (left) and surround subfields (middle). Right: histogram for the ratio of the surround and the center subfields radii. D Responses of LGN neurons are strongly rectified unless the contrast is very low. Firing rate of one typical LGN neuron as a function of time when the spatial frequency of the stimulus is 0.04 cpd, for 4 values of the contrast: ε=100% (red), 50% (magenta), 25% (blue) and 2% (black). The RF is circular with σcx=σcy=1 deg , σsx=σsy=6.3 deg and β=2.1 E. Voltage traces for one excitatory neuron. Stimulus begins at t=500msec. The drifting grating (SF = 0.03 cyc/deg) is presented at two orientations: 40° (upper trace) and 120° (lower trace). The panels below the voltage traces depict the excitation/inhibition balance. The excitatory (red), inhibitory (blue) currents to the neuron are plotted (note that in simulations all these currents and the voltage are always simultaneously known). Right panel: The tuning curve of the neuron. Average firing rate averaged over 80 sec. Parameters are as in Tables 1 and 2. F. Histograms of the peak firing rate (left), the coefficient of variation (CV) of the interspike distribution (middle).The stimulus is at 0° (SF=0.03 cyc/deg). Histograms are essentially the same for all stimulus orientations. The heterogeneity in firing rates and high temporal variability (CV around 1) of the neurons' discharges are hallmarks of the balanced state. Right panel: The OSI of the peak response (SF=0.03 cyc/deg). Red: Excitatory neurons. Blue: Inhibitory neurons. Inhibitory neurons are much less selective than excitatory neurons in agreement with experimental results (Kuhlman et al., 2011). (Fig. 2.2 continued).

Networks with random connectivity operating in a balanced regime have previously been shown to maintain preferences present in the input (Hansel and van Vreeswijk, 2012). We hypothesized that orientation selectivity would emerge in our model if the spatial inhomogeneity in the aggregate thalamic input were maintained in the output by the balance of excitation and inhibition. In the balanced state the untuned time-averaged component of the input is largely suppressed by the intracortical feedback, leading to a net input in which the

tuned modulation is comparable to the untuned component. Indeed, orientation selectivity emerges in our model (Fig. 2.3A), varying between highly selective neurons (e.g. model neuron E10371) to weakly selective (e.g. model neuron E11763). This diversity of selectivity results in a distribution of orientation selectivity index (OSI) demonstrating that orientation selectivity emerges naturally in a random connectivity model (Figs. 2.3, 2.2F, 2.4, 2.5). The emergent cortical orientation preference is matched to the preferred orientation of aggregate thalamic input (Fig. 2.4 A, B), as observed in mouse visual cortex (Li et al., 2013). In this balanced model the emergent orientation selectivity should be insensitive to the number of inputs. To verify this, we varied this number from 25 to 100 and found that the degree of orientation selectivity was maintained (Fig. 2.3C, D, Fig. 2.5). The emergent selectivity is also robust to changes in network size and in synaptic strength (Fig. 2.5A,B).

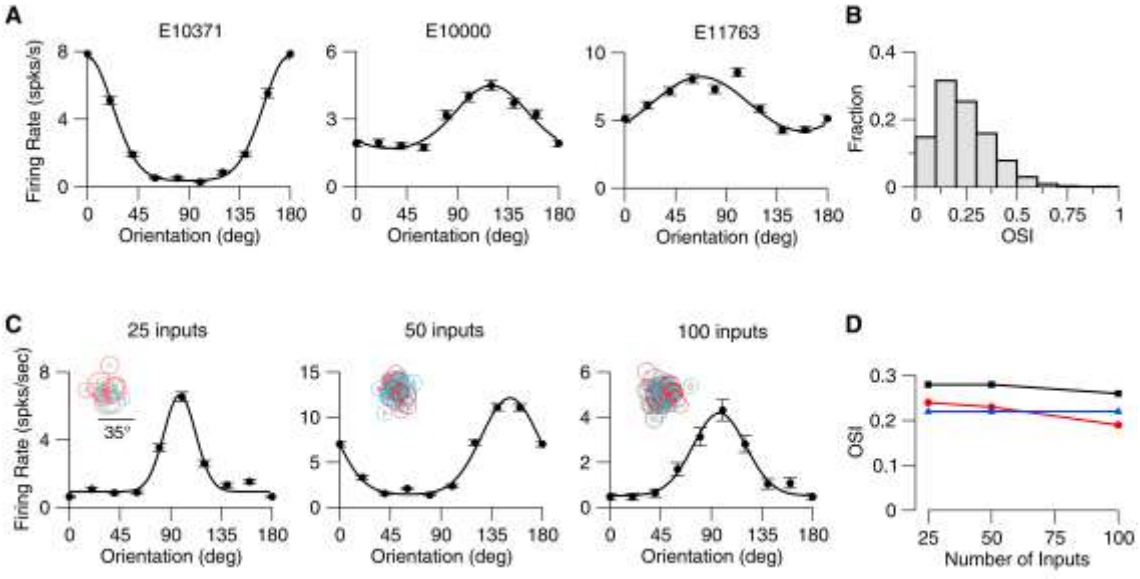

Figure 2.3: Orientation selectivity emerges in mouse V1 model.

A. Examples of tuning curves (peak firing rate) of three excitatory V1 neurons in the model. SF of the drifting grating is 0.03 cyc/deg. OSIs from left to right are: 0.62, 0.23, 0.15. B. Distribution of OSI (peak response) over all the neurons (neurons in the central part of the network; see Methods; n=5041). Mean OSI=0.24 (mean OSIs of the F0 and F1 components of the response are 0.29 and 0.19). C. Examples of tuning curves of excitatory neurons in networks with different average number of thalamic inputs per neuron. From left to right: OSI=0.47, 0.48, 0.49. D. Average OSIs vs. average number of thalamic inputs. Red: Peak spike response. Black: F1 component of the spike response. Blue: F1 component of the thalamic excitatory input. (Fig. 2.3. continued).

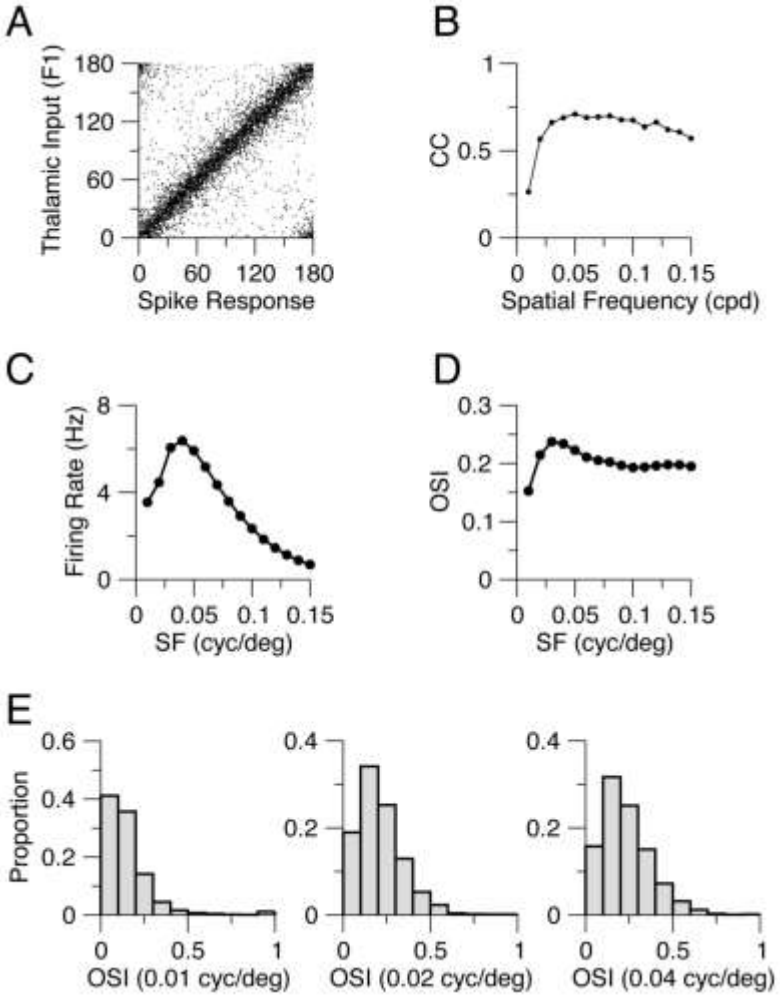

Figure 2.4: Dependence of the firing rate and selectivity on spatial frequency in the V1 network model.

A. Preferred orientation of the thalamic excitation vs. preferred orientation of the spike response of the cortical neurons for SF=0.03 cyc/deg (n=5041). B. The circular correlation (CC, see Methods) of the thalamic input and spike response preferred orientations vs. the spatial frequency. The dependence on spatial frequency is weak except for low spatial frequency. C. Population average of the peak firing rate at preferred orientation (E neurons) vs. grating spatial frequency (See Methods). D. Population average OSI of the peak spike response vs. spatial frequency. E. Histograms of the OSI for different spatial frequencies. (For 0.03 cyc/deg, see Fig. 2.3). The histograms are similar except for SF=0.01 cyc/deg. (Fig. 2.4. continued).

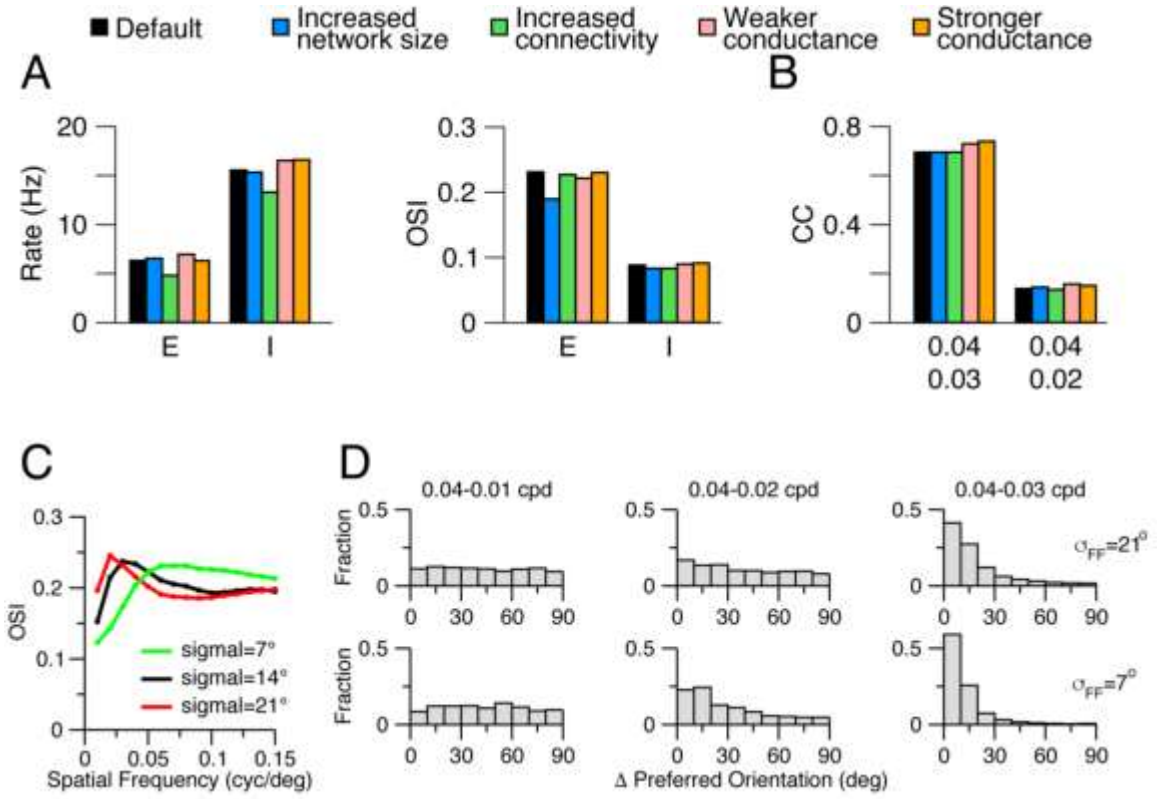

Figure 2.5: Robustness to changes in the model network size, connectivity parameters and thalamo-cortical dispersion.

A. Bar charts for the population averaged peak response (orientation of the stimulus: 0°; SF=0.04 cycle/deg) for excitatory (E) and inhibitory (I) neurons (left) and population averaged OSI (right). Black: Default set of parameters (Table 1,2). Blue: NE=78400, NI=19600, NL=40000; other parameters as in

Table 1, 2. Green: KEL=100; gEL was increased to keep in both populations the firing rate approximately the same.: gEL=0.009 mS msec/cm2; Pink: All conductances are multiplied by 0.75; Orange: All conductances are multiplied by 1.25. Other parameters as in Table 2.1, 2.2. B. Correlation coefficient (CC) for excitatory population between the preferred orientation of spike response for SF=0.04 cyc/deg and SF=0.03 cyc/deg (left) and SF=0.02 cyc/deg (right). For SF=0.01 cyc/deg: CC=0. Color code as in A. C. Population average OSI of the peak spike response of excitatory neurons vs. spatial frequency for σFF. = 14° (black), 21° (red) and 7° (green). Other parameters as in Table 1, 2. D. Histograms of the difference in orientation preference between 0.04 cyc/deg and 0.01 (left), 0.02 (middle) and 0.03 (right) cyc/deg. σFF=7° are plotted in the top row. The bottom row shows the histograms for σFF =21°. Compare with the corresponding histograms for σFF=14° (Fig. 4). Only neurons with OSI larger than 0.2 for each pair of spatial frequencies are included. For σFF=7°: CCs are 0.72 (0.04-0.03 cyc/deg), 0.18 (0.04-0.02 cyc/deg) and 0 (0.04-0.02 cyc/deg). For σFF=21°: CC=0.48, (0.04-0.03 cyc/deg), 0.03, (0.04-0.02 cyc/deg), 0 (0.04-0.01 cyc/deg). (Fig. 2.5. continued).

Orientation selectivity emerges in our random connectivity model because of the spatial inhomogeneity in inputs to cortical neurons. In particular, the convergence of ON and OFF thalamic inputs onto model neurons are spatially offset from one another. The orientation of this offset may be related to the emergent orientation preference of neurons (Liu et al., 2010; Lien and Scanziani, 2013). To assess this relationship, we estimated the ON and OFF subfields of the thalamic inputs by presenting spots at different locations to the model network as in Lien and Scanziani (2013) (see Methods). The estimated ON and OFF subfields for 4 example neurons reveal different offsets. When ON and OFF subfields have large horizontal displacements (E14493, E14847) preference for the vertical orientation of the drifting grating at 0.03 cyc/deg tends to emerge whereas when ON and OFF subfields are vertically displaced preference for horizontal orientations tends to emerge (Fig. 2.6A, E14664). The offsets in ON and OFF subfields that emerge from the random connectivity model (Fig. 2.6B)

are similar to those observed experimentally (Lien and Scanziani, 2013). When the ON/OFF offset is large there is a strong correspondence between the axis of the offset and the preferred orientation of the thalamic input (Fig. 2.6). The ON and OFF displacement, however, is not the only factor that contributes to this orientation preference. The randomness in the feedforward connectivity generates ON and OFF subfields of the thalamic excitation that deviate from circularity. The shape of the subfields, and the interaction between the subfields, can create orientation preferences that deviate from that predicted from the offset of ON and OFF subfields (Fig. 2.6A, example 15022). In sum, the offset of ON and OFF subfields, their interaction, and their shape influence the emergent thalamic orientation selectivity. Because the thalamic input selectivity is directly related to the cortical output selectivity (Fig. 2.4A, B) these factors impact the emergent cortical orientation selectivity in the same way. The emergent orientation preference, however, is particularly sensitive to the spatial structure of the stimulus (Fig. 2.1).

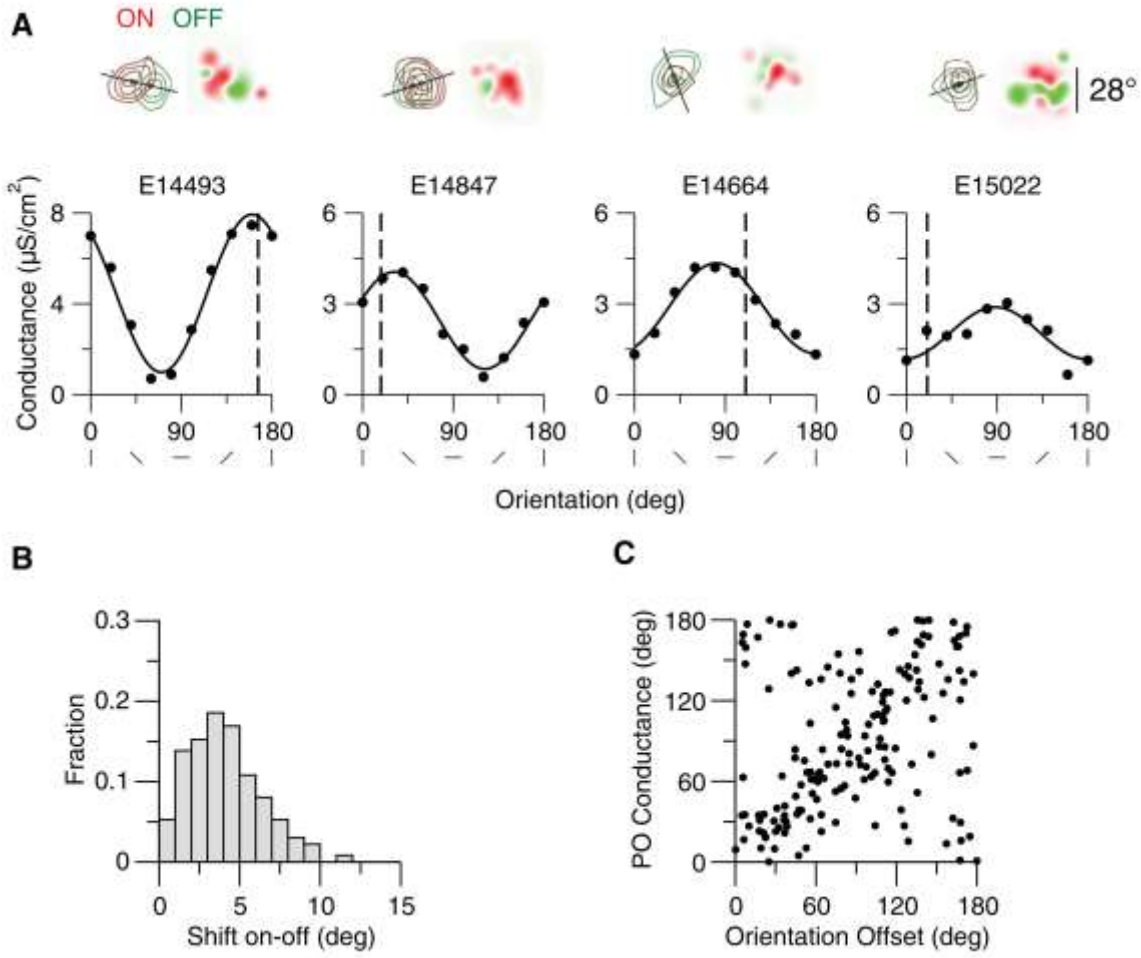

Figure 2.6: The contribution of the offset of ON and OFF subregions of the thalamic excitation to its orientation preference.

The ON and OFF subfields of the thalamic inputs were estimated by presenting spots at different locations to the model network as in Lien and Scanziani (2013) (see Methods). A. Top panels: ON (red) and OFF (green) subfields of the thalamic excitation for four example neurons. Dark spots: Center of mass of the subfields. The solid line indicates the axis of the offset of the two centers of mass. Receptive fields based on the summed ON and OFF thalamic inputs are shown on the right. Bottom panels: Tuning curves of the thalamic excitation for these neurons. The SF of the drifting grating is 0.03 cyc/deg. Vertical dashed

line indicates the orientation of the offset axis (0° corresponds to a horizontal axis). Offset amplitude and orientation and preference of the thalamic excitation is: E14493: 11.4°; 166.1°, 160.3°. E14847: 4.7°, 18.2°, 31.1°. E14664: 3.9°, 111.4°, 80.7°. E15022: 2.8°, 20.6°, 88.0°. B. Offset distribution across neurons (n=361; neurons are at the center of the network, see Methods). Mean offset: 4.1°. D. Orientation preference of the thalamic input conductance (drifting grating with 0.03 cyc/deg) vs. orientation of the offset axis for all neurons with an offset larger than 4° (n=170). The circular correlation is: 0.24. (Fig. 2.6. continued).

Dependence of preferred orientation on spatial frequency in the model

We then characterized how much the properties of the neuronal responses vary with spatial frequency in the model. First, we investigated how the population average peak response and OSI were affected when changing spatial frequency (SF). We found that, although the mean population response was modulated by SF (maximal response for SF, 0.035 cyc/deg) the overall selectivity of the population was less sensitive to SF (Fig. 2.4D, E). This mild effect across the population contrasts with the effect of spatial frequency changes on the preferred orientation of individual neurons. As we varied the SF, the preferred orientation of neurons often changed (top and bottom left panels in Fig. 2.7A; Fig. 2.7B, C, pink). We quantified this change by computing the circular correlation (CC, see Methods) of the preferred orientation at different spatial frequencies across neurons. This correlation was strong for nearby spatial frequencies, whereas for spatial frequencies far apart it was weaker (Fig. 2.7B and C). It declined from 0.71 for 0.04-0.03 cyc/deg to 0.00 for 0.04-0.01 cyc/deg (Fig. 2.8, $\Delta CC=0.71$). We found that this effect was robust to changes in network size, the number of connections per neuron, and the synaptic conductance strengths (Fig. 2.5). We also found that it was qualitatively robust to changes in

spatial dispersion of the thalamic feedforward connections but that the decorrelation was weaker for small dispersions (Fig. 2.5.C and D).

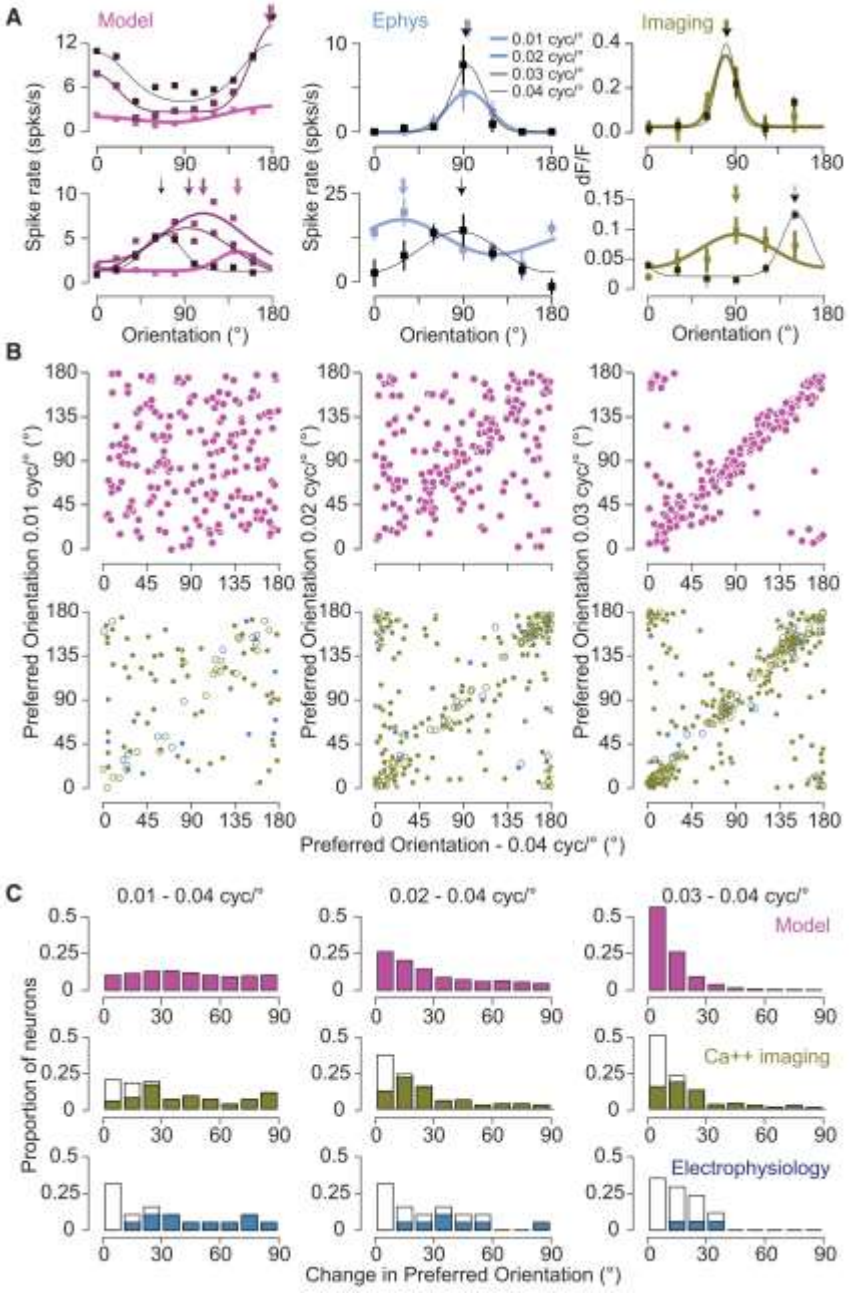

Figure 2.7: SF and orientation selectivity in the model and mouse V1.

A. Example orientation tuning curves based on spike rate are plotted for neurons in the spiking network model (left), electrophysiology (middle) and based on fluorescence changes from calcium imaging experiments (right). Orientation tuning curves are plotted for different spatial frequencies, from 0.01 to 0.04 cyc/deg, indicated by color. If the error bars are not visible, they are smaller than the symbol size. B. Top row: The relationship between preferred orientations in the model. Left: 0.04 cyc/deg and 0.01 cyc/deg. Middle: 0.04 cyc/deg and 0.02 cyc/deg. Right: 0.04 cyc/deg and 0.03 cyc/deg. Bottom row: The same for the calcium and electrophysiological records (green and blue symbols, respectively). The bootstrapped vector average is used as the estimate of the preferred orientation. For calcium and spiking data, statistically significant shifts in orientation preference are indicated by filled circles. Number of cells in the imaging data for comparison of 0.01 and 0.04 cyc/deg is 90, for comparison of 0.02 and 0.04 cyc/deg is 228 and for comparison of 0.03 and 0.04 cyc/deg is 288. Number of cells in the electrophysiological data for comparison of 0.01 and 0.04 cyc/deg is 32, for comparison of 0.02 and 0.04 cyc/deg is 28 and for comparison of 0.03 and 0.04 cyc/deg is 25. C. Histograms of the difference in orientation preference between 0.04 cyc/deg and 0.01 (left), 0.02 (middle) and 0.03 (right) cyc/deg. Filled bars for electrophysiology and calcium imaging data indicate statistically significant changes in orientation preference. (Fig. 2.7. continued).

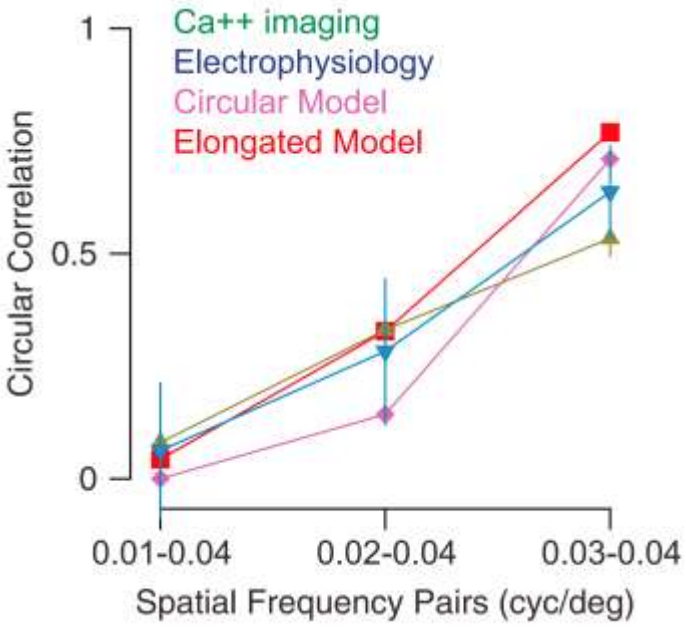

Figure 2.8: Comparison between model and experimental results.

Graph indicates the observed circular correlation between preferred orientations of single neurons at two spatial frequencies. The pairs of spatial frequencies being compared are indicated on the X axis. Green: Calcium imaging. Blue: Electrophysiology. Purple: Model with circular thalamic receptive fields (same as in Fig. 2.7), Red: Model with elongated thalamic receptive fields (see text and Fig. 2.12). Error bars are bootstrapped confidence intervals on the circular correlation. (Fig. 2.8. continued).

Dependence of preferred orientation on spatial frequency in mouse V1

These theoretical results prompted us to determine whether spatial frequency has a similar effect on orientation preference in mouse V1. Varying spatial frequency yielded shifts in orientation preference for many, but not all, neurons when measured using intracellular, whole-cell, recordings (Fig. 2.7A, middle: top and bottom panels; Fig. 2.7C, blue panels). Changes in orientation preference were observed both at the level of spike rate and membrane potential (38 total cells) (Fig. 2.9). To gain access to this effect in large populations of V1 neurons, we also examined it by measuring calcium responses using 2 photon microscopy (606 total cells) (Fig. 2.7A, left: top and bottom panels; Fig. 2.7B, C, green panels; Fig. 2.10). As with our electrophysiological data we found a diversity of changes with spatial frequency: preference shifted dramatically for some neurons and not for others.

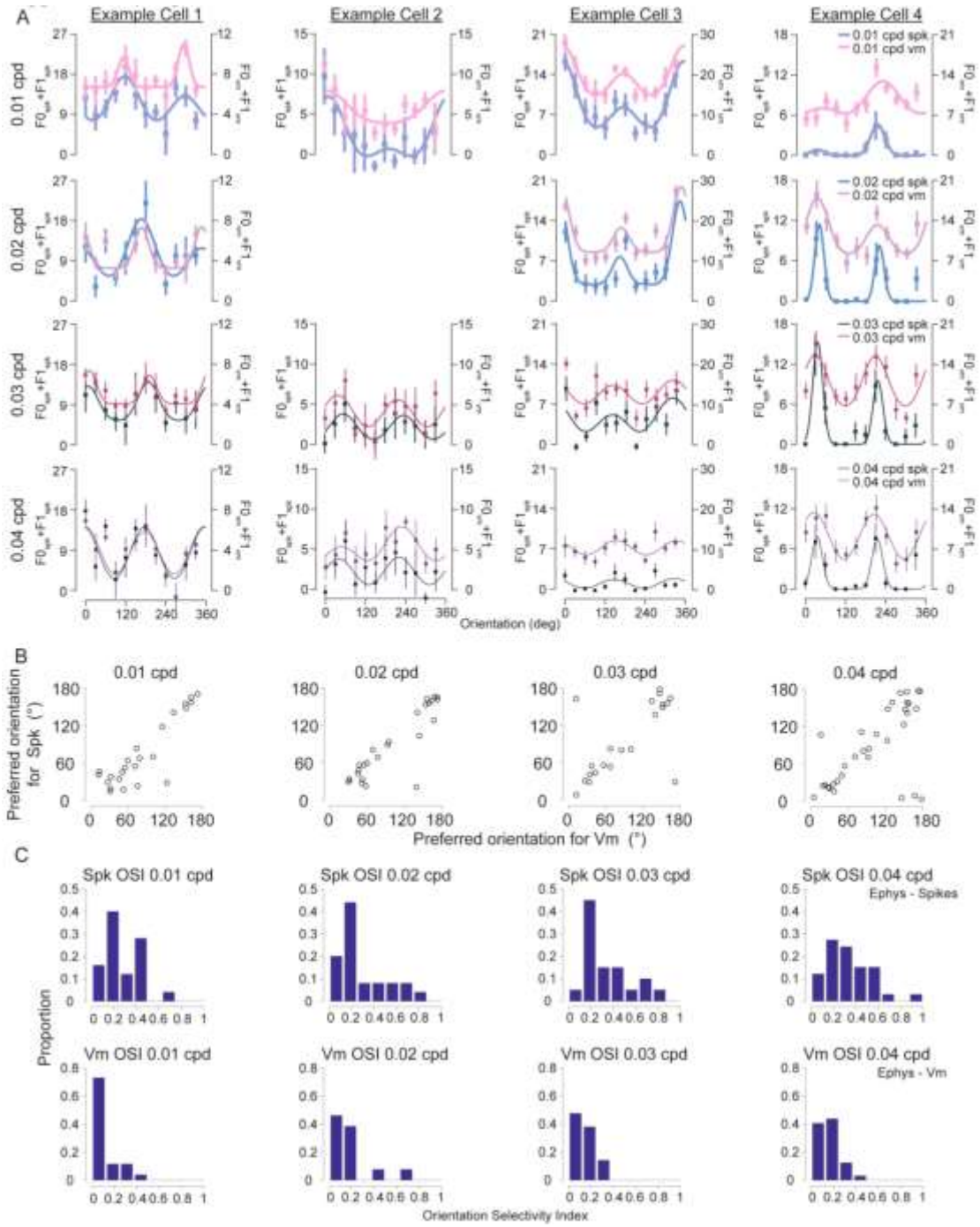

Figure 2.9: Vm and spike orientation preferences show similar dependency on spatial frequency.

A. Each column represents a neuron. Each row is tuning curves for a different SF. Both the Vm and spikes based tuning curves show similar preference. B. The preferred orientation based on spikes vs. the preferred orientation based on Vm for all neurons. C. The orientation selectivity index (Methods) for spike rate (top row) and membrane potential (bottom row). (Fig. 2.9. continued).

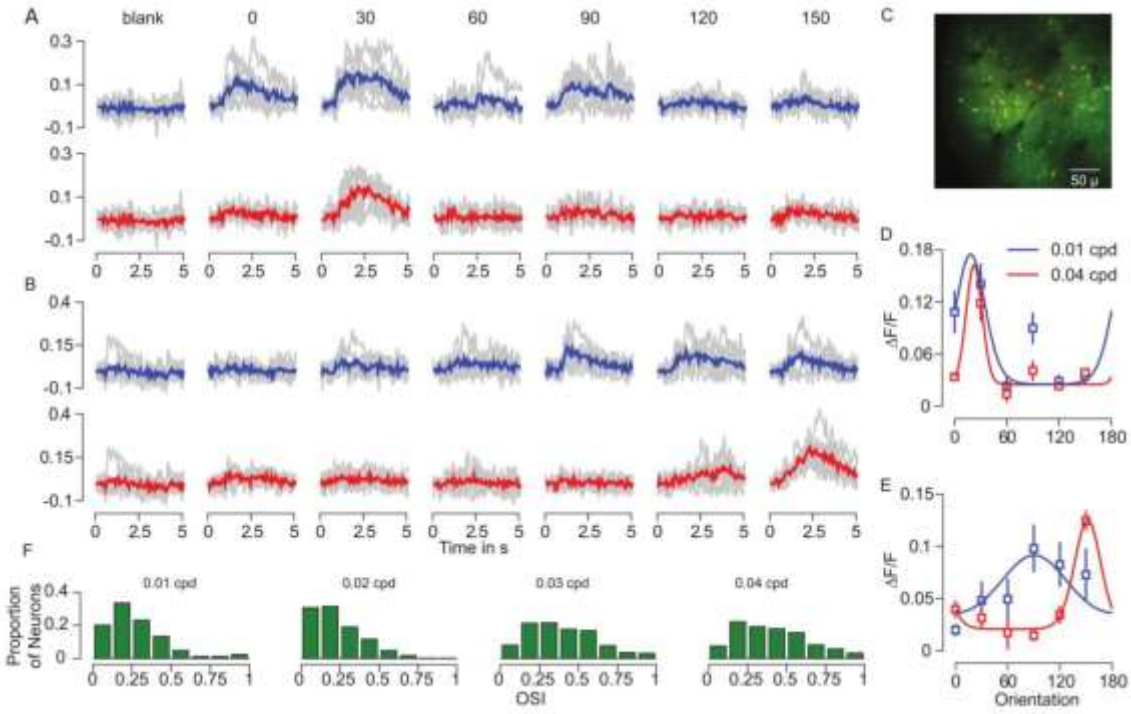

Figure 2.10: Example calcium orientation selectivity in mouse V1.

A, B: The calcium responses for three example neurons for different orientation conditions and two spatial frequencies (0.01 cpd, blue and 0.04 cpd, red). C: Example imaging plane. D, E: Orientation tuning curves for different SFs for the neurons represented in a and b. F: OSI distribution across all SFs used.

These differences in preferred orientation observed from our Ca++ responses could be due to noise in our measurements. To be included in our population analysis, cells were required to have a minimum peak response of 8% at both frequencies. Using different thresholds to include cells yields similar declines in correlation when comparing orientation preference at 0.04 cyc/deg to

0.03 and 0.01 cyc/deg (8%: ΔCC=0.46 with 90 cells for 0.01 and 0.04 cyc/deg and 288 cells for 0.03 and 0.04 cyc/deg; 10%: ΔCC=0.4 with 43 cells for 0.01 and 0.04 cyc/deg and 182 cells for 0.03 and 0.04 cyc/deg; 12%: ΔCC=0.52 with 22 cells for 0.01 and 0.04 cyc/deg and 139 cells for 0.03 and 0.04 cyc/deg). To address whether the observed effect was influenced by differences in response amplitude for different spatial frequencies, we also restricted our analysis to neurons with differences in peak response amplitudes less than 10% (Fig. 2.11). This also did not alter the decline in circular correlation (ΔCC = 0.49, n = 86 for 0.01 and 0.04 cyc/deg and n = 259 for 0.03 and 0.04 cyc/deg). Furthermore, we examined whether the reduction in CC was related to the OSI of neurons by restricting our analysis to only those cells within the top 25% of our distribution. This restriction yields a similar ΔCC of 0.45 (n = 23, 0.01-0.04 comparison, n = 72 for 0.03-0.04 comparison). In sum, orientation preference changed with spatial frequency in electrophysiology records as well as calcium imaging measurements.

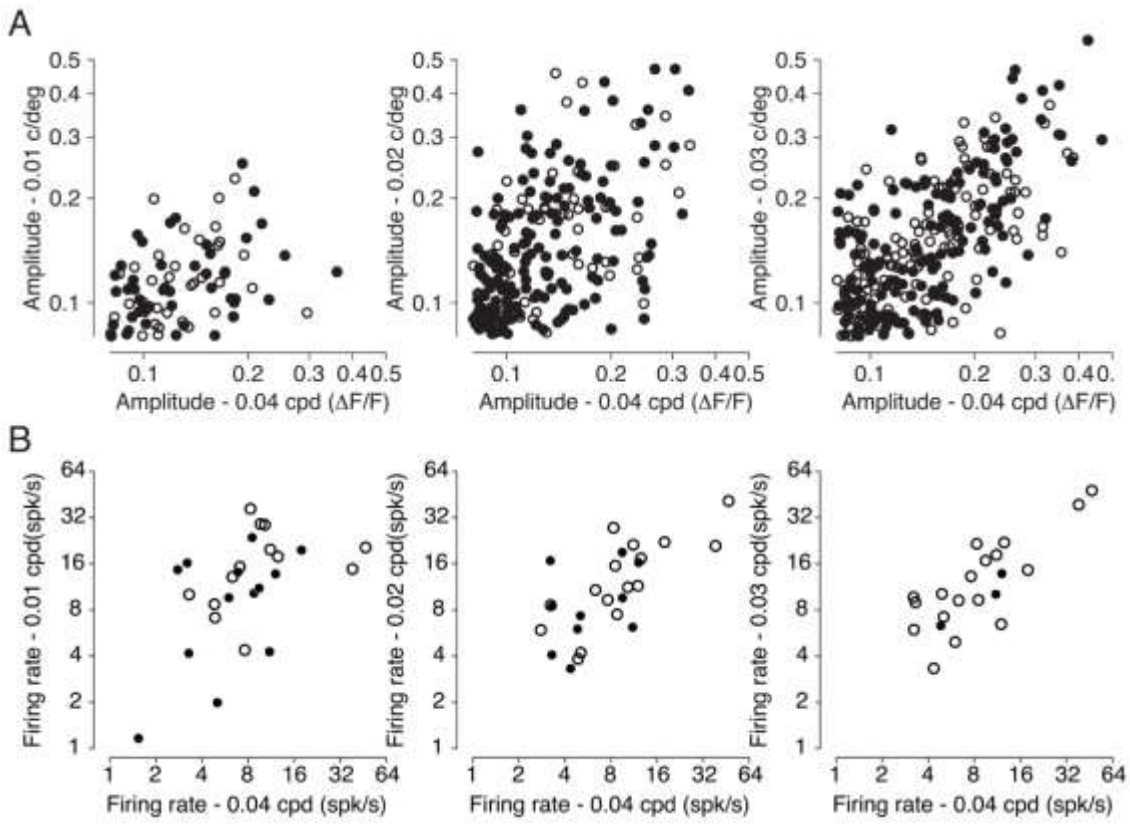

Figure 2.11: Response amplitudes across spatial frequencies in mouse V1.

A: The amplitude of calcium responses used to extract orientation preference are plotted for 0.01, 0.02 and 0.03 relative to the amplitudes at 0.04 cyc/deg. Closed symbols have significant changes in orientation preference whereas open symbols did not exhibit significant changes in orientation preference. B: As in A, but for electrophysiology. Responses had the background response removed by subtraction.

We have found that both the model and actual mouse V1 neurons exhibit changes in orientation preference with spatial frequency in a similar fashion (Fig. 2.8). That is, for small frequency shifts the model and actual neurons have

similar orientation preferences, as indicated by a high CC, whereas large changes in SF cause substantial decreases in CC. One notable discrepancy between the model and actual data is that nearby spatial frequencies have higher correlations for the model than for the data. A factor that contributes to this discrepancy is the amount of data collected in the model records relative to the physiological records (between 10 and 24 s for each orientation and SF). When we limit the records from which the model data are based to 20 seconds, instead of 80 seconds, ΔCC declines from 0.71 to 0.58. An additional factor we considered is the nature of the thalamocortical input. Orientation selectivity does exist in mouse thalamic neurons (Piscopo et al., 2013; Scholl et al., 2013b; Zhao et al., 2013), so we also explored the impact of elongated thalamic receptive fields on the properties of the cortical model (Fig. 2.12). This impact was modest, slightly altering the dependence of orientation preference on spatial frequency (Fig. 2.8, elongated thalamic receptive field model, ΔCC=0.73, Fig. 2.12 F,G), while increasing the overall orientation selectivity of V1 excitatory neurons (mean OSI = 0.32 vs 0.23 for circular thalamic receptive field) , Fig. 2.12B).

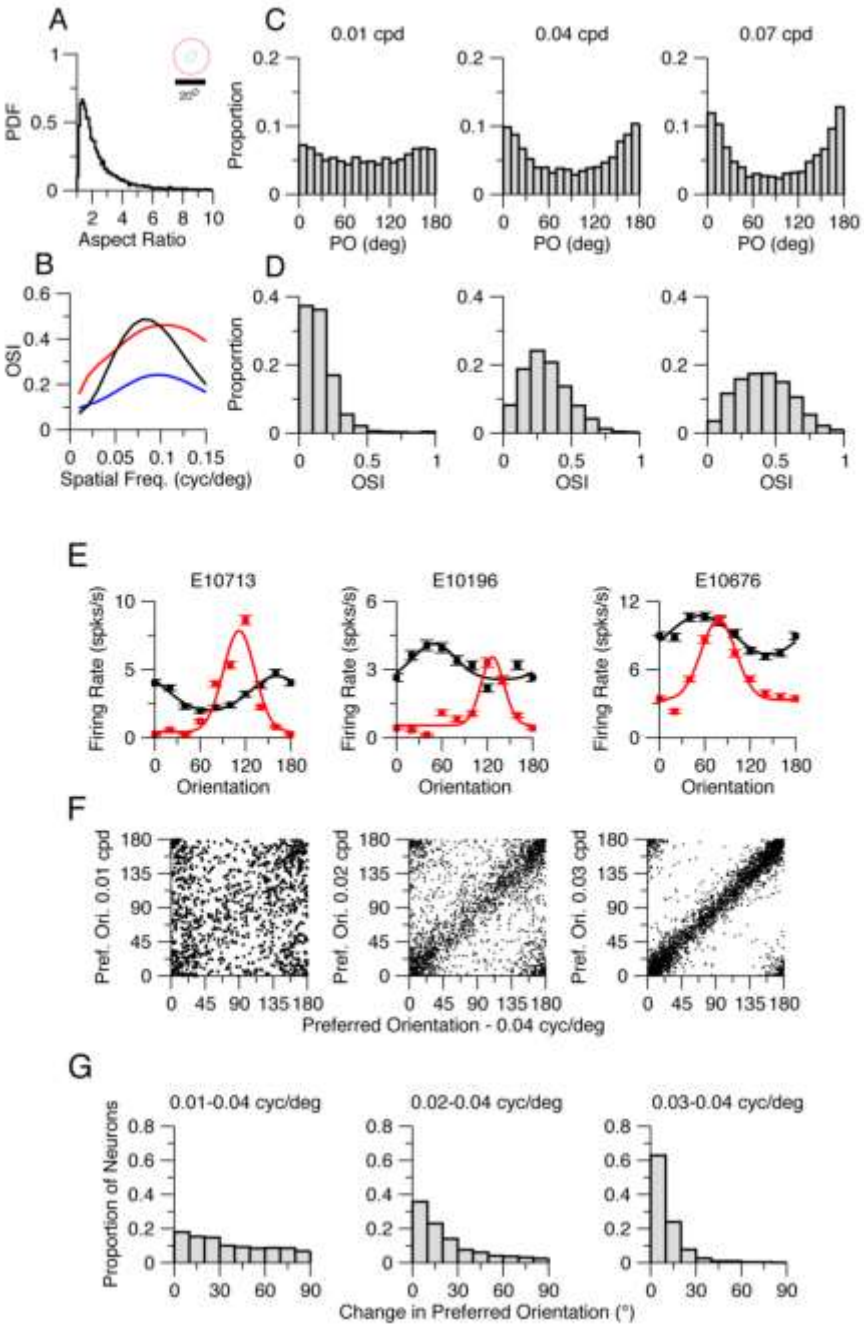

Figure 2.12: The V1 network model with elongated thalamic receptive fields.

Parameters are as in Table 2.3. A. The central subfields of the receptive fields of LGN cells are elongated. Surround subfields are circular. Distribution of the aspect ratio for the center subfield is plotted. Inset: Example of a thalamic neuron receptive field. B. Population average OSI for the spike peak response vs. spatial frequency. Red: E cells. Blue: I cells. Black: LGN cells. C. Histograms of the preferred orientations of the excitatory neurons for grating with 0.01 (left), 0.04 (middle) and 0.07 (right) cyc/deg. Preferred orientations are bias toward 0° because the distribution of the axis orientation of the center subfield of LGN cells is biased toward this orientation. D. Histograms of OSI for E neurons. Left to right: 0.01, 0.04, 0.07 cyc/deg. E. Tuning curves of three example E cortical neurons. Black: 0.01 cyc/deg; Red: 0.04 cyc/deg. F, G. Population data demonstrating the change in preferred orientation with spatial frequency. CC=0.77 (0.04-0.03 cyc/deg)., 0.33 (0.04-0.02 cyc/deg,) 0.04 (0.04 -0.01 cyc/deg. (Fig. 2.12. continued).

Two-dimensional SF filters of neurons in mouse V1 are non-separable

The observed dependence of orientation preference on spatial frequency indicates that in mouse V1, neuron receptive fields are not simple orientation detectors. Instead they may be measuring components of the visual scene that are better characterized by a conjunction of two-dimensional SF filters. We therefore measured responses of V1 neurons while varying vertical and horizontal spatial frequency components (Ringach et al., 2016) (24 cells, Hartley gratings, see Methods; Fig. 2.13A). Neurons whose orientation selectivity is invariant to spatial frequency, would exhibit preference profiles for which angle (orientation) does not change with the distance from the origin (SF). As before different neurons revealed a diversity of behaviors (similar to kernels shown in Ringach et al., 2016), from invariance (Fig. 2.13A, left) to systematic change in selectivity with spatial frequency (Fig. 2.13A, middle). We also recorded from a small number of inhibitory neurons (identified based on spike rate and action

potential width) with broad selectivity for orientation and SF (Niell and Stryker, 2008) Fig. 2.13A, right). Measures of orientation preference based on the Hartley stimulus qualitatively agree with those made by measuring orientation tuning curves at different spatial frequencies (compare top and bottom panels in Fig. 2.13A). This indicates that many V1 neurons are better characterized as containing receptive fields that are a conjunction of horizontal and vertical spatial frequency filters instead of invariant selectivity for orientation. We performed a comparable analysis in our V1 network model (see Methods) and found a similar behavior (Fig. 2.13B; Fig. 2.14).

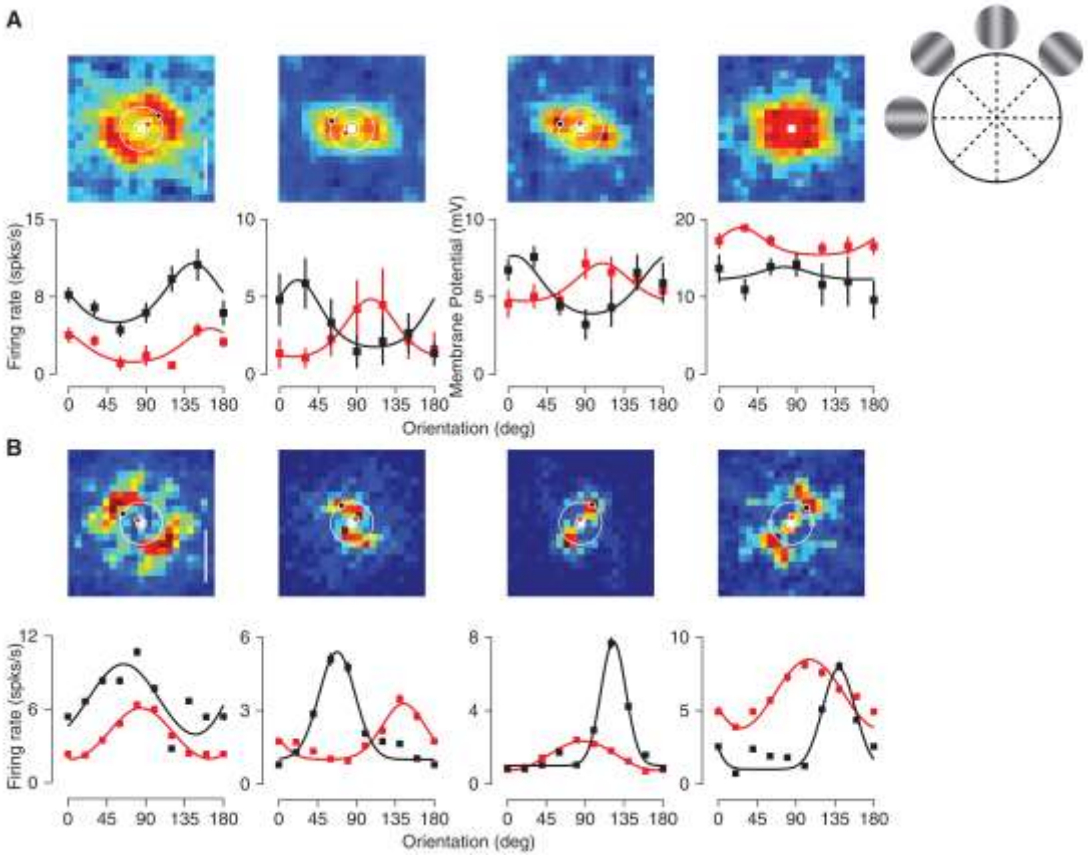

Figure 2.13: Neuron receptive fields in the frequency domain are intricate.

A. Mean membrane potential responses to Hartley stimuli (see Methods) are plotted for combinations of horizontal and vertical spatial frequencies (top row). Circles indicate stimulus combinations corresponding to oriented gratings at fixed spatial frequencies. Each panel corresponds to a different example cell. Orientation tuning curves for drifting gratings at 0.014 cyc/deg and 0.044 cyc/deg are shown for these four neurons (bottom row). B. Example frequency receptive fields for four neurons in the model. Orientation tuning curves at 0.01 cyc/deg and 0.04 cyc/deg are shown for these neurons (bottom row) based on responses to drifting gratings. (Fig. 2.13. continued).

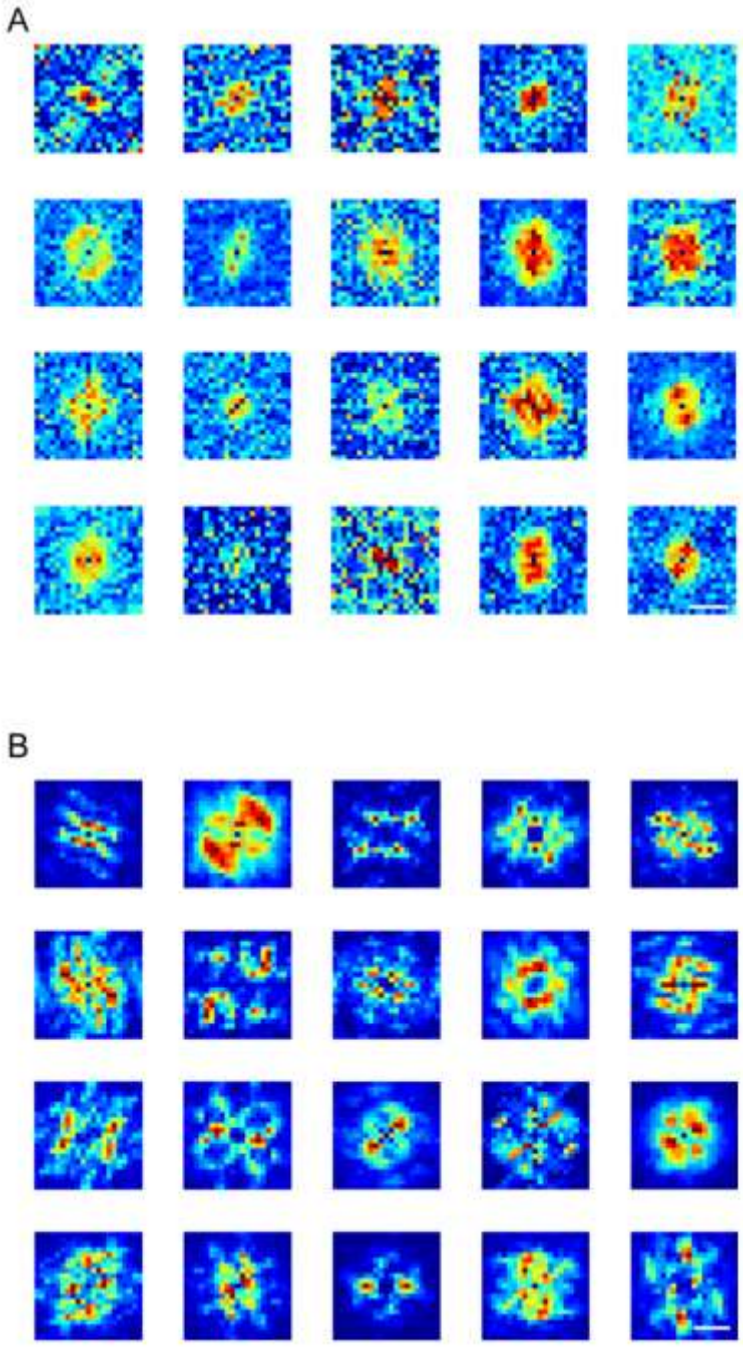

Figure 2.14: Examples of Hartley RFs based on electrophysiology and the model.

A. 20 example neuron membrane potential responses to the Hartley stimulus. B. 20 example responses of model neurons to the Hartley stimulus.

DISCUSSION

We have presented a network model for rodent V1 that demonstrates that orientation selectivity can emerge from random connectivity even if LGN cells are not selective. It makes the specific prediction that this selectivity should be sensitive to spatial form for some V1 neurons. Testing that prediction in mouse visual cortex, we found a similar effect. Using a model that receives thalamic inputs which exhibited some orientation selectivity increased the degree of cortical orientation selectivity yielding distributions of OSI closer to experimental estimates. This model also exhibited a similar dependence of orientation preference on spatial frequency.

In our models there is a strong overlap of the ON and OFF subregions of the thalamic inputs as seen in experiments (Liu et al., 2010; Li et al., 2013; Lien and Scanziani, 2013). When the offset between the centers of the ON and OFF subfields is large, the orientation of this offset can be predictive of the orientation preference of the neuronal response. Nevertheless, even when this offset is large, the orientation preference can change substantially with SF. In our model, the orientation of the offset and the orientation preference of the neuronal response are strongly correlated for intermediate SF (Fig. 2.15).

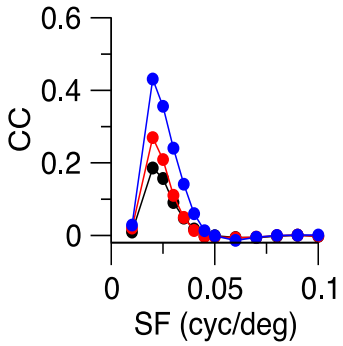

Figure 2.15: Correlation coefficient between the orientation of the ON-OFF offset axis and the orientation preference of the thalamic excitation vs. SF in the model.

Parameters of the model as in the default set. Black: All cells. Red: Offset > 2°. Blue: Offset > 4°.

Quantitatively, the decorrelation of preferred orientation with spatial frequency is somewhat weaker in experiments when compared to our models. One source of this discrepancy is related to the amount of data collected for the model and the experiments. When records for the model are limited to 20 seconds, the model ΔCC was 0.59, close to the experimental value of ΔCC = 0.46. The change in ΔCC is due to the decline in CC between 0.03 to 0.04 cyc/deg from 0.71 to 0.59. Another possible source for this difference is that we did not incorporate any feature specific component in the connectivity even though this has been shown to be present in mouse V1 after the critical period (Ko et al., 2011; Ko et al., 2013; Lee et al., 2016b).

We have demonstrated that V1 neurons' receptive fields are surprisingly intricate (Figs. 2.13, 2.14). This complexity stands in contrast to the V1 receptive fields in cats (Webster and De Valois, 1985; Jones et al., 1987; Hammond and

Pomfrett, 1990) and primates (De Valois et al., 1982), where orientation preference is represented in a separable manner from spatial form. A similar dependence in the mouse V1 was reported in a study based on calcium imaging (Ayzenshtat et al., 2016). There, it was demonstrated that a reduction in SF by one octave causes a mean shift in preferred orientation by 22.1°, comparable to our own estimates of the change in orientation when shifting from 0.04 to 0.02 cyc/deg (model: mean ΔPO = 29.8°, ephys: ΔPO = 30.2°, ca++: ΔPO =22.2°). They proposed that the dependence could arise from separable selectivity in frequency domain. We demonstrate here that while some V1 neurons do have separable frequency domain receptive fields, V1 receptive fields exhibit diverse dependencies that yield SF invariant orientation preferences (Fig. 2.13, first column) or SF-dependent orientation preferences (Fig. 2.13, second column).

Such receptive field complexity likely has an impact on connectivity patterns within V1. In primates and carnivores where preferred orientations are similar for different spatial frequencies, neurons with similar orientation preferences are much more likely to be connected (Bosking et al., 1997; Wilson et al., 2016). In mice, neurons with similar orientation preference have been reported to be somewhat more likely to be connected (Ko et al., 2011; Ko et al., 2013). However, in these experiments, difference in preferred orientation was measured at only one spatial frequency (0.045 cyc/deg). As we have shown, this difference varies with spatial frequency and the connectivity is likely to depend on the similarity in response at all spatial frequencies. Indeed, correlation in the response to natural stimuli was found to be a stronger factor than orientation

preference at one spatial frequency in determining connection probability (Ko et al., 2013; Cossell et al., 2015).

The intricate receptive field profiles described here are akin to those observed in primary auditory cortex. Auditory cortex neurons are sensitive to the combination of many auditory cues (Wang et al., 2005), which may comprise a synthesis sufficient to detect auditory objects (Bar-Yosef and Nelken, 2007). The frequency domain receptive field profiles observed in mouse V1 neurons may therefore reflect a similar progression toward a representation for objects using a random connectivity scheme that occurs as information flows through the visual pathway.

To conclude, our investigation demonstrates that random connectivity can be the dominant component accounting for emergent properties such as orientation selectivity. An important advantage of random wiring schemes is that they occur naturally, following the broader patterns of retinotopy that are formed by biochemical gradients. This natural emergence may thus reflect a wiring strategy that allows for selectivity without the cost associated with constructing specific afferent wiring connections.

METHODS

Procedures for two-photon imaging and physiology were based on those previously described (Scholl et al., 2013a; Scholl et al., 2015). Animals were anesthetized for the duration of the experiments and stimuli were presented on

calibrated CRT monitors. Analyses of physiological data were performed using routines in Matlab that have previously been employed (Scholl et al., 2013a). The computational model is composed of two networks. One represents LGN while the other represents layer 4 and layer 2/3. Neurons of the cortical network are described in terms of conductance-based models (Wang and Buzsaki, 1996; Hansel and van Vreeswijk, 2012).

Detailed experimental methods

Physiology.

Procedures for two-photon imaging and physiology were based on those previously described (Scholl et al., 2015; Scholl et al., 2016). Experiments were conducted using normal, adult male and female animals (n =33, P34 - P60). Mice were anesthetized with intraperitoneal injections of 1000 mg/kg urethane and 10 mg/kg chlorprothixene. Brain edema was prevented by intraperitoneal injection of up to 10 mg/kg dexamethasone. Animals were warmed with a thermostatically controlled heat lamp to maintain body temperature at 37° C. A tracheotomy was performed and the head was placed in a mouse adaptor (Stoelting). A craniotomy and duratomy were performed over visual cortex. Eyes were kept moist with a thin layer of silicone oil. Primary visual cortex was located and mapped by multi-unit extracellular recordings with tungsten electrodes (1 mΩ, Micro Probes). The V1/V2 boundary was identified by the characteristic gradient in receptive locations (Drager, 1975; Metin et al., 1988). Eye drift under urethane anesthesia is typically small and results in a change in eye position of less than 2 degrees per hour (Sarnaik et al., 2014).

Dye Loading and In vivo Two-Photon Microscopy

Bulk loading of a calcium sensitive dye under continuous visual guidance followed previous protocols in V1 (Stosiek et al., 2003; Kerr et al., 2005; Ohki et al., 2005; Mrsic-Flogel et al., 2007; Golshani and Portera-Cailliau, 2008). Dye solution contained 0.8 mM Oregon Green 488 BAPTA-1 AM (OGB-1 AM, Invitrogen) dissolved in DMSO (Sigma-Aldrich) with 20% pluronic acid (Sigma-Aldrich) and mixed in a salt solution (150 mM NaCl, 2.5 mM KCl, 10 mM HEPES, pH 7.4, all Sigma-Aldrich). 40-80 µM Alexa Fluor 594 (Invitrogen) was also included for visualization during and immediately after loading. Patch pipettes (tip diameter 2-5 µm, King Precision Glass) containing this solution were inserted into the cortex to a depth of 250-400 µm below the surface with 1.5% agarose (in saline) placed on top the brain. The solution was carefully pressure injected (100-350 mbar) over 10-15 minutes to cause the least amount of tissue damage. OGB-1-AM is only weakly fluorescent before being internalized, so the amount of dye injected was inferred through the red dye. To ensure full loading we waited 1 hour before adding a glass coverslip for imaging. Metal springs were fastened on the attached head plate to place pressure on the glass coverslip and reduce brain pulsations. Fluctuations in calcium fluorescence were collected with a custom-built two-photon resonant mirror scanning microscope (Scholl et al., 2015) and a mode-locked (925 nm) Chameleon Ultra Ti: Sapphire laser (Coherent). Excitation light was focused by a 16X or 40x water objective (0.8 numerical aperture, Nikon). Images were obtained with custom software (Labview, National Instruments). A square region of cortex 300 µm wide was imaged at 256x455 pixels. In all experiments, multiple focal planes, separated by

20-25 µm, were used to collect data, starting around 150 µm below the cortical surface. Before each experiment neuron drift was measured over a 2-3 min period. If drift occurred, then the glass coverslip and agarose were readjusted to stabilize the brain during stimulus protocol (7-20 minutes each focal plane).

Stimuli.

Visual stimuli were generated by a Macintosh computer (Apple) using the Psychophysics Toolbox (Brainard, 1997; Pelli, 1997) for Matlab (Mathworks). Gratings were presented using a Sony video monitor (GDM-F520) placed 25 cm from the animal's eyes. The video monitors had a non-interlaced refresh rate of 100Hz, a spatial resolution of 1024x768 pixels, which subtended 40x30 cm, and a mean luminance of 40 cd/cm2. Drifting gratings (38 deg diameter for imaging, variable diameter for electrophysiology, 0.01-0.04 spatial frequency, 100% contrast, 2 Hz temporal frequency) were presented for 2-3 sec. Each stimulus was followed by a 3 sec blank (mean luminance) period in the imaging protocol. Spontaneous activity was measured during blank (mean luminance) periods interleaved with drifting grating stimuli, all presented in a pseudorandom sequence. Direction presented ranged from 0-330 deg. Different spatial frequencies used were either presented individually in separate blocks or interleaved within the same block. Hartley stimuli were presented for each spatial frequency combination for 250 ms (Malone and Ringach, 2008; Ringach et al., 2016). For each spatial frequency combination four phases were presented and the response to these phases were averaged. These were repeated 5-30 times per cell. During imaging sessions, each stimulation protocol was repeated 7-10

times at each focal plane. The microscope objective and photomultiplier tubes were shielded from stray light and the video monitors.

Two-photon Calcium Imaging Analysis

Images were analyzed with custom Matlab software (Mathworks). Cells were identified by hand from structure images based on size, shape, and brightness. Cell masks were generated automatically following previous methods (Nauhaus et al., 2012). Glia were easily avoided due to their different morphology from both OGB-1 AM filled neurons. Time courses for individual neurons were extracted by summing pixel intensity values within cell masks in each frame. Responses (F_t) to each stimulus presentation were normalized by the response to the gray screen (F_0) immediately before the stimulus came on:

$$\Delta F/F = (F_t - F_0)/F_0$$

For each stimulus, the mean change in fluorescence $\Delta F/F$ was calculated in a 0.66 sec window of the response, identified by averaging responses to all stimuli and detecting the global peak. Visually responsive cells were identified if at least one orientation evoked a response with:

$$(\mu_{stimulus} - \mu_{spontaneous})/(SE_{stimulus} + SE_{spontaneous}) > 1$$

where $\mu_{stimulus}$ refers to the mean stimulus evoked response, $\mu_{spontaneous}$ refers to the mean spontaneous activity, $SE_{stimulus}$ is the stimulus evoked response standard error, and $SE_{spontaneous}$ is the spontaneous activity standard error. Additionally, identified responses were required to have distinct different trial-to-

trial fluorescence time courses, so as to not be scaled versions of neuropil activity. The maximum peak response for each cell was also required to have a response amplitude greater than 0.08. Mean changes in fluorescence from visually responsive neurons were used to generate tuning curves for orientation selectivity.

Electrophysiology Analysis:

Spiking responses for each stimulus were cycled-averaged across trials after removing the first cycle. The Fourier transform of mean cycle-average responses was used to calculate the mean (F0) and modulation amplitude (F1) of each cycle-averaged response, after mean spontaneous activity was subtracted. The subthreshold membrane potential responses were also similarly computed after median filtering the voltage traces to remove spikes. Peak responses were defined as the sum of the mean and modulation (F0 + F1).

Peak responses per trial across each condition for neuronal responses measured using electrophysiology and imaging were bootstrapped to compute the vector average orientation. This was used as the preferred orientation for the neuron. For electrophysiology, cells were only included in the analysis, if the bootstrapped confidence intervals on mean of the maximum amplitude spiking response did not include zero. A double Gaussian curve was fit to the responses for characterizing orientation tuning (Carandini and Ferster, 2000):

$$R(\theta) = \alpha e^{-(\theta - \theta_{pref})^2/(2\sigma^2)} + \beta e^{-(\theta - \theta_{pref} + \pi)^2/(2\sigma^2)} + k$$

Here R(θ) is the response of the neuron to different orientations (θ), σ is the width of the tuning curve, k is the mean activity, α and β are peak amplitudes,

and θ_{pref} is the orientation preference. Gaussian fits were used only for qualitative description of the tuning. The actual fit parameters have not been used in the analysis. The orientation selectivity index was also computed (Ringach et al., 2002; Tan et al., 2011):

$$OSI = \frac{\sqrt{(\sum R(\theta)\sin(2\theta))^2 + (\sum R(\theta)\cos(2\theta))^2}}{\sum R(\theta)}$$

The circular correlation (cc) between the preferred orientations (PO) is defined as:

$$cc = \frac{\sum_{i,j} \sin(PO_i - PO_j)\sin(PO'_i - PO'_j)}{\sqrt{\sum_{i,j} \sin^2(PO_i - PO_j)\sum_{i,j} \sin^2(PO'_i - PO'_j)}}$$

where PO_i is the preferred orientation of neuron i for one spatial frequency and PO'_i is the preferred orientation of the same neuron for another spatial frequency. This number is always in the range [-1:1], reaching 1 for perfect linear correlation between the preferred orientations in the two conditions.

To determine if the difference in the preferred orientations computed at different spatial frequencies was statistically significant, we generated bootstrapped confidence intervals on the both the preferred orientations being compared. The difference was considered significant if these intervals did not overlap.

The computational model of mouse V1

The model is composed of two networks. One represents LGN and has N_L neurons. The second network represents layer 4 and layer 2/3 in mouse V1. For simplicity these two layers are collapsed into one single network, with N_E

excitatory and N_I inhibitory neurons. In both networks the neurons are arranged on a square grid and the position (x_{iA}, y_{iA}), where (i,A) denotes the neuron i=1,...,N_A of population A=E,I,L. The position of neuron (i,A) is given by $x_{ia} = M\frac{i_x}{\sqrt{N_A}}; y_{ia} = M\frac{i_y}{\sqrt{N_A}}$ where M is the size of the network (2mm), $i_x = (i-1)\ mod\ \sqrt{N_A}$ and $i_y = \lfloor (i-1)/\sqrt{N_A} \rfloor$. Here $\lfloor x \rfloor$ is the largest integer equal to or smaller than x. All N_A are square integers so that i_x and i_y are integers between 0 and $\sqrt{N_A} - 1$. Unless said otherwise we take N_E=32400, N_I=8100, N_L=25600.

Cortical neurons:

They are described in terms of conductance-based models. The membrane potential of neuron (i,A), A=E,I, evolves in time according to

$$C\frac{dV_{iA}}{dt} = -I_{l,iA} - I_{Na,iA} - I_{K,iA} - I_{adapt,iA} + I_{LGN,iA} + I_{rec,iA} + I_{b,iA} \qquad (1)$$

where C is the membrane capacitance, $I_{l,iA}$, is the leak current, and $I_{Na,iA}$, $I_{K,iA}$ are the intrinsic sodium and potassium currents that shape the action potentials and $I_{adapt,iA}$ is an adaptation potassium current which included in E neurons, only. The dynamics of these currents are as in (Hansel and van Vreeswijk, 2012). The current $I_{LGN,iA}$ describes the input from LGN, $I_{rec,iA}$ is the recurrent input from other cortical neurons and $I_{back,\ iA}$ represents a background input from other cortical regions not explicitly included in the model.

LGN neurons

LGN cells are modeled as Poisson neurons with time varying rates that depend on the visual stimulus. Neuron (i,L) responds to a luminosity field L(x,y,t) with an instantaneous firing rate

$$r_{iL}(t) = \left[r_{sp} + \iint dxdy\ R_{il}(x,y)L(x,y,t)\right]_+ \qquad (2)$$

where r_{sp} is the spontaneous firing rate of the neuron, assumed to be the same for all LGN cells, $R_{iL}(x,y)$ is its receptive field and $[x]_+=x$ for $x>0$, $[x]_+=0$ for $x<0$. . The luminosity field of a sinusoidal drifting grating with orientation θ, spatial wavelength λ and temporal frequency ω is

$$L(x,y,t) = L_0[1 + \varepsilon\ \cos(k_x\, x + k_y y - \omega t)\ ] \qquad (3)$$

where L_0 is the average luminosity, □ is the contrast, and the wave-vector of the grating is: $\boldsymbol{k} = (k_x, k_y) = (k\ \cos\Theta, k\sin\Theta)$ with $k = 2\pi/\lambda$. The parameters used in our simulations are listed in Tables 1 and 2

The receptive field of neuron (i,L) has the form

$$R_{il}(x,y) = \pm R\left[\frac{\exp\left(-\frac{x'^2}{2\sigma_{cx}^2}-\frac{y'^2}{2\sigma_{cy}^2}\right)}{2\pi\sigma_{cx}\sigma_{cy}} - \gamma\frac{\exp\left(-\frac{x'^2}{2\sigma_{sx}^2}-\frac{y'^2}{2\sigma_{sy}^2}\right)}{2\pi\sigma_{sx}\sigma_{sy}} - U\right] \qquad (4)$$

where $x' = (x - x_{il})\cos\Theta_{iL} + (y - y_{il})\sin\Theta_{iL}$, $y' = -(x - x_{il})\sin\Theta_{iL} + (y - y_{il})\cos\Theta_{iL}$, γ is a parameter that controls the relative weights of the two subfields, U is a constant such that $\iint dx\,dy\,R_{il}(x,y) = 0$ and R is a constant (1 Hz). The long and short axis of the center (resp. surround) region are denoted here by σ_{cx} and σ_{cy} (resp. σ_{sx} and σ_{sy}). The global sign is +1 if the receptive field is ON center and -1 if it is OFF center. We take this sign at random with equal probability to be +1 or -1.

In all simulations except those in Supp. Fig. 8 we assume circular receptive fields for both center and surround subfields. In the simulations described in Supp Fig. 8 surrounds are circular but centers are elongated. We use the following

parametrization: $\sigma_{cx} = \sqrt{1+\alpha}\sigma,\ \sigma_{cy} = \frac{\sigma}{\sqrt{1+\alpha}}, \sigma_{sx} = \sigma_{sy} = \beta\sigma$ with $\sigma \equiv \sqrt{\sigma_{cx}\sigma_{cy}}$. Therefore, α =0 corresponds to a circular center and surround subfields. In this case the LGN cell is not selective to orientation. The degree of selectivity increases with α.

The response of the LGN cells to a drifting grating can then be calculated based on

$$r_{iL}(t) = \left[r_{sp} + \hat{r}_{iL}(\theta,\lambda)\cos\left(\omega t - \Delta_{iL}(\theta,\lambda)\right)\right]_+ \quad (5)$$

where

$$\hat{r}_{iL}(\theta,\lambda) = R\,L_0\,\exp\left(-\left(\frac{\sigma}{\lambda}\right)^2 (A + B\cos 2(\theta-\theta_{iL}))\right) - \gamma\exp\left(-\left(\beta\frac{\sigma}{\lambda}\right)^2 (1-\cos 2(\theta-\theta_{iL}))/2\right) \quad (6)$$

with $A = (\alpha^2+1)/2$ and $B = (\alpha^2-1)/2$.

The phase $\Delta_{iL}(\theta,\lambda)$ is: $\Delta_{iL}(\theta,\lambda) = 2\pi\,(x_{iL}\ \cos\Theta_{iL} + y_{iL}\ \sin\Theta_{iL})/\lambda$
($\Delta_{iL}(\theta,\lambda) = \pi + 2\pi\,(x_{iL}\ \cos\Theta_{iL} + y_{iL}\ \sin\Theta_{iL})/\lambda$) for an ON (OFF) cell.

Thalamo-cortical and recurrent connectivity:

The connectivity between model LGN and cortex is random and does not depend on the functional properties of the cells. The probability that cortical neuron (i,A) is connected to LGN cell (j,L) is

$$P_{ij,AL} = K_{AL} G\left(x_{iA} - x_{jL}, \sigma_{AL}\right) G\left(y_{iA} - y_{jL}, \sigma_{AL}\right) \qquad (7a)$$

Where K_{AL} is the mean number of LGN inputs received by a cortical cell in population A, and

$$G(x,\sigma) = \frac{1}{\sqrt{2\pi\sigma^2}} \sum_{k,l=-\infty}^{+\infty} \exp\left(-\frac{[x-Mk]^2}{2\sigma^2}\right) \qquad (7b)$$

is the periodic Gaussian with variance σ^2 .The recurrent interactions in the cortical network are also random and nonspecific. The probability of connection between neuron (j,B) and (i,A) (A=E,I; B=E,I) is

$$P_{ij,AB} = K_{AB} G\left(x_{iA} - x_{jB}, \sigma_{AB}\right) G\left(y_{iA} - y_{jB}, \sigma_{AB}\right). \qquad (8)$$

The feedforward and recurrent synaptic currents:

Thalamo-cortical synapses on cortical population A are all excitatory, have a reversal potential V_E, a strength g_{AL} and a synaptic time constant τ_L. The thalamo-cortical current, $I_{LGN,iA}$, in neuron (i,A) is

$$I_{LGN,iA}(t) = -g_{iL}(t)[\rho(V_{iA} - V_E) + (1-\rho)(V_L - V_E)] \qquad (9)$$

with: $g_{iL}(t) = \frac{g_{AL}}{\tau_L} \sum_{j=1}^{N_L} C_{ij}^{AL} \sum_k \exp\left(-\left(t - t_{k,j}\right)/\tau_L\right)$, where C^{AL} is the $N_A \, X \, N_L$ connectivity matrix of the thalamo-cortical projections ($C_{ij}^{AL} = 1$ if there is a connection from neuron (j,L) to neuron (i,A); $C_{ij}^{AL} = 0$ otherwise), and $t_{k,j}$ is the time of the k-th spike generated by neuron (j,L). The sum over k is over all the spikes with $t_{k,j} < t$.

The total recurrent current into neuron (I,A) is $I_{rec,iA} = I_{iA,E} + I_{iA,I}$ where

$$I_{iA,B} = -g_{iA,B}(t)[\rho(V_{iA} - V_B) + (1-\rho)(V_B - V_L)] \quad (10)$$

with $g_{iA,B}(t) = \frac{g_{AB}}{\tau_{AB}} \sum_{j=1}^{N_L} C_{ij}^{AB} \sum_k \exp\left(-\left(t - t_{k,j}\right)/\tau_{AB}\right)$.

Finally, the background current in Eq. (1) is modeled as

$$I_{b,iA} = -g_{b,iA}(t)[\rho(V_{iA} - V_E) + (1-\rho)(V_L - V_E)] \quad (11)$$

where $g_{b,iA}(t)$ is a random Gaussian variable with mean $K_b g_{\ b} r_0$ and variance $\sqrt{K_b} g_{\ b} r_0$. This represents the effect of K_b uncorrelated Poisson inputs, each of synaptic strength $g_{\ b}$.

Note that in Eqs. (9,10) the right hand-sides comprise two contributions. The first is proportional to the driving force $V_{iA} - V_B$. Thus, it modifies the input conductance of the neuron. This contrasts with the second contribution which does not depend on the membrane potential of the post-synaptic cell. We adopted this description to incorporate in a simplified manner the fact that the change in input conductance induced by a synapse depends on its location on the dendritic tree. Proximal synapses which substantially affect the neuron's input conductance are represented by the first contribution. The second contribution accounts for the synapses which are distal, and which affect the input conductance of the neuron less (see also Hansel and van Vreeswijk, 2012).

Numerical procedures and analysis:

Numerical simulations were performed using a 4th-order Runge-Kutta scheme to integrate the neuronal dynamics (Press, 1992). The synaptic interactions and the noise were treated at first order. The time step is $\delta t = 0.05ms$.

For each cortical neuron the mean firing rate, $F_0(\theta_k)$, and firing rate temporal modulation (first Fourier component of the response) $F_1(\theta_k)$ were estimated for each orientation, $\theta_k = (k-1)20°, k = 1,..,9$, by averaging the response upon 40s of stimulation, unless specified otherwise. We then computed the orientation averaged responses

$$\bar{F}_n = \frac{1}{9}\sum_{k=1}^{9} F_n(\theta_k) \quad n = 0,1$$

and the complex numbers

$$Z_n = \frac{1}{9}\sum_{k=1}^{9} F_n(\theta_k) e^{2i\theta_k} \quad n = 0,1$$

The Orientation Selectivity Index (OSI) and the Preferred Orientation (PO) of the peak response is then estimated from

$$OSI = \frac{|Z_0 + Z_1|}{\bar{F}_0 + \bar{F}_1}$$

$$PO = Arg(Z_0 + Z_1)$$

The OSI is 0 if the response has no tuning and 1 if the neuron responds at only one orientation. These definitions for the OSI and PO are equivalent to those used in the analysis of the experimental data (see above).

The definition of correlation coefficient is same as described above.

We also fit the tuning curves of the mean, $F_0(\theta)$, and temporal modulation, $F_1(\theta)$, of the spike to periodic Gaussian functions

$$\widetilde{F_n}(\theta) = A_n + B_n \sum_{k,l=-\infty}^{+\infty} \exp\left(-\frac{\left[\theta - k\pi - \hat{\theta}_n\right]^2}{2\,\sigma_n^2}\right)$$

with n=0,1. We estimated the parameters $A_n, B_n, \hat{\theta}_n$, σ_n , for each neuron by minimizing the quadratic error: $E\left(A_n, B_n, \hat{\theta}_n, \sigma_n\right) = \frac{1}{9}\sum_{k=1}^{9}\left(\widetilde{F_n}(\theta_k) - F_n(\theta_k)\right)^2$.

Robustness of the results:

To check that a time step, $\delta t = 0.05ms$, was sufficiently small, we also performed several simulations with $\delta t = 0.025ms$. To verify that our results were also robust to changes in system size we performed several simulations on networks with N_E=78560, N_I=19600, N_L=40000, keeping the average number of connections into E and I cells the same.

Structure of the ON and OFF subfield of the thalamic input:

We characterized the thalamo-cortical input in the model by performing simulations with a protocol similar to the one in the experiments of Lien & Scanziani (2013). The stimuli used to map the receptive fields were Gaussian spots with a standard deviation of 5.6 degrees. The spots were presented in one of 64 locations arranged regularly in a square of 8x8 in the center of the network. The distance between the centers of adjacent spots was 7°. In order to characterize both ON and OFF receptive fields the stimuli were either brighter or dimmer than the background illumination. Each stimulus was presented during 1sec . During that time, we evaluated the average of the conductance of the thalamic to each cortical neuron. We checked that the results were robust with respect to longer simulation times. The intensity of the stimulus (with respect to the background value) at the center of the Gaussian was I_0=±0.075. After performing the simulations, the centers of the ON and OFF subfields were

estimated by evaluating their center of mass: $\langle \mathbf{r} \rangle = \Sigma_i f_i \mathbf{r}_i / \Sigma_i f_i$, where f_i is the average thalamic input for a stimulus at position is $\mathbf{r}_i$. In order to reduce the noise level, we performed the sum only over the locations for which the average input is larger or equal than 30% of the maximal average input.

Let us note that this way of estimating the center of the fields is only valid for cortical neurons whose feedforward inputs do not come from the border of the LGN network. Otherwise, because of the periodic boundary conditions of the LGN receptive fields, the linear estimation could combine inputs from opposite sides of the visual field. As the feedforward connectivity profile is topographically organized, neurons in the center of the cortex receive inputs from neurons in the center of the LGN. Therefore, boundary effects can be avoided by evaluating the center of mass only for neurons in the central part of the cortical network. In particular all the statistics of the ON and OFF subfields were estimated from neurons the square region of 14°x14° at the center of the network (361 neurons).

Parameters of the computational model:

The cortical network is assumed to have a size of 2mm x 2mm representing 140^0x 140^0 in the visual field(Kalatsky and Stryker, 2003).

The synaptic dispersion of the recurrent connectivity is taken to be 200 μm, consistently with values reported in Reyes & Sakmann, 1999 (Reyes and Sakmann, 1999). Unless indicated otherwise, the dispersion of the feed-forward connectivity was 100 μm.

The synaptic efficacies were as in Table 1. With these parameter values post-synaptic potentials have peak size is 0.5 mV (E->E interaction), -0.3 mV (I->E), 2.7 mV (E->I), -0.9 mV (I->I), 0.9 mV (LGN->E), 0.8 mV (LGN->I). See Supplementary Figure 1a.

We introduced heterogeneity in the parameters σ_{cx}, σ_{sx}, α, β. For each thalamic neuron these parameters were chosen from a log-normal distribution

$$P(x) = \frac{1}{x\, s\, \sqrt{2\pi}}\, e^{-\frac{(\ln x - m)^2}{2\, s^2}}$$

where the parameters m and s are given by σ_{cxm}, σ_{cxs}, σ_{sxm}, σ_{sxs}, α_m, α_s, β_m, β_s respectively. The values of these parameters are given in Table 2. Examples of receptive fields of LGN neurons in the model are plotted in Supp. Fig. 1B. The heterogeneity in the LGN receptive fields is depicted in Supp. Fig. 1C.

In the simulations of Fig. 2.9, the preferred orientations of LGN neurons are chosen randomly with a distribution

$$P(\theta) = P_0 \left[a_\theta + b_\theta \exp(-\frac{\theta^2}{2{c_\theta}^2})\right]$$

where P_0 is a normalization constant. The parameters we used in these simulations are given in Table 3.

N_E	32400
N_I	8100
K_{AB} (A,B=E,I)	500
K_{EL}	25
K_{IL}	100
g_{EE}	0.011 ms mS/cm^2
g_{IE}	0.067 ms mS/cm^2
g_{EI}	0.029 ms mS/cm^2
g_{II}	0.098 ms mS/cm^2
g_{EL}	0.04 ms mS/cm^2
g_{iL}	0.02 ms mS/cm^2
τ_{AB}(A=E,I ; B=E,I,L)	3 ms
σ_{AB} (A,B=E,I)	200 μm
σ_{AL} (A=E,I)	100 μm
V_E	0 mV
V_I	-80 mV
V_L	-65 mV
ρ	0.5
K_b	500
g_b	0
r_0	1 Hz
L_0	0.075
ε	1

Table 2.1: Default parameters of the computational model of mouse V1 (Layer 4 and stimulus).

N_L	25600
r_{sp}	1 Hz
□	1
σ_{cxm} (*)	1.3
$\sigma_{sxm}(*)$	2.7
β_m	0.05
σ_{cxs}(*)	0.2
$\sigma_{sxs}(*)$	0.2
β_s	0.45

Table 2.2: continued next page

Table 2.2: Parameters of the computational model of mouse V1: default values for the LGN cells.

α_m	0
α_s	0.2
a_θ	142
b_θ	1128
c_θ	21.5 deg

Table 2.3: Parameters of the computational model of mouse V1: elongated receptive fields of LGN cells.

(*) Parameters of the log-normal distribution are normalized to obtain values in degrees.

Chapter 3: Thalamic and cortical contributions to simple and complex cells in mouse visual cortex

SUMMARY

Simple and complex cells are distinct stages of cortical processing in carnivores and primates. The basis for the difference in the cell type lies in a circuit hierarchy in which simple cells emerge from the integration of thalamic inputs, and complex cells emerge from the integration of cortical inputs. Here, we study the synaptic differences in simple and complex cells characterized by different degrees of nonlinear responses, in the mouse visual cortex. We find that as proposed in the hierarchical model, some complex cells in the mouse V1 do not receive any thalamic input and orientation selectivity of many simple cells is matched to the thalamic input orientation selectivity. But, in contrast to the hierarchical model, we find that a majority of mouse V1 neurons receive direct thalamic input. When this input is incident on the complex cells, this aggregate thalamic input can also be nonlinear. In addition, the thalamic responses also show signatures of input from orientation selective LGN cells, which contribute to orientation tuning of the target cell. Our results demonstrate alternate connectivity models in the mouse visual pathway which underlie the generation of simple and complex cells.

INTRODUCTION

The cerebral cortex implements remarkable transformations on the incoming sensory information to generate representations to guide behavior. It does so, using a common neural circuit composed of neurons arranged into six layers which form cortical columns. There has been intense focus on the

computations focusing in the primary visual cortex because within V1 visual information is transformed systematically. Hubel and Wiesel not only described the emergence of orientation, direction and binocular sensitivity, but they described two functional classes of V1 neurons (Hubel and Wiesel, 1962). The first class of neurons exhibit receptive fields that are roughly linear: mapping the spatial and temporal sensitivity predicts their selectivity for orientation, direction and binocularity. The second class of neurons maintain these selectivities, but their spatiotemporal receptive fields no longer predicts selectivity. These cells exhibit nonlinear receptive fields in which responses are insensitive to the polarity of light thus providing signals for orientation, motion and object depth invariant to the particular lighting of visual objects.

Hubel and Wiesel proposed a hierarchical model to account for these two classes of neurons (Hubel and Wiesel, 1962). They suggested that simple cells derive their spatial preferences from the convergence of thalamic inputs with spatially offset receptive fields. Consistent with this hypothesis, simple cells lie in the thalamorecipient layer of cat visual cortex, layer 4, and convergent inputs from LGN neurons matches their response selectivity (Hirsch, 1992; Reid and Alonso, 1995; Martinez et al., 2005). In a second stage of processing simple cells which share orientation preference but with spatially offset receptive fields converge on complex cells, allowing these neurons to respond selectively in a manner that is invariant to light polarity. In support of this hierarchical model, complex cells in the cat visual cortex generally lie outside of the thalamorecipient layers (Martinez et al., 2005), and the inactivation of simple cells leads to the silencing of complex cells (Martinez and Alonso, 2001).

These observations establish that the emergence of complex cells as a cortical process, as with the emergence of selectivity for orientation, direction and binocularity from cat visual cortex. Recent measurements from the mouse visual system, however, demonstrate that at least some of the properties that have been ascribed to the visual cortex exist in the retina and the visual thalamus (Piscopo et al., 2013; Scholl et al., 2013; Cruz-Martin et al., 2014). For example, selectivity for orientation and direction exist in the thalamus and we know that inputs from the two eyes can converge on thalamic relay cells (Howarth et al., 2014). Furthermore, almost all layers of mouse V1 receive direct input from the thalamus, instead of the more restricted thalamocortical targeting found in cat V1. The impact of these thalamic selectivities and their divergent laminar targets on cortical processing is under scrutiny and has raised the question of whether the emergence of complex cell responses in mouse V1 might be derived from thalamic inputs instead of the cortical hierarchy model.

MATERIALS AND METHODS

Experiments were conducted in transgenic PV-ChR2 adult male and female animals (P45-120). All procedures were approved by The University of Texas at Austin Institutional Animal Care and Use Committee.

Physiology

Procedures for physiology were based on those previously described (Scholl et al, 2013, Pattadkal et al., 2018). Mice were anesthetized with intraperitoneal injections of 1000 mg/kg urethane and 10 mg/kg chlorprothixene.

Brain edema was prevented by intraperitoneal injection of up to 10 mg/kg dexamethasone. Animals were warmed with a thermostatically controlled heat lamp to maintain body temperature at 37°C. A tracheotomy was performed, and the head was placed in a mouse adaptor (Stoelting). A craniotomy and duratomy were performed over visual cortex. Eyes were kept moist with a thin layer of silicone oil. Primary visual cortex was located and mapped by multi-unit extracellular recordings with tungsten electrodes (1 mΩ, Micro Probes). The V1/V2 boundary was identified by the characteristic gradient in receptive locations (Drager, 1975; Metin et al., 1988). Eye drift under urethane anesthesia is typically small and results in a change in eye position of less than 2 degrees per hour (Sarnaik et al., 2014).

Intracellular recordings

Glass patch electrodes (5–9 MΩ) filled with a potassium-gluconate-based solution were used to record from neurons in the whole-cell configuration. Raw membrane potential records were split into two channels: the subthreshold responses that resulted after first removing the action potentials using a median filter; the suprathreshold action potentials identified by the characteristic large amplitude changes in membrane potential. Recordings were conducted both in current clamp mode, where the holding current was 0 and in the voltage clamp mode where the cell was held at -70 mV.

Stimuli

Visual stimuli were generated by a Macintosh computer (Apple) using the Psychophysics Toolbox (Brainard, 1997; Pelli, 1997) for MATLAB (MathWorks)

and presented using Sony video monitors (GDM-F520) placed 38 cm from the animal's eyes. The video monitors had a noninterlaced refresh rate of 100 Hz and a spatial resolution of 1024 × 768 pixels, which subtended 40 × 30 cm (58 × 46 deg). The video monitors had a mean luminance of 40 cd/cm2. Sinusoidal gratings of 0.04 cpd were used in all protocols. These gratings were either used in drifting grating configuration or in static contrast reversal configuration. Stimulus in each case was presented for 2 s long, preceded and followed by a 0.5 s period of blank screen. For drifting gratings, the temporal frequency used was 2 Hz. These were either presented across multiple orientations (0 to 330 in steps of 30 degrees) to assess orientation selectivity or at a single preferred orientation of the recorded cell. For counterphase gratings, stimulus orientation used was the preferred orientation of the cell estimated from drifting grating responses. The static gratings were presented at either 4 or 8 regularly spaced spatial phases. The frequency for contrast reversal was also 2 Hz. There was also a blank condition, when only gray screen was presented. All stimuli were presented to the contralateral eye and different trial conditions were interleaved.

Optical stimulation

A blue LED was placed over the craniotomy that illuminated the entire exposed brain surface. In conditions in which the cortex is inactivated, the LED was triggered on 100 ms after the trial start and 400 ms before the start of the stimulus. The LED was turned off 100 ms following end of the stimulus. The inactivation trials were always interleaved with the normal trials.

Analysis

Responses of the cells were cycle averaged across trials. The Fourier transform of mean cycle-average responses was used to calculate the mean (F0) and modulation amplitude (F1) of each cycle-averaged response, after mean spontaneous activity was subtracted. The subthreshold membrane potential responses were also similarly computed after median filtering the voltage traces to remove spikes. Peak responses were defined as the sum of the mean and modulation (F0 + F1). Each neuron analyzed passed a visual response criterion based on an ANOVA between spontaneous firing rate during blank periods and visual stimuli. Peak responses across orientations (Θ) were fit with two Gaussian curves of the same variance (σ^2), but two different amplitudes (α and β):

$$R(\theta) = \alpha e^{-(\theta - \theta_{pref})^2/(2\sigma^2)} + \beta e^{-(\theta - \theta_{pref} + \pi)^2/(2\sigma^2)} + k$$

The second Gaussian (β) was constrained to be 180° phase-shifted from the preferred orientation (Θ_{pref}). A DC component was also included. Gaussian fits were used only for qualitative quantification of orientation tuning curves. Orientation preference was calculated based on the vector average of the peak responses across orientations. Modulation ratio of cells was computed as F1/F0.

For the counterphase gratings analysis, Fourier transform of the mean responses was used to generate F1 and F2 amplitudes at each spatial phase. The F1 modulation of the F1 amplitudes was then extracted to estimate the linear component. The mean of F2 across all spatial phases was taken as the estimate of the nonlinear component. The ratio of these two quantities was taken as the nonlinearity index.

Response significance of thalamic inputs was assessed by bootstrapping mean values in stimulus evoked and blank conditions. An overlap in bootstrap confidence intervals of the evoked and baseline values was assigned as nonsignificant thalamic input.

Cortical responses were estimated as the difference between the total response and its thalamic components. The mean and modulation values for cortical responses were also computed as stated above.

RESULTS

We are interested in identifying the set of circuit rules in the mouse V1 that are responsible for receptive fields that vary in their linearity and selectivity. The classical model for the emergence of orientation selectivity and simple and complex cells in V1 is composed of two distinct stages (Fig. 3.1A). Thalamic relay cells with circularly-symmetric receptive fields provide input by converge on cortical simple cells in the first stage of processing. The spatial arrangement of their receptive fields provides cortical simple cells with orientation selectivity. These simple cells are characterized by linear receptive fields that are followed by an output rectification nonlinearity. That is, their responses are sensitive to the polarity of light that is presented, and they generally exhibit spatially offset preferences for ON and OFF stimuli. In a second stage of processing orientation-selective complex cells are generated by integrating the responses of simple cells with the same orientation preference, but spatially offset receptive fields. This circuit allows these neurons to be sensitive for orientation, in a manner that

is invariant to spatial position and polarity. To examine whether this functional connectivity scheme exists in mice we isolated the thalamic and cortical contributions to the responses of individual neurons using a combination of light-induced cortical silencing and whole cell recordings. Cortical silencing was accomplished using transgenic mice in which PV+ neurons express ChR2. Blue light activates these inhibitory neurons and effectively inactivates the remaining cortical cells (Lien and Scanziani, 2013, 2018) isolating the thalamic input, to which we have access with intracellular recordings.

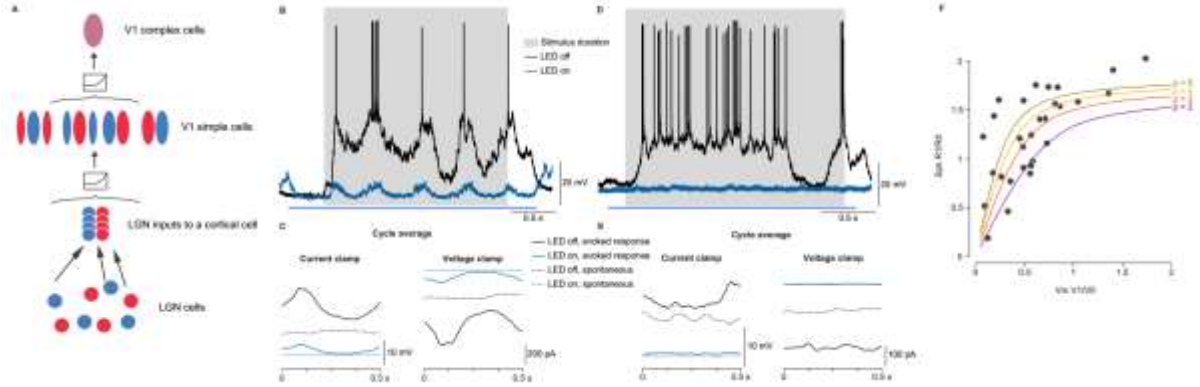

Figure 3.1: Hierarchical model, example cells and membrane potential to spiking nonlinearity for modulation ratios.

A: The hierarchical model by Hubel and Wiesel to explain emergence of simple and complex cells. B, D: Example recording from a simple cell (B) and a complex cell (D), with (blue) and without (black) cortical inactivation. Grey region depicts stimulus duration. C, E: Cycle averaged responses from the cells in B and D respectively, under current clamp (left) and voltage clamp (right) conditions. Responses in black are without cortical inactivation. Responses in blue are during cortical inactivation. Solid lines are responses to the stimulus, dotted lines are responses to blank screen. F: Modulation ratio for responses to drifting gratings for spiking responses vs membrane potential demonstrates a nonlinear relation. Colored lines are power law model with different exponents (p = 2 for purple, 3 for orange, 4 for yellow, 5 for green).

We first classified mouse V1 neurons in the intact circuit by measuring the responses to drifting sine wave gratings and quantifying the relative magnitudes of the mean and the modulation of the evoked response (Movshon et al., 1978b, a; Skottun et al., 1991). A cell which shows a higher modulation in the spiking response to a drifting grating than an increase in the mean spiking response (F1/F0>1) is classified as a simple cell (Fig. 3.1B-C). In contrast, a cell which responds with a larger mean spiking response than modulation (F1/F0<1) to a drifting grating is classified as a complex cell. This elevated mean response reflects the spatial overlap of the ON and OFF portions of the receptive field (Fig. 3.1D-E). Because we are performing intracellular recordings, we have access to both the subthreshold and suprathreshold responses and the corresponding modulation ratios. Modulation ratios for membrane potential and spike rate varied between 0 and 2 and are related in a nonlinear fashion (Fig. 3.1F, n = 29). A simple power law nonlinearity that transforms membrane potential into spike rate recapitulates the nonlinear relationship between the sub- and suprathresold modulation ratios, as happens in carnivores and primates (Priebe et al., 2004; Tan et al., 2014). The modulation ratio based on membrane potential is smaller than that found from spike rate (median V1/V0 = 0.56, mean R1/R0 = 1.24, two sample KS test, P = 3 x 10-6). For simplicity, we chose a criterion membrane potential modulation ratio of 0.5 to classify neurons as simple or complex, though we recognize that the distribution of this membrane potential modulation ratio in mouse V1 neurons is not bimodal (Dip test statistic = 0.05, p value = 0.67).

Thalamic input to simple and complex cells

A central component of the hierarchical model proposed by Hubel and Wiesel is that thalamic neurons provide input to simple cells and simple cells provide input to complex cells. To determine the relative contributions of the thalamic and cortical circuitry to the emergence of simple and complex responses in the mouse visual system, we used optogenetics to inactivate cortical responses. Using optogenetics to silence V1 while recording intracellularly from cortical neurons allows us to isolate and characterize the aggregate thalamic input each cell receives.

We quantified the fraction of thalamic input to a cell by recording from neurons while voltage clamping their membrane potential at -70 mV (Fig. 3.1 C, E). We compared the recorded currents to visual stimulation in the presence or absence of optogenetic stimulation, providing measurements of the thalamic and total synaptic drive. We computed the ratio of the mean thalamic input to the mean total input (TR: thalamic ratio) from these measurements (Fig. 3.2 A, B) (Lien and Scanziani, 2013). Across our sample population we found V1 cells received varying degrees of thalamic input. Some cells are dominated by their thalamic input (e.g. TR = 0.72, Fig 3.2 C) whereas others received little to no thalamic input, as indicated by visually-evoked responses during optogenetic stimulation of PV+ neurons that were not statistically significant than the response to a blank screen (Fig. 3.2 C, black symbols).

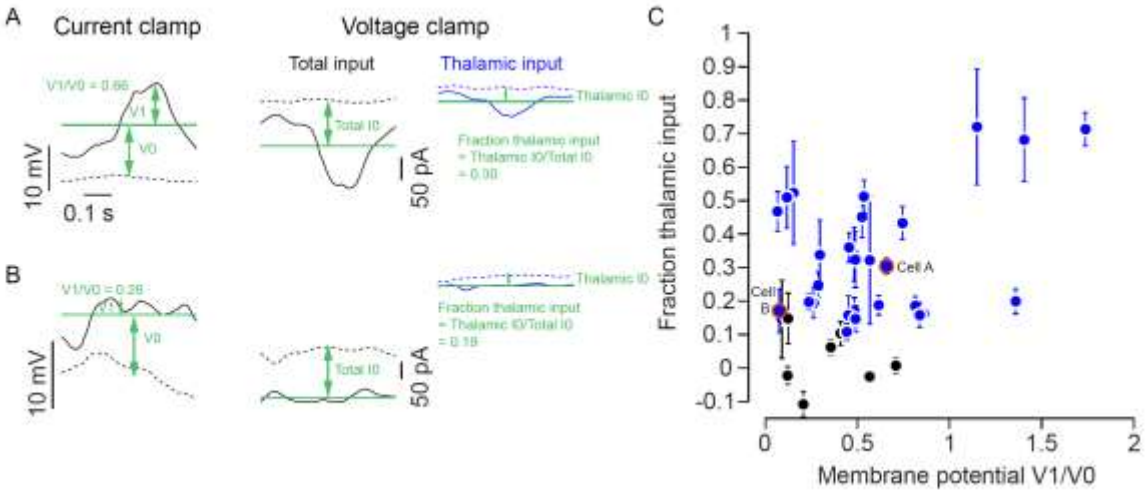

Figure 3.2: Thalamic input to cells varying degrees of nonlinearity.

A, B: Cycle average responses from two cells (A and B) showing the computation of membrane potential modulation ratio (V1/V0) in current clamp on the left. On the right side are responses in voltage clamps showing total input (black) and thalamic input (blue). The mean values of these inputs are used to compute the thalamic ratio (TR). C: Population summary of thalamic ratio as a function of membrane potential modulation ratio. Black points are cells without significant thalamic inputs. Error bars are standard deviation of the bootstrapped ratios.

As expected from the hierarchical model, we find a relationship between cell class and the amount of direct innervation from the thalamus. Simple cells (with V1/V0>0.5) exhibited a larger TR (mean = 0.30 +/- s.d. 0.24, n = 15) than complex cells (median = 0.17 +/- s.d. 0.16, n= 21), but the difference was not statistically significant (two sample KS test p = 0.54). In further agreement with the hierarchical model, those neurons that receive direct thalamic input have a higher modulation ratio (mean V1/V0 = 0.59 +/- s.d. 0.41, two sample KS test p = 0.04) whereas, neurons that receive only cortical input have a low membrane potential modulation ratio (mean = 0.32 +/- s.d. 0.22, n = 8). Out of these 8 cells

that did not receive thalamic input, all but two were classified as complex cells. These measurements demonstrate that those mouse V1 cells that only receive cortical input tend to have nonlinear, complex response profiles.

While these observations are in general agreement with the hierarchical model, there are notable deviations from the hierarchical model in our sample population. One of these deviations is the observation that some simple cells did not receive thalamic inputs (n = 2/15). These were very few in number but suggest a difference from classical connectivity pattern proposed by Hubel and Wiesel. The second deviation is that the majority of complex cells receive direct thalamic input (n = 15/21). We find that a majority of cells in our sample population receive some thalamic input (n = 28/36). While simple cells are more likely to receive direct thalamic input, and the degree of their thalamic innervation is stronger (simple cells: mean thalamic input = 0.39, s.d = 0.22, n = 13, complex cells: mean thalamic input = 0.29, s.d. = 0.14, n = 15), it is nonetheless the case that complex cells also receive a substantial thalamic input. Among those cells that received direct thalamic input there were only mild differences in the TR (simple cells: mean thalamic input = 0.39, s.d = 0.22, n = 13, complex cells: mean thalamic input = 0.29, s.d. = 0.14, n = 15) which was not statistically significant (Two sample KS test, p = 0.66). The presence of these thalamorecipient complex cells indicates the presence of a circuitry motif that is distinct from the hierarchical model.

Models for the emergence of complex cells

The presence of direct thalamic input onto complex cells may have consequences for the selectivity and circuitry of these cells. We describe three circuit motifs from which the nonlinear complex cell responses may emerge (Fig. 3.3). The first possibility is that the thalamic input is linear and the non-linearity in receptive fields for complex cells arises out of recurrent cortical inputs (Fig. 3.3 A) (Chance et al., 1999; Tao et al., 2004; Yunzab et al., 2019). If this circuit underlies the emergence of complex cells, then we would expect that the modulation ratio of the thalamic input would be higher than the modulation ratio of the cortical inputs. A second possibility is that the thalamic input itself is nonlinear and can form the basis of overall nonlinearity of the complex cells. If this were true, then it might impact the orientation selectivity these cells exhibit. If the thalamic input is composed of afferent with overlapping ON and OFF receptive fields, a complex response will be observed in the target V1 neuron, but this neuron would lack orientation selectivity (Fig 3.3 B). Under the original hierarchical model proposal, the computation of orientation selectivity occurs at a stage prior to the generation of nonlinear responses thereby separating these computations (Fig. 3.1A). An intervening rectification nonlinearity provided by the simple cells, allows for orientation selectivity to be maintained, while generating spatially invariant responses. To construct a complex receptive field that is also orientation tuned, cells need to rely on inputs from orientation selective inputs. This would occur if the thalamic input is nonlinear and orientation-tuned (Fig. 3.3 C). This would then lead to the conclusion that the thalamic receptive fields being used are not circular but already exhibit an orientation bias. Orientation-selective

cells are known to exist in mouse LGN and under this case, it would imply that these cells provide input to cortical complex cells.

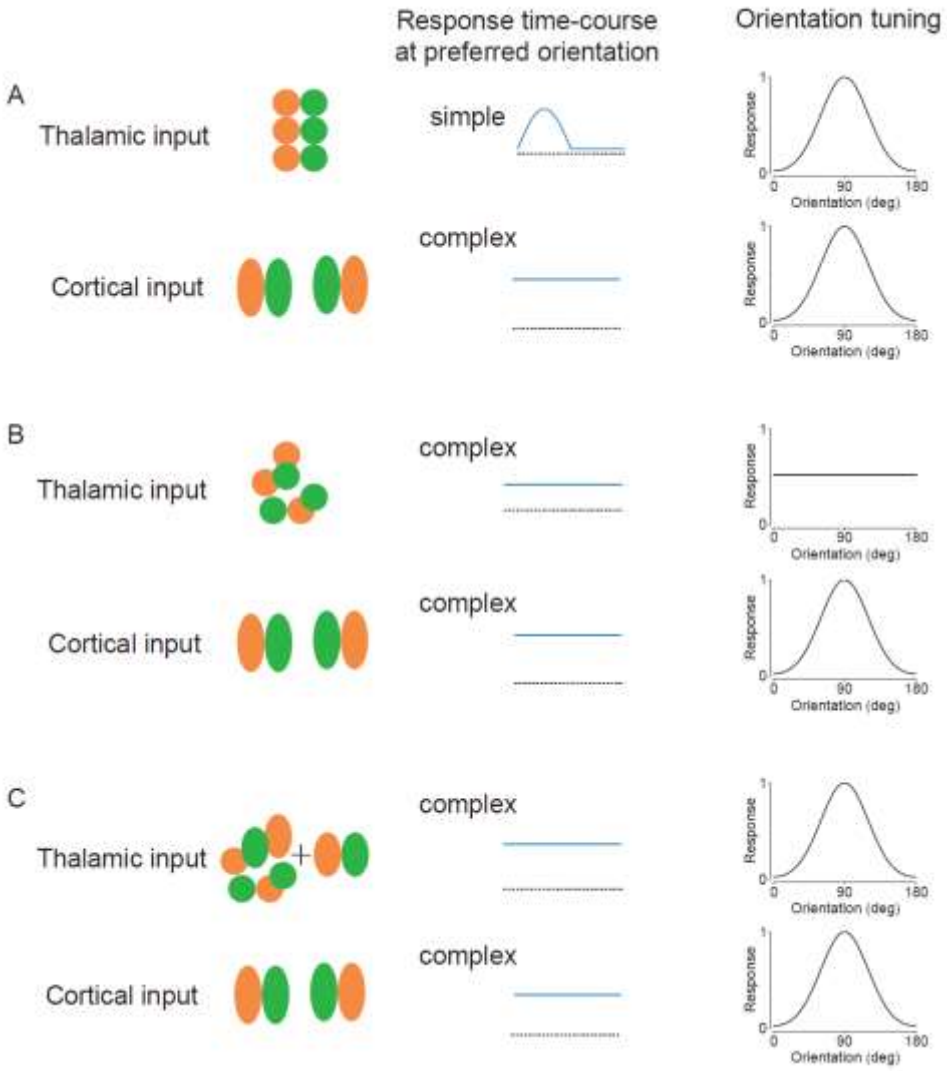

Figure 3.3: Schematic models for emergence of complex cells.

Thalamic and cortical input cartoons are shown on the left, their response time-course is shown in the middle column and their orientation tuning is shown in the rightmost column. A: Under this scenario, thalamic input can only be simple and orientation selective. Cortical input generates complexity in the responses and maintains the orientation preference. B: Under this case, both thalamic and

cortical inputs are complex. Since lack of segregation in ON and OFF fields causes complex thalamic responses, these responses are not orientation selective. C: Under this case, thalamic inputs use orientation-tuned LGN cells. As a result, thalamic responses can be complex and orientation selective. (Fig. 3.3. continued).

Linear and nonlinear components of thalamic input

Since we have uncovered direct connectivity between the thalamus and V1 neurons in simple and complex cells, we next examined the relationship between the response nonlinear responses cortical neurons relative to their thalamic input. To assess the relationship between the relative nonlinearity of cortical responses and their thalamic inputs, we compared the modulation ratios of the measured thalamic input and total input elicited by drifting gratings. For the example simple cell, the thalamic input to the neuron, evident during optogenetic silencing of the cortex, modulates in a similar manner as the modulation that is evoked by visual stimulation when the cortex is intact (Fig. 3.4 A). When we isolated the thalamic input onto cortical complex cells (Fig. 3.4 B), we found that the thalamic input had a similar modulation ratio as the target complex cell. We examined the relationship between modulation ratio for thalamic and total synaptic input across all of the neurons in our sample population and found a high correlation (Fig. 3.4 C, correlation coefficient = 0.54, n = 28), indicating that the degree to which the thalamus provide nonlinear input is preserved in the total response, including the cortical inputs. The strong relationship between the characteristics of the thalamic and total synaptic input could arise if the thalamic input were strong relative to the total synaptic input. Alternatively, the cortical synaptic input could have a similar nonlinear response as the thalamic input. To compare the cortical and thalamic input nonlinearity, we

estimated the cortical input in these cells by subtracting the response when the cortex is inactivated (thalamic input) from the response when the cortex is active (total input) (Fig 3.4 A, B). The resulting relationship was less correlated (Fig. 3.4 D, correlation coefficient = 0.21, n = 28), indicating a weaker match between response linearity of thalamic and cortical inputs to a cell. Nonetheless, there were overall differences in the degree of nonlinearity that characterizes thalamic input onto simple and complex cells. Simple cells receive thalamic input characterized with a high modulation ratio (median = 0.83 +/- s.d. 0.31), whereas complex cells received input with significantly less F1/F0 (median = 0.24 +/- s.d. 0.17, two sample KS test, $p = 4.3 \times 10^{-5}$).

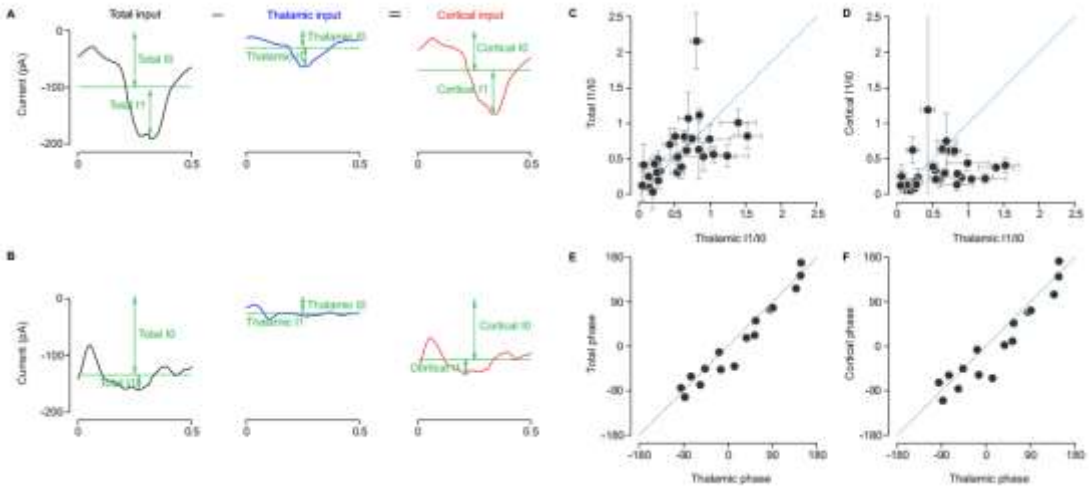

Figure 3.4: Modulation ratios and phase preferences for thalamic, total and cortical inputs.

A, B: Cycle average responses from two example cells showing estimation of cortical inputs (red) by subtracting thalamic (blue) response from the total inputs (black). The modulation ratio (I1/I0) is computed from these voltage clamp responses. C: Comparison of modulation ratio for total vs thalamic inputs. Error bars are standard deviation of the bootstrapped median ratio. D: Comparison of modulation ratio for cortical vs thalamic inputs. Error bars are standard deviation of the bootstrapped median ratio. E: Comparison of spatial phase preference for

total and thalamic inputs for simple cells. F: Comparison of spatial phase preference for cortical and thalamic inputs for simple cells. (Fig. 3.4. continued).

We not only noted a relationship between the modulation ratios of the thalamic input to cortical neurons, we also found a tight match between dynamics of the visually evoked thalamic input relative to target cortical cell. For the cells with simple cell responses (V1/V0 > 0.5, n = 16), the total thalamic input is modulated at a characteristic phase relative to the stimulus (Fig. 3.4 A). We compared the response phase of the thalamic input to both the total input (Fig. 3.4 E) and the extracted cortical input (Fig. 3.4 F). We find that modulation phase of thalamic inputs was very similar to both the total synaptic input (circular correlation: 0.92, n = 16) and the cortical synaptic input (circular correlation = 0.85). In sum, both the degree of modulation of V1 neurons and their dynamics matches their thalamic inputs. These observations, however, reflect evidence both for and against the hierarchical model. Evidence for this model is that simple cells receive linear input that modulate at the same temporal phase as their inputs. In contrast, the presence of direct input onto complex cells from the thalamus that exhibit nonlinear responses is not consistent with the hierarchical model.

The mean and modulated responses to drifting gratings have been extensively used to describe relative nonlinearity of visual neurons. As a cortical neuron increases it modulation amplitude, however, the mean also increases. An alternative method that compares two modulated responses, and for which there is not a link between the underlying metrics, is to compare the first and second

modulation amplitude to stationary contrast-modulated gratings. The counterphase grating stimulus has been used previously to study the nonlinear spatial summation responses in the retina (Enroth-Cugell and Robson, 1966; Hochstein and Shapley, 1976), LGN (Shapley and Hochstein, 1975) and V1 in cats (Movshon et al., 1978b), primates (Hawken and Parker, 1987) and mice (Yunzab et al., 2019). Cells which have strictly linear spatial summation should only respond at the stimulus frequency of contrast reversal and the timing and amplitude of the response should be dependent on the spatial phase of the stationary grating (Fig. 3.5 A, left). Any non-linearity in spatial summation in the receptive field will lead to ON-OFF responses causing some power at even harmonics of the stimulus frequency. A cell with a spatially invariant receptive field, as in a complex cell, the timing of the even harmonic should not depend on the spatial phase of the stimulus (Fig. 3.5 A, right). The presence of response modulation at the even harmonic is an indication of non-linear spatial summation in the receptive fields. One can then distinguish simple and complex cells by considering the first and second Fourier components in the complex plane (Fig. 3.5 B). Simple cells should have large F1 components that lie along an axis in the complex plane. For the example simple cell, that axis is along the abscissa. In contrast, the example complex cell has small F1 component, but a large F2 component for which the response does not change with the stimulus phase. To extract a metric that describes the relative F1 and F2 modulations of the responses, we computed the amplitude of the projection of the F1 values onto their principal axis in the complex plane, and compared that to the vector average F2 value in the complex plane (Yunzab et al., 2019). Doing so enforces

the expectation that the timing of the F2 component should be invariant to spatial phase. The resulting contrast reversing modulation index (F2/F1) is large for complex cells and small for simple cells.

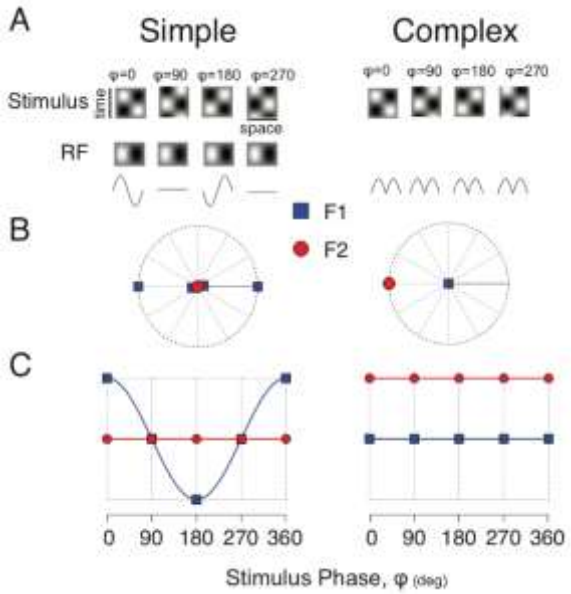

Figure 3.5: Use of counterphase gratings to estimate response nonlinearity.

A: Responses of a model simple cell (left) and a model complex cell (right) to static contrast reversing gratings at 4 different spatial phases. Simple cell shows modulation at stimulus frequency for preferred and anti-preferred phases and no response at null phases. Complex cell modulates at twice the contrast reversal frequency at all spatial phases. B: Polar plot of response modulation at the contrast reversal frequency (F1 in blue) and twice that frequency (F2 in red). Simple cell has F1 values that modulate around an axis in this complex plane. F2 values are at zero, because of lack of modulation at twice the stimulus frequency. Complex cell only has F2 values. C: F1 and F2 modulation of responses as a function of spatial phase of stimulus. Simple cell shows sinusoidal modulation for F1 values. Complex cell has a constant F2 modulation at all phases.

Example responses from a cell to 8 different spatial phases of counterphase gratings is shown in Fig 3.6 A. Within each cycle of the grating, the

responses are modulated twice, indicating a response to both ON and OFF phases of the contrast modulation. The response modulation at the frequency of the contrast reversal (F1 response) and modulation at twice this frequency (F2 response) are plotted as a function of spatial phase in Fig 3.6 C. Note that the F1 response varies with the spatial phase of the counterphase gratings, whereas the F2 phase is invariant to spatial position. This neuron exhibits both F1 and F2 components, but is dominated by the F2 component, thus indicating that it is a complex cell.

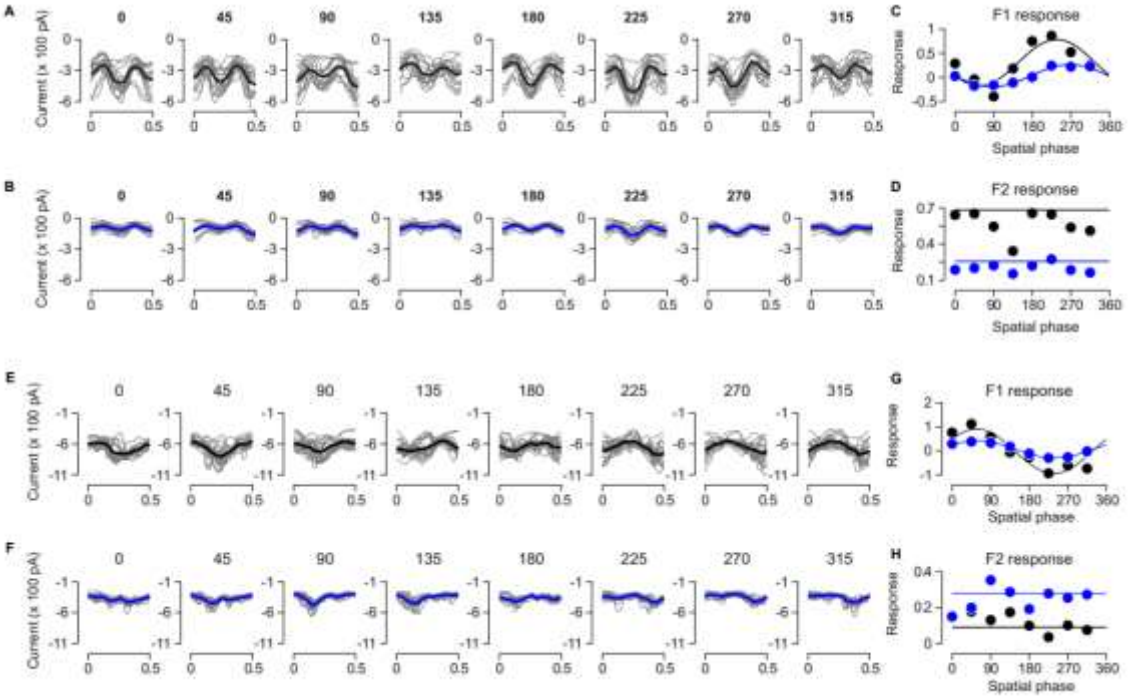

Figure 3.6: Example responses to counterphase gratings.

Cell 1 responses are shown in A-D, cell 2 responses are shown in E-H. A, E: Responses for 8 different spatial phases under voltage clamp. Response average is shown in black. Individual repeats are shown in grey. B, F: Responses of the cells when the cortex is inactivated. Response average is shown in blue, individual repeats in grey. C, G: Modulation at the contrast reversal frequency

(F1) as a function of stimulus spatial phase for total inputs in black and thalamic inputs in blue. D, H: Modulation at twice the contrast reversal frequency (F2) as a function of stimulus spatial phase for total inputs in black and thalamic inputs in blue. (Fig. 3.6. continued).

We then silenced the cortex to study whether the response nonlinearity evident in the large F2 modulation is also present in the thalamic inputs (Fig 3.6 B). For this example neuron silencing cortex dramatically reduced the input magnitude, but the modulation at twice the frequency of the contrast modulation is still evident. These data support our previous measure using F1/F0 to drifting gratings, that complex cells receive an aggregate input from thalamus with similar complexity. An additional simple cell shows a different behavior, in which there is little F2 modulation across stimulus phases, but there is a large F1 component, which depends systematically on the stimulus phase (Fig. 3.6 E-H).

To generate a measure of the relative linear and nonlinear components of the response we computed the F2/F1 of the responses across stimulus phase (see Methods). We compared the magnitude of F2/F1 responses for thalamic and cortical components in our sample population (Fig. 3.7). We find that both thalamic and cortical inputs can exhibit F2 responses suggesting that nonlinearity in receptive field can emerge from both thalamic and cortical inputs. We also do not find any bias in thalamic F2/F1 responses towards lower values, which would be the expectation if thalamic input was largely simple in nature. The F2/F1 responses at thalamic and cortical levels are also correlated with each other (correlation coefficient = 0.40, n = 17) indicating that recurrent inputs roughly

preserve the nonlinearity.

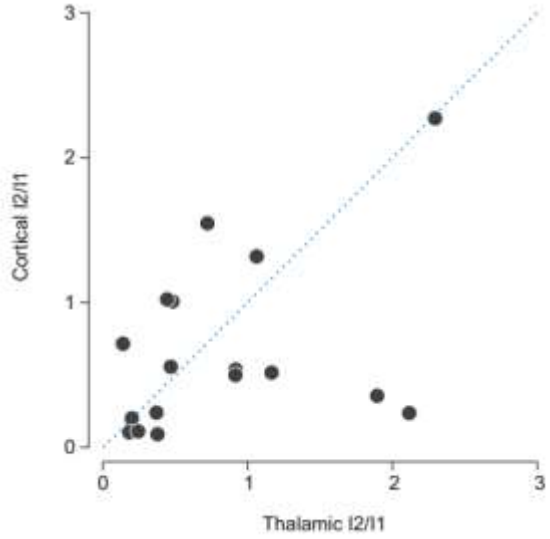

Figure 3.7: Comparison of degree of nonlinearity for thalamic and cortical responses.

Response nonlinearity is measured using nonlinearity index computed on voltage clamp responses (I2/I1) for both cortical and thalamic inputs.

Revisiting our model layout for different ways to obtain complex cells, we have convincing evidence that the direct thalamic inputs to complex cells can themselves be nonlinear. We also find that the thalamic F2/F1 do not differ significantly from cortical F2/F1 (F2/F1 thalamic vs cortical, two sample KS test, $p = 0.93$). This rules out the first scenario of the model which suggested that direct thalamic inputs were simple in nature and recurrence alone can cause nonlinearity.

Orientation tuning of aggregate thalamic inputs

Another approach to compare if the thalamic orientation tuned cells contribute to orientation selectivity of their cortical targets, is to compare the orientation selectivity of the mean and modulated components of the aggregate thalamic inputs (Lien and Scanziani, 2013). The modulated component of the response will be orientation tuned for an orientation tuned target cell. But the mean component will not be tuned if the individual cells contributing to the mean are themselves not orientation selective. Observing orientation selectivity in the mean response is therefore an indication of input by orientation selective LGN inputs (Lien and Scanziani, 2013). Across our sample population, we find the degree of orientation selectivity to be similar for the modulated thalamic response (Fig 3.8 A, B, median: 0.16, +/- s.d. 0.05, n = 13) and its mean component (Fig 3.8 C,D, median: 0.17, +/- s.d. 0.10, n = 13) and the two distributions were not different (n =13, two sample KS test, p = 0.22). They also depend on degree of linearity. This suggests that orientation selective LGN cells are indeed providing inputs to some of our recorded cells. The orientation tuning of the mean response may not however mean much for the cortical cell, if its orientation preference does not match the preference generated by the overall inputs.

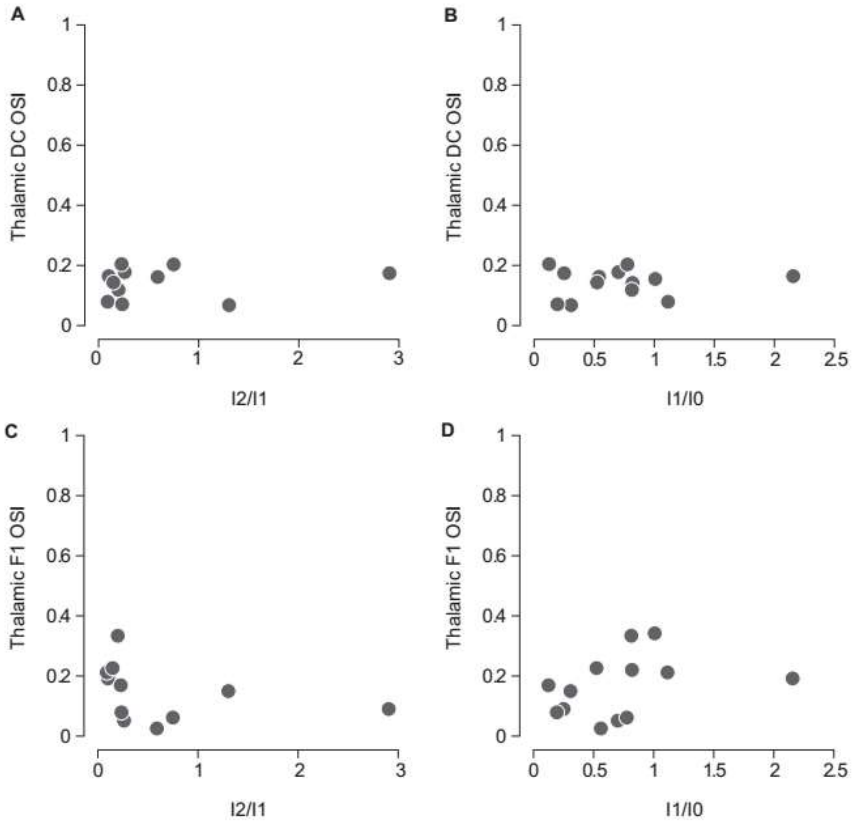

Figure 3.8: Population summary of orientation selectivity for thalamic responses and nonlinearity.

A, B: Orientation selectivity of mean component of the thalamic responses to drifting gratings as a function of nonlinearity index for responses to counterphase gratings in A and drifting gratings in B. C, D: Orientation selectivity of modulated component of the thalamic responses to drifting gratings as a function of nonlinearity index for responses to counterphase gratings in C and drifting gratings in D.

The orientation selectivity of inputs to mouse V1 neurons is weak (Tan et al., 2011), with a median OSI near 0.1. To assess whether the orientation tuned LGN cells contributed to receptive field of similar orientation preference, we

checked the match between orientation preference for the mean and modulated thalamic responses. We only compared these values for responses considered to be orientation tuned (OSI > 0.06). In our current data, we find a good match between the preferred orientation for F0 and F1 components (Fig 3.9, circular correlation = 0.88, n = 11). Despite the overall weak degree of selectivity, we observe in thalamic inputs, it is directly related to the orientation preference of V1 neurons.

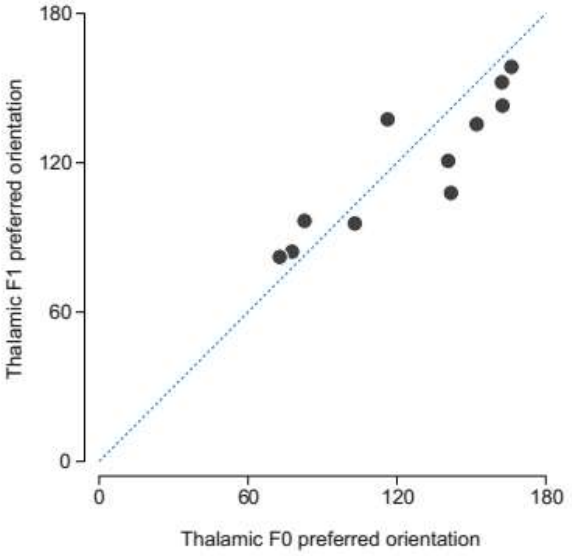

Figure 3.9: Comparison of preferred orientation of different response components of thalamic inputs.

Preferred orientation comparison between mean and modulated component of the thalamic responses to drifting gratings, plotted for cells with OSI > 0.06).

There are significant caveats to our observations. Our sample population contains a majority of neurons with f2/f1 ratios less than 1 (simple cells: 13/19).

Of the remaining 6 cells, 2 cells did not receive any thalamic input, and from 2 cells orientation selectivity was measured. We examined the mean component of the current inputs and found in both cases, nonlinear thalamic OSI is similar to the OSI measured when the cortex is intact. Nonetheless these data do suggest that the orientation selectivity of thalamic afferents may contribute to cortical orientation selectivity, as suggested by the third model. Further experiments will be required to dissect whether the second or third models are appropriate descriptions for the nonlinear thalamic input to complex cells in mouse V1.

DISCUSSION

Using a combination of in vivo intracellular recordings and optogenetic cortical silencing, we have searched for the rules that guide the circuitry underlying the diversity of spatial summation observed in orientation-selective neurons in mouse V1. We found evidence both for and against the hierarchical model proposed by Hubel and Wiesel to account for the emergence of orientation selective, spatially invariant responses in V1 (Hubel and Wiesel, 1962). Most simple cells receive monosynaptic input from the thalamus that imparts both orientation selectivity and phase specificity to these cells. In agreement with the hierarchical model, some complex cells, receive input only from recurrent inputs within V1. But we also uncovered find many discrepancies from the hierarchical model. Notably, we observed that a majority of complex cells receive monosynaptic thalamic input. Furthermore, the net thalamic input received by these cells also tends to be largely complex in nature, suggesting that cortical connectivity does not act to increase the complexity of V1 neuron receptive

fields. We have verified the nonlinear nature of the thalamic input using metric based on responses to drifting grating as well as responses to contrast reversing static gratings, which demonstrate significantly nonlinear input patterns. For a subset of these cells, we were also able to measure the orientation tuning of the aggregate thalamic input. We find that the aggregate input to all cells that receive monosynaptic thalamic input is orientation tuned. Even in those cells which exhibit highly nonlinear thalamic input, orientation selective input exists which matches the orientation preferences of the cortical inputs.

While we find significant discrepancies between the hierarchical model for the emergence of simple and complex cells described in carnivore and primate V1, these records demonstrate that the thalamic and recurrent inputs to cortical neurons are matched. The thalamic and cortical inputs to neurons exhibit the same orientation preferences. Thalamic and cortical inputs to simple cells modulate at the same temporal phase in simple cells. Furthermore, the degree of nonlinearity exhibited in thalamic inputs is matched to the degree of nonlinearity exhibited in the cortical inputs to the same neurons. It seems unlikely that these patterns of matched thalamic and cortical inputs could emerge from a circuit composed of random inputs (Hansel and van Vreeswijk, 2012).

The presence of nonlinear thalamic input to complex cells could act to disrupt orientation selectivity. If this nonlinear input reflects the summed activity of overlapping ON and OFF LGN neurons (Fig. 3.3 B), this input would be complex, but lack orientation selectivity. While this situation is formally possible,

we have demonstrated that the degree of nonlinearity of the input is independent from degree of orientation selectivity. Furthermore, we do not find differences in the overall orientation selectivity of neurons and the degree of response nonlinearity. One potential explanation for this independence of these parameters is the involvement of oriented LGN receptive fields projecting to cortical complex cells. More data are required to determine this outcome definitively. In summary, when cortical cells receive thalamic input, the degree of linearity of that input is maintained by the cortex.

Under the hierarchical connectivity model, there is a precise arrangement of connections between different cell types, that is able to explain the emergence of simple and complex cells within V1. In light of our current observations, we find a distinct circuit diagram in which the progression from simple, linear receptive fields to complex, nonlinear receptive fields is largely absent. Instead it is clear that between the thalamus and cortex the degree of selectivity is matched for many cells. Nonetheless there are hints of a progression between simple and complex receptive fields in the mouse visual pathway. Almost all simple cells received direct thalamic innervation, whereas a significant number of complex cells received purely cortical input.

The nonlinear thalamic input onto complex cells suggests that response nonlinearity may not be an emergent property in mouse V1. Our results, and those of previous studies, also indicate that orientation selectivity also emerges at stages prior to visual cortex. The basis for both the orientation tuning and

spatial nonlinearity of LGN cells seems to have a source in the retina (Baden et al., 2016; Suresh et al., 2016), though it could emerge from the convergence of multiple retinal ganglion cells onto thalamic relay cells. Whether the basis for this nonlinearity also relies on direct inheritance of nonlinear inputs from the retina or if it follows a Hubel and Wiesel connectivity, except in the LGN, or the convergence of orientation tuned inputs from the thalamus, remains to be tested.

Could our observed results be due to lack of complete inactivation of the cortex? It would be possible for long distance intracortical inputs to contribute to the responses of the recorded cells under the inactivation condition. Such an effect would lead to us overestimating the thalamic input and incorrectly assigning response features that are cortical to the thalamus. We think this unlikely, as our craniotomies during experiments were large and exposed the entire visual cortex. The LED illumination also covered the exposed cortical area and recording anywhere within the exposed area always resulted in cells ceasing to fire action potential when stimulated with LED. Furthermore, our estimates of thalamic inputs on cortical cells also match previously reported values (our data median = 0.31, compared to 30% input in (Lien and Scanziani, 2013, 2018)). Since these values also do not differ significantly between simple and complex cells, we think it is unlikely that the observed effects are due to insufficient inactivation of the cortex.

We have explored the flow of information from the visual thalamus to the cortex in order to find the rules that govern the emergence of spatial invariance

and orientation selectivity. We found that despite the disordered functional organization in the mouse V1, there is a strong alignment between thalamic and cortical inputs onto single V1 neurons. This alignment, in which cortical and thalamic inputs share orientation preference, degree of spatial invariance and phasic modulation, is not the organization that we had hypothesized that we would observe. Based on recordings in carnivores and primates we hypothesized that we would observe a hierarchy in which orientation selectivity initially emergence in thalamorecipient simple cells, followed by complex cells receiving cortical inputs that generate spatial invariance. The lack of this hierarchy suggests that the computations that the circuitry within mouse V1 are performing are distinct from those in carnivores and primates. The differences in computations may have their basis in the diversity of sensory signals that are provided in the mouse afferents. More than 30 retinal ganglion cell classes have been identified in the mouse, which carry distinct sensory information, including sensitivity to motion and orientation (Sanes and Masland, 2015). While some of those diverse signals undoubtedly remain in primates and carnivores, the retinas of both of these species are overwhelmingly dominated by two retinal ganglion cell classes, midget and parasol cells, which do not provide motion or orientation information. It is potentially the case that in the mouse signals for orientation selectivity and spatial invariance have already been extracted in the retina, whereas in carnivores and primates these computations are left to visual cortex. If this hypothesis were true, then the matching that we observe in terms of orientation and spatial invariance between the thalamic and cortical inputs, may

simply reflect a mechanism to maintain computations that have been performed at earlier stations.

Chapter 4: Binocular disparity selectivity weakened after monocular deprivation in mouse V1[3]

SUMMARY

Experiences during the critical period sculpt the circuitry within the neocortex, leading to changes in the functional responses of sensory neurons. Monocular deprivation (MD) during the visual critical period causes shifts in ocular preference, or dominance, towards the open eye in primary visual cortex (V1) and disrupts the normal development of acuity. In carnivores and primates, MD also disrupts the emergence of binocular disparity selectivity, a cue resulting from integrating ocular inputs. This disruption may be a result of the increase in neurons driven exclusively by the open eye that follows deprivation or a result of a mismatch in the convergence of ocular inputs. To distinguish between these possibilities, we measured the ocular dominance (OD) and disparity selectivity of neurons in mouse V1 following MD. Normal mouse V1 neurons are dominated by contralateral eye input and contralateral eye deprivation shifts mouse V1 neurons toward more balanced responses between the eyes. This shift towards binocularity, as assayed by OD, decreased binocularity disparity sensitivity. MD did not alter the initial maturation of binocularity, as disparity selectivity prior to the MD was indistinguishable from that of normal mature animals. Decreased disparity tuning was most pronounced in binocular and ipsilaterally-biased neurons, which are the populations that have undergone the largest shifts in OD. In concert with the decline in disparity selectivity we observed lower spatial

[3]Published in the Journal of Neuroscience (2017):
Binocular disparity selectivity weakened after monocular deprivation in mouse V1
Benjamin Scholl*, Jagruti J. Pattadkal*, and Nicholas J. Priebe
*Authors contributed equally

resolution for the ipsilateral eye following MD. These results suggest an emergence of novel synaptic inputs during MD that disrupt the representation of disparity selectivity.

INTRODUCTION

Experience-dependent plasticity during the developmental critical period (CP) shapes cortical circuit anatomy and functions (Katz and Crowley, 2002; Espinosa and Stryker, 2012). A prime example of CP plasticity is ocular dominance (OD) plasticity, where the OD of V1 neurons shifts towards the open eye following monocular deprivation (MD). In primates and carnivores, MD results both in a shift of neurons' responses to being dominated by the open eye, and a decline in binocular interactions necessary for three-dimensional representation of the world (Julesz, 1971). The decline in binocular disparity sensitivity is consistent with an increase in neuron monocularity, but whether these two are linked, however, is unclear.

Mouse V1 neuron responses, in contrast, are normally dominated by the contralateral eye. Contralateral MD shifts OD towards the ipsilateral eye, causing a paradoxical increase in binocularity (Gordon and Stryker, 1996). A conventional measure of binocularity, OD, is based on independent stimulation of each eye (Drager, 1975; Wagor et al., 1980; Hanover et al., 1999; Tagawa et al., 2005; Mrsic-Flogel et al., 2007; Hofer et al., 2009), but provides no information on binocular integration (LeVay and Voigt, 1988). Disparity selectivity, the sensitivity to spatial offsets between the two retinal images, requires the

integration of both retinal images (Hubel and Wiesel, 1962; Pettigrew et al., 1968; Joshua and Bishop, 1970; Ohzawa and Freeman, 1986; Longordo et al., 2013; Scholl et al., 2013a; Scholl et al., 2013b). Binocular disparity provides a cue for the depth of objects and modulates V1 neuron responses, which exhibit a variety of disparity preferences ranging from near to far (Poggio and Fischer, 1977; Ohzawa and Freeman, 1986; DeAngelis et al., 1995; Cumming and Parker, 1999).

We used this paradoxical increase in binocularity following MD to study how experience shapes binocular integration. We hypothesized that contralateral eye deprivation could affect disparity selectivity in mouse V1 neurons in three ways. Disparity selectivity could increase if the right and left eye signals are balanced by MD (Fig. 4.1A,B, left). Alternatively, disparity selectivity could decrease if novel circuitry disrupts the precise receptive field alignment between the eyes (Fig. 4.1B, right). Finally, disparity selectivity could remain the same if compensatory mechanisms counteract these other effects.

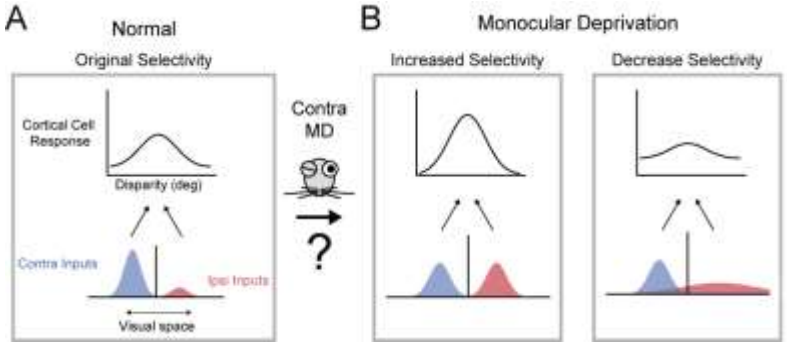

Figure 4.1: Potential changes to disparity selectivity following monocular deprivation.

(a) Normal adult mouse visual cortical neurons are contralaterally biased by monocular stimuli but can be sensitive to binocular disparity by receiving weak ipsilateral inputs. Disparity selectivity formed from the convergence of distributions of contralateral and ipsilateral inputs representing distinct locations in visual space. (b) Monocular deprivation of the dominant eye leads to a shift in ocular preference such that neurons are more binocular by monocular stimulation. Increased binocularity could increase disparity selectivity by the enhancement of excitatory input from the weak eye (left). Disparity selectivity could be decreased if the ipsilateral input no longer provides the spatial signal necessary for generating disparity selectivity (right). (Fig. 4.1. continued).

We assessed how MD during the CP alters binocular integration using in vivo two-photon calcium imaging (Stosiek et al., 2003; Kerr et al., 2005; Ohki et al., 2005; Garaschuk et al., 2006; Mrsic-Flogel et al., 2007; Golshani and Portera-Cailliau, 2008; Scholl et al., 2015) from layer 2/3 neurons in the binocular zone of mouse V1. We measured OD and binocular disparity selectivity in normal pre-CP animals, post-CP animals, and animals following MD during the CP. In deprived animals, disparity selectivity was decreased compared to normal post-CP animals. Normal binocular integration exists before the MD was performed, as disparity selectivity and OD were similar between pre- and post- CP animals. The decline in disparity selectivity was predominately found in neurons receiving substantial input from the non-deprived eye. In concert with this decline we found evidence for a disruption in the ipsilateral eye receptive field following MD. Together, our data suggest that eye occlusion reshapes synaptic inputs without preserving functionality required for stereoscopic disparity sensitivity.

METHODS

Physiology

Procedures for two-photon imaging and physiology were based on those previously described (Scholl et al., 2013a; Scholl et al., 2015). Experiments were conducted using normal animals (n = 14, P25 - P60) or animals with the contralateral eye deprived during the critical period (n = 7). Both male and female animals were used. 4-day monocular deprivation was initiated between P28 and P30 (Gordon and Stryker, 1996; Hanover et al., 1999; Tagawa et al., 2005). Mice were anesthetized with intraperitoneal injections of 1000 mg/kg urethane and 10 mg/kg chlorprothixene. Brain edema was prevented by intraperitoneal injection of 10 mg/kg dexamethasone. Animals were warmed with a thermostatically controlled heat lamp to maintain body temperature at 37oC. A tracheotomy was performed. The head was placed in a mouse adaptor (Stoelting) and a craniotomy and duratomy were performed over visual cortex. Eyes were kept moist with a thin layer of silicone oil. Primary visual cortex and binocular zone were located and mapped by multi-unit extracellular recordings with tungsten electrodes (1 mΩ, Micro Probes). The V1/V2 boundary was identified by the characteristic gradient in receptive locations (Drager and Hubel, 1975; Metin et al., 1988) Eye drift under urethane anesthesia is typically small and results in a change in eye position of less than 2 degrees per hour (Sarnaik et al., 2014).

Dye Loading and In vivo Two-Photon Microscopy

Bulk loading of a calcium sensitive dye under continuous visual guidance followed previous protocols (Stosiek et al., 2003; Kerr et al., 2005; Ohki et al.,

2005; Garaschuk et al., 2006; Mrsic-Flogel et al., 2007; Golshani and Portera-Cailliau, 2008; Scholl et al., 2015) in the V1 binocular zone. Dye solution contained 0.8 mM Oregon Green 488 BAPTA-1 AM (OGB-1 AM, Invitrogen) dissolved in DMSO (Sigma-Aldrich) with 20% pluronic acid (Sigma-Aldrich) and mixed in a salt solution (150 mM NaCl, 2.5 mM KCl, 10 mM HEPES, pH 7.4, all Sigma-Aldrich). Either 40-80 µM Alexa Fluor 594 (Invitrogen) or 125 µM Sulforhodamine 101 (Sigma-Aldrich) was also included for visualization during and immediately after loading. Patch pipettes (tip diameter 2-5 µm, King Precision Glass) containing this solution were inserted into the cortex to a depth of 250-400 µm below the surface with 1.5% agarose (in saline) placed on top the brain. The solution was carefully pressure injected (100-350 mbar) over 10-15 minutes to cause the least amount of tissue damage. OGB-1-AM is only weakly fluorescent before being internalized, so the amount of dye injected was inferred through the red dye. To ensure full loading we waited 1 hr before adding a glass coverslip for imaging. Metal springs were fastened on the attached head plate to place pressure on the glass coverslip and reduce brain pulsations. Fluctuations in calcium fluorescence were collected with a custom-built two-photon resonant mirror scanning microscope (Stosiek et al., 2003; Golshani and Portera-Cailliau, 2008; Scholl et al., 2015) and a mode-locked (925 nm) Chameleon Ultra Ti: Sapphire laser (Coherent). Excitation light was focused by a 40x water objective (0.8 numerical aperture, Nikon). Images were obtained with custom software (Labview, National Instruments). A square region of cortex 300 µm wide was imaged at 256x455 pixels. In all experiments, multiple focal planes, separated by 20-25 µm, were used to collect data, starting around 150 µm below the cortical

surface. Before each experiment neuron drift was measured over a 2-3 min period. If drift occurred, then the glass coverslip and agarose were readjusted to stabilize the brain during stimulus protocol (7-10 minutes each focal plane).

Stimuli

Visual stimuli were generated by a Macintosh computer (Apple) using the Psychophysics Toolbox (Brainard, 1997; Pelli, 1997) for Matlab (Mathworks). Gratings were presented dichoptically using Sony video monitors (GDM-F520) placed 25 cm from the animal's eyes. The video monitors had a non-interlaced refresh rate of 100Hz and a spatial resolution of 1024x768 pixels, which subtended 40x30 cm (58x46 deg). The video monitors had a mean luminance of 40 cd/cm2. Square-wave drifting gratings (38 deg diameter, 0.02-0.04 spatial frequency, 100% contrast, 1-4 Hz temporal frequency) were presented for 2-3 sec. Each stimulus was followed by a 3 sec blank (mean luminance) period. Spontaneous activity was measured during blank (mean luminance) periods interleaved with binocular and monocular drifting grating stimuli, all presented in a pseudorandom sequence. Binocular phase differences (disparities) ranged 0-315 deg. For a subset of experiments, we also measured preferred orientation (grating orientation ranged 0-315 deg) and spatial frequency sensitivity using gratings (grating orientation 90 deg) of spatial frequencies that varied between 0.01 and 0.16 cycles/degree. During imaging sessions, each stimulation protocol was repeated 7-10 times at each focal plane. The microscope objective and photomultiplier tubes were shielded from stray light and the video monitors.

Two-photon Calcium Imaging Analysis

Images were analyzed with custom Matlab software (Mathworks). Cells were identified by hand from structure images based on size, shape, and brightness. Cell masks were generated automatically following previous methods (Nauhaus et al., 2012). Glia were easily avoided due to their different morphology from both OGB-1 AM filled neurons. Time courses for individual neurons were extracted by summing pixel intensity values within cell masks in each frame. Responses (F_t) to each stimulus presentation were normalized by the response to the gray screen (F_o) immediately before the stimulus came on:

$$\Delta F/F = (F_t - F_o)/F_o$$

For each stimulus, the mean change in fluorescence ($\Delta F/F$) was calculated in a 0.5 sec window of the response, identified by averaging responses to all stimuli and detecting the global peak. Visually responsive cells were identified if at least one monocular and one binocular stimulus response had:

$$(\mu_{Stimulus} - \mu_{Spontaneous})/(SE_{Stimulus} + SE_{Spontaneous}) > 1.$$

$\mu_{Stimulus}$ refers to the mean stimulus evoked response, $\mu_{Spontaneous}$ refers to the mean spontaneous activity, $SE_{Stimulus}$ is the stimulus evoked response standard error, and $SE_{Spontaneous}$ spontaneous activity standard error. Additionally, identified responses to each monocular and binocular stimulus were required have distinct different trial-to-trial fluorescence time courses, so as to not be scaled versions of neuropil activity.

Mean changes in fluorescence from visually responsive neurons were used to generate tuning curves for binocular disparity. Tuning curves in figures

4.2 and 4.3 were fit with a cosine-wave function. To measure ocular dominance, we used a standard metric (Cang et al., 2005; Priebe, 2008):

$$ODI = (R_{ipsi} - R_{contra})/(R_{ipsi} + R_{contra})$$

Here R_{contra} and R_{ipsi} represent calcium responses from monocular stimulation of the contralateral and ipsilateral eyes, respectively. Disparity selectivity was quantified using a normalized vector strength (Scholl et al., 2013a; Scholl et al., 2013b):

$$DSI = \frac{\sqrt{(\sum_{\varphi} R_{\varphi} \sin(\varphi))^2 + (\sum_{\varphi} R_{\varphi} \cos(\varphi))^2}}{\sum_{\varphi} R_{\varphi}}$$

Here R is a calcium response to the particular binocular disparity (φ).

Orientation preference was characterized using a double Gaussian curve (Carandini and Ferster, 2000). Both Gaussian curves had the same variance (σ2) but different amplitudes (α and β). The second Gaussian curve was constrained to be 180o phase shifted from the preferred orientation (θ_{pref}).

$$R(\theta) = \alpha e^{-(\theta - \theta_{pref})^2/(2\sigma^2)} + \beta e^{-(\theta - \theta_{pref} + \pi)^2/(2\sigma^2)} + k$$

Here R(θ) is the peak calcium response at the particular orientation used (θ), k is the baseline spontaneous activity. The preferred orientation was estimated from this fitted equation. The orientation selectivity index was computed using the following equation: (Ringach et al. 2002; Tan et al. 2011):

$$OSI = \frac{\sqrt{(\sum R(\theta) \sin(2\theta))^2 + (\sum R(\theta) \cos(2\theta))^2}}{\sum R(\theta)}$$

Spatial frequency tuning responses were fitted using a single Gaussian function (DeAngelis et al., 1993; Van den Bergh et al., 2010):

$$R(\theta) = \alpha e^{-(\theta - \theta_{pref})^2/(2\sigma^2)} + k$$

Here R(θ) is the peak calcium response at the particular spatial frequency (θ), α is the amplitude of the Gaussian, θpref is the preferred spatial frequency, σ2 is the variance of the Gaussian used, k is the baseline. The function is Gaussian along a linear axis. The preferred spatial frequency was estimated from the fitted equation. We also measured spatial resolution, which was defined as the highest spatial frequency at which the fitted tuning curve reached baseline level (Van den Bergh et al., 2010).

Binocular Disparity Model

We modeled the thalamocortical input and the first stage of binocular integration within visual cortex. Thalamic inputs responses to drifting gratings were modeled as half-wave rectified sine waves (Scholl et al., 2013a). Each thalamic input responded in a phase sensitive manner to the drifting grating. Individual thalamic relay cells had distinct phase selective responses due to slight offsets in their spatial receptive field (Reid and Alonso, 1995). In the normal condition, the Gaussian distribution of phases was characterized by a standard deviation of 14 degrees. The total contralateral input (R_c) and ipsilateral input (R_i) to a cortical neuron was thus modeled as:

$$R_i = \sum \lfloor \sin(\omega t + \delta_i) \rfloor_+$$

$$R_c = \sum \lfloor \sin(\omega t + \delta_c) \rfloor_+$$

where R_i and R_c reflect the differences between individual relays cells due to offsets in receptive fields. Input phases from each eye were drawn for separate distributions, thus the mean phase difference between these

distributions defined the neuron's preferred disparity or interocular phase difference. To change the diversity of spatial positions that converge onto a cortical cell, the standard deviation of the either □i and □c was adjusted. Monocular inputs were generated by summing all inputs from each eye and normalizing the amplitude by the total number of inputs. Binocular inputs were generated by shifting the phase of one monocular aggregate input (simulating the systematic change in interocular phase difference between two gratings) and summing monocular aggregates. Thalamic inputs were then passed through a threshold to simulate spiking output responses. Peak (DC + F1) amplitudes of binocular responses were then used to compute the DSI. Peak monocular input amplitude was used to compute the ODI. To simulate contralateral eye deprivation, the number of contralateral eye inputs were decreased in conjunction with an equivalent increase in the number of ipsilateral inputs. Two MD scenarios were examined: (1) new ipsilateral eye input phase preferences match the old ipsilateral inputs or (2) new ipsilateral eye input phase preferences increase the variance of □i. In scenario (1), new input phase preferences were drawn from the same ipsilateral eye normal distribution. In scenario (2), the distribution variance was increased. Note that while in scenario 2 we model the effects of MD as by changing the ipsilateral receptive field, receptive field changes could occur in the contralateral input and would also impact disparity selectivity. Disparity selectivity relies on an alignment between ipsilateral and contralateral inputs that can be degraded either by changes in the contralateral, ipsilateral, or both receptive fields.

All animal procedures were approved by The University of Texas at Austin Institutional Animal Care and Use Committee.

RESULTS

We used in vivo two-photon calcium imaging to measure the ocular dominance and binocular disparity tuning of neurons in V1 of anesthetized normal and monocularly deprived (MD) mice (see Methods). Deprivation of the contralateral eye was initiated during the critical period (CP) (P28-P30) and lasted for 4 days (Gordon and Stryker, 1996; Hanover et al., 1999; Tagawa et al., 2005). In each experiment the binocular zone of V1 was identified from extracellular recordings, receptive fields were carefully mapped in a targeted region within the central 30 degrees of the visual field, and a mirror was placed in front of the contralateral eye to allow for presentation of a dichoptic stimulus (Scholl et al., 2013a).

Potential effects of monocular deprivation on binocular integration

Cortical neurons in the binocular zone of mouse V1 are normally dominated by input from the contralateral eye. Despite the imbalance in contra- and ipsilateral eye inputs, prominent disparity selectivity exists in these neurons (Fig. 4.1A). In this illustration, the receptive field profiles of each eyes are spatially disparate. This spatial disparity of the receptive fields between the two eyes causes certain stimulus phase differences to evoked greater response than others. By probing a range of stimulus phase differences, it is possible to measure the sensitivity of cortical cell for binocular disparity (Ohzawa and Freeman, 1986).

Contralateral eye deprivation during the CP in mouse V1 produces a shift in the ocular dominance towards more equivalent inputs between the two eyes (Gordon and Stryker, 1996; Hanover et al., 1999; Tagawa et al., 2005). To illustrate two possible outcomes from MD we show loss of contralateral input in conjunction with the addition of new ipsilateral input (Fig. 4.1B). In the first case, binocular disparity selectivity could be increased if the new ipsilateral synaptic inputs have the same receptive field locations as that of pre-existing ones (Fig. 4.1B, left). This is because the preferred interocular phase difference would be preserved and synapses of equivalent strength from each eye will generate larger response modulation with binocular disparity (Scholl et al., 2013a; Scholl et al., 2013b). Alternatively, contralateral deprivation might cause a decrease in disparity selectivity if new ipsilateral inputs alter the spatial receptive field (Fig. 4.1B, right). While we diagram these changes as impacting the ipsilateral receptive field, similarly disruptive changes could occur in the contralateral receptive field during deprivation. Changes in the receptive field brought on by new inputs from either eye could degrade the precise alignment of contra and ipsilateral inputs, leading to decreased disparity sensitivity.

Binocular response properties in normal and deprived animals

To measure monocular responses and binocular disparity selectivity we pseudorandomly presented dichoptic drifting vertical gratings to each eye alone or simultaneously while recording changes in calcium fluorescence. By varying the interocular phase difference of the drifting gratings, we probed eight binocular disparities (0-315 deg). During each experiment we imaged multiple focal planes

below the pial surface. A rotatable objective was used to position the cortical surface normal to imaging plane. Cells were chosen by hand from an OGB-1 AM structure image (Fig. 4.2A-B, right) and an automated algorithm created a mask for denoting pixels to average in each frame (Scholl et al., 2015). Across normal animals used (n = 10, P35-P60) we identified a total of 4,924 neurons, of which 1,191 neurons were visually responsive (see Methods for criterion) for vertical monocular stimuli (24%) and 2,505 neurons were visually responsive for binocular stimuli (51%). Across MD animals used (n = 7, P33-P35) we identified a total of 3,463 neurons, of which 932 neurons were visually responsive for monocular stimuli (27%) and 1,853 neurons were visually responsive for binocular stimuli (54%). To probe binocular disparity, we employed vertically oriented gratings at a single spatial frequency. Mouse V1 neurons exhibit a ‘salt and pepper’ pattern of orientation preferences and a wide range of spatial frequency selectivity (Ohki et al., 2005; Niell and Stryker, 2008), so the vertically oriented gratings may not be effective at stimulating all visually responsive neurons.

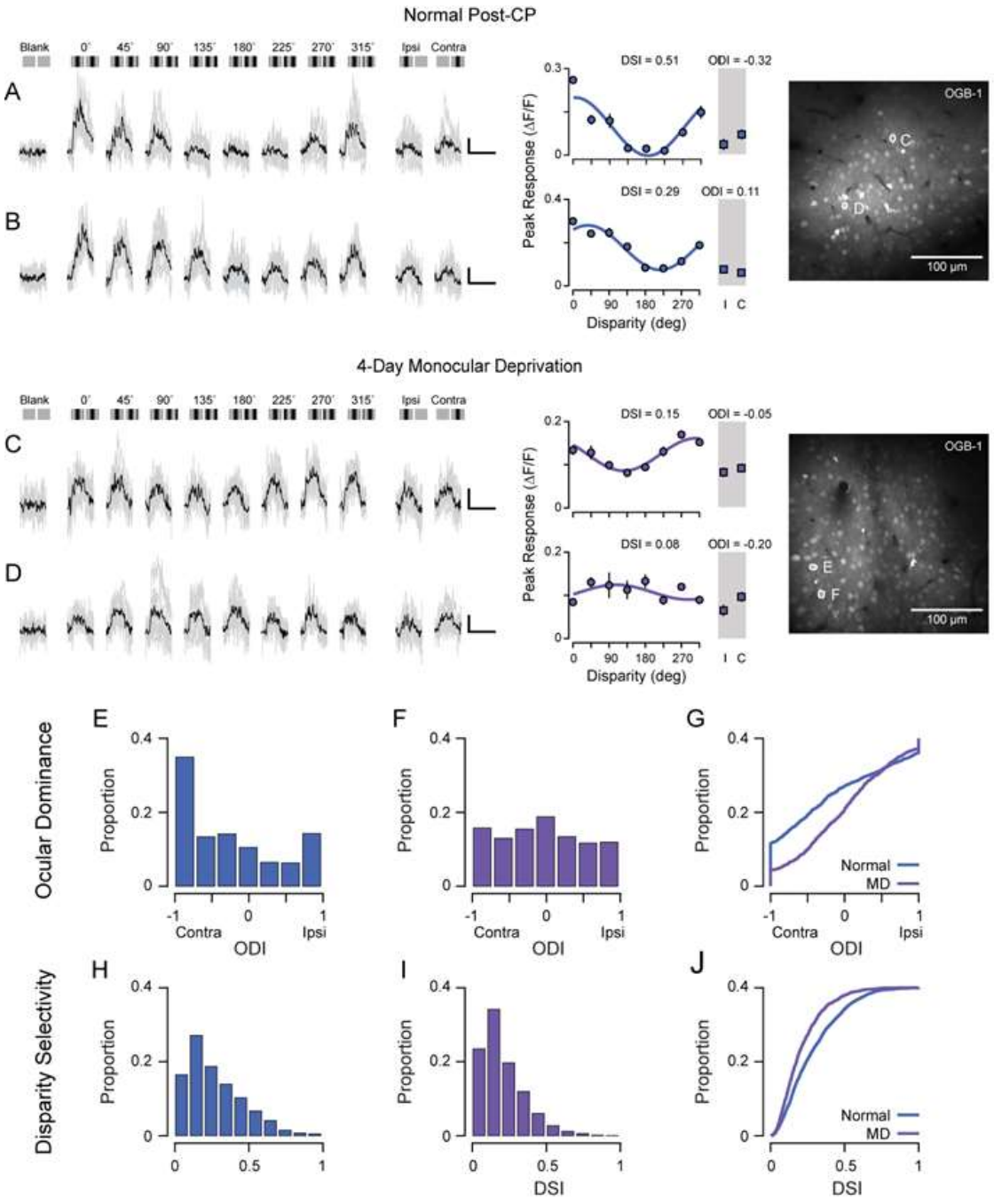

Figure 4.2: Two-photon imaging of binocular disparity selectivity in neurons from mouse V1 binocular zone

(a - d) Example of calcium responses in a binocular neuron evoked by a range of binocular disparities (0 - 315 deg), monocular stimulation of each eye, and a mean luminance screen. Individual traces shown in gray and trial-average mean shown in black. Illustration of each stimulus shown above response traces. Scale bar indicates 10% change in fluorescence (∆F/F) and 2 sec duration. Mean and standard error of peak ∆F/F shown in a tuning curve. Two-photon images (right) show fluorescence from OGB-1 AM dye. Drifting gratings used to measure these responses had a spatial frequency of 0.02 cycles per deg. (a-b) Example neurons from a normal animal with different ocular preferences, but both selective to binocular disparity. (c-d) Example neurons from an animal with 4-day monocular deprivation (MD) during the critical period. (e) Population ocular dominance (OD) distribution from normal animals. (f) Population OD distribution from animals with 4-day MD. (g) Cumulative OD distributions from normal and MD animals showing the shift towards binocularity in the MD animals. (h) Population distribution of disparity selectivity index for cells from normal animals (i) Population distribution of disparity selectivity index for cells from animals with MD. (j) Cumulative distributions for disparity selectivity index from normal and MD animals showing the shift towards lowed disparity selectivity following MD. (Fig. 4.2. continued).

Fluorescence fluctuations from cells in mouse V1 were strongly modulated by binocular disparities, compared to stimulation of either eye alone or the blank (mean luminance) period, similarly to previous reports of spiking activity (Scholl et al., 2013a) and two-photon calcium imaging in cat (Kara and Boyd, 2009) and mouse V1 (Scholl et al., 2015). In an example neuron (Fig. 4.2A), monocular stimulation of either eye evoked roughly equivalent changes in fluorescence (5-10% ∆F/F), while the preferred disparity (0o phase difference) evoked even larger fluorescence changes (~30% ∆F/F) and the null disparity (180o phase difference) evoked little change (~5% ∆F/F). Plotting stimulus-averaged peak calcium responses showed response modulation by disparity and binocular responses that were as strong or stronger than responses to either eye alone (Fig. 4.2A, see tuning curve). From these neural responses we computed two

metrics: an ocular dominance index (ODI, see Methods) to compare monocular responses from each eye and a disparity selectivity index (DSI, see Methods) to quantify response selectivity to binocular phase differences. In this example (Fig. 4.2A), these metrics depicted a binocular, but contralaterally-biased neuron with strong disparity selectivity (ODI = -0.32, DSI = 0.51). Ipsilaterally biased neurons also exhibit strong disparity selectivity (ODI = 0.11, DSI = 0.29, Fig. 4.2B).

Across all neurons with visually evoked responses to monocular stimuli we found a shift in OD between normal and deprived animals. As reported previously from spiking (Gordon and Stryker, 1996; Hanover et al., 1999; Tagawa et al., 2005) and calcium responses (Mrsic-Flogel et al., 2007; Kameyama et al., 2010), the contralateral bias in normal mice (Fig. 4.2E) shifted towards more equivalent monocular responses and a more uniform distribution of ocular dominance (Fig. 4.2F). Since ODI is a symmetric index, to quantify the difference in these distributions we computed the absolute value of ODI, such that a value of 0 indicates binocular responses and a value of 1 indicated perfectly monocular responses. Neurons from normal animals were more monocular than those from MD animals (Normal: mean |ODI| = 0.64 ± 0.34 s.d., n = 1191; MD: mean |ODI| = 0.49 ± 0.33 s.d., n = 932; $p < 0.001$, Mann-Whitney test, Fig. 4.2G).

We next investigated how increases in binocularity following MD affected disparity selectivity. Surprisingly, we found a decrease in DSI in deprived animals compared to those raised normally (Fig. 4.2H-I). With normal development, neurons exhibited modest disparity selectivity (median DSI = 0.23, mean DSI =

0.28 ± 0.19 s.d., n = 2505), whereas neurons showed a significant reduction in disparity selectivity following MD (median DSI = 0.17, mean DSI = 0.21 ± 0.14 s.d., n = 1853; $p < 0.001$, Student's two-tailed t-test, Fig. 4.2J). This loss of disparity selectivity demonstrates a divergence in how MD affects ocular dominance and disparity selectivity, suggesting that a rearrangement of inputs occurs that disrupts the match of receptive fields necessary for disparity selectivity.

Although we observe a significant decrease in DSI for deprived animals, we wondered whether this decrease is related to differences in peak binocular responses across our population of individual cells (5 – 40% $\Delta F/F$). We therefore compared the degree of disparity selectivity in normal and monocularly deprived animals for groups of cells with similar amplitude binocular responses. When comparing only cells with small (< 10%), medium (10% to 20%), or large (> 20%) amplitude peak binocular responses, the difference in disparity selectivity between deprived and normal animals was consistent ($p < 0.001$, Mann-Whitney). We did find that DSI was correlated with peak binocular responses (Normal: amplitude < 10% median DSI = 0.20, amplitude > 20% median DSI = 0.43; MD: amplitude < 10% median DSI = 0.15, amplitude > 20% median DSI = 0.37). This relationship was also monotonic, suggesting that saturation of the calcium indicator was unlikely to influence our measurements of DSI. Another potential issue is that we employed vertical gratings, while the orientation preference of individual cells varies substantially. In a subset of experiments, we separated neurons into those preferring vertical and horizontal gratings and did

not find a difference in DSI (preferred orientation = 90o ± 45o s.d., n = 27, median DSI = 0.28; preferred orientation = 0o ± 45o s.d., n = 70, median DSI = 0.26; p = 0.35, Mann-Whitney test).

Binocular response properties in young animals

One potential explanation for the reduction in disparity selectivity by MD is that disparity selectivity emerges over the period in which the deprivation occurred, and we have disrupted this development. To address this possibility, we measured binocular response properties of V1 neurons in mice during the epoch immediately before we performed MD (P25-P27). We denote these animals Pre-CP, even though it has been shown that mouse V1 neurons are plastic at this age.

Across all animals used (n = 4, P25-P27) we identified a total of 4,137 neurons, of which 1197 neurons were visually responsive (see Methods for criterion) for monocular stimuli (29%) and 1685 neurons were visually responsive for binocular stimuli (41%). As in normal animals, neurons responding to stimulation of both eyes equally (ODI = -0.03, Fig. 4.3A) as well as those driven predominately by one eye (ODI = -0.50, Fig. 4.3B), were strongly modulated by binocular disparities (DSI = 0.36 and DSI = 0.41, respectively). The distribution of ODI and absolute value of the ODI in pre-CP neurons was identical to that of normal animals (Pre-CP: median |ODI| = 0.67, mean |ODI| = 0.64 ± 0.32 s.d., n = 1197; Post-CP: median |ODI| = 0.70, mean |ODI| = 0.64 ± 0.34 s.d., n = 1191; p = 0.001, Mann-Whitney test; Fig. 4.3C). Importantly, disparity selectivity, which reflects the underlying binocular synaptic integration, between pre-CP and

normal animals was similar, although pre-CP neurons showed slightly greater selectivity (Pre-CP: median DSI = 0.26, mean DSI = 0.29 ± 0.18 s.d., n = 1685; Post-CP: median DSI = 0.23, mean DSI = 0.28 ± 0.19 s.d., n = 2505; $p < 0.01$, Mann-Whitney test; Fig. 4.3D). These data suggest that disparity selectivity has formed prior to the monocular deprivation, and that the deprivation disrupted

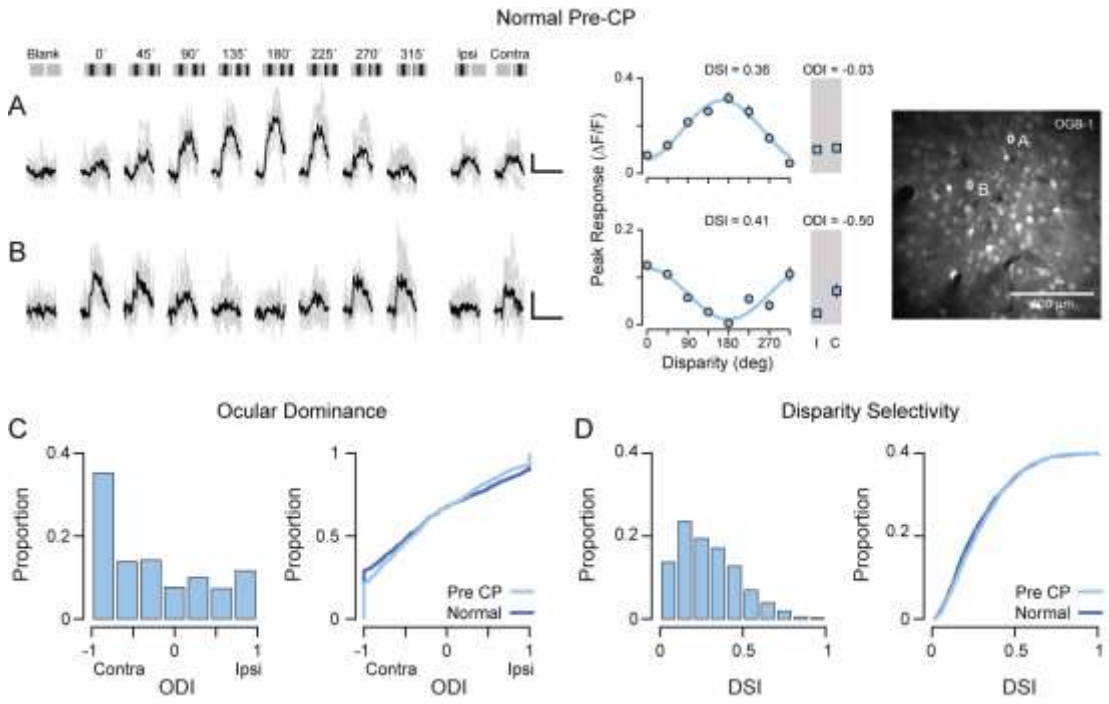

normal binocular integration.

Figure 4.3: Disparity selectivity formed prior to the critical period

(a-b) Example tuning responses from neurons in an animal imaged prior to the critical period. Both binocular and monocular neurons, as defined by ocular dominance (OD) are sensitive for binocular disparity. Drifting gratings used to measure these responses had a spatial frequency of 0.02 cycles per deg. (c) OD distribution from animals prior to the critical period (left). Cumulative distributions from between pre- and post- critical period animals show similar OD (right). (d) Distribution for disparity selectivity index from animals prior to the critical period

(left). Cumulative distributions from between pre- and post- critical period animals show identical disparity selectivity (right). (Fig. 4.3. continued).

Specificity of disparity selectivity loss in deprived animals

Despite a large shift in ocular dominance and disparity selectivity following MD, the impact of MD on OD and disparity selectivity was variable. For example, some neurons following MD maintain a strong preference for the contralateral eye (Fig. 4.2F) while others maintain a degree of disparity selectivity like that found in normal animals (Fig. 4.2I). This maintenance of selectivity diversity may result from differential impacts of MD. If so, then neurons with maintained OD preference should exhibit little change in disparity selectivity. Likewise, neurons receiving more input from the ipsilateral (non-deprived) eye should exhibit greater reductions in disparity selectivity. Thus, we grouped the neurons based on OD and compared their disparity selectivity (Normal: n = 1012, Deprived: 838). Neurons maintaining preference for contralateral eye input following MD have little change in disparity selectivity (Fig. 4.4, unfilled circles, OD < -0.6: $p = 0.14$, Mann-Whitney test). All other OD groups showed significant reductions in disparity selectivity (Fig. 4.4, filled circles, $p < 0.01$, Mann-Whitney test). These results indicate that the circuit changes following MD are responsible for the reduction in disparity selectivity. We also examined the relationship between OD and disparity selectivity in pre-CP animals (n = 910 cells), finding similar degrees of disparity selectivity as in normal animals for neurons receiving contralateral input (OD < 0: $p = 0.12$, Mann-Whitney test), but greater disparity selectivity for neurons receiving ipsilateral input (OD > 0: $p < 0.01$, Mann-Whitney test). In both groups we noticed that monocular neurons receiving ipsilateral input had greater

disparity selectivity than those receiving contralateral input (Pre-CP: OD < -0.6: median DSI = 0.20, OD > 0.6: median DSI = 0.41, $p < 0.001$, Mann-Whitney test; Normal: OD < -0.6: median DSI = 0.24, OD > 0.6: median DSI = 0.34, $p < 0.001$, Mann-Whitney test). This is surprising given the strong contralateral bias typically found in mouse V1 (Fig. 4.2E, 4.3C), but suggests that the ipsilateral eye input prevails in controlling the degree of disparity selectivity.

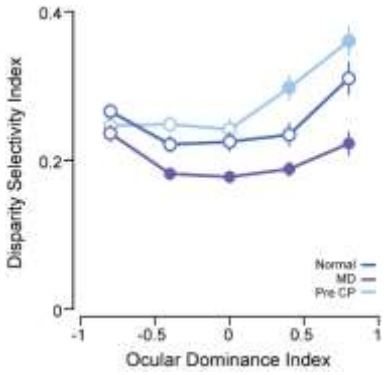

Figure 4.4: Decreased disparity selectivity found in binocular and ipsilaterally-dominant neurons.

Disparity selectivity for normal pre-critical period (light blue), normal post-critical period (dark blue), and deprived animals (purple) are shown for different ocular dominance groups. Each point represents mean and standard error. Filled circles represent significantly different values as compared to normal post-critical period animals.

The decline in disparity selectivity following MD may be the consequence of a change in overall activation of neurons by binocular stimulation or by a change in the degree in which cells are modulated by binocular stimulation. To address this, we compared fluorescence response amplitudes of neurons to binocular stimulation in normal animals, deprived animals and pre-CP animals. We grouped neurons by ocular dominance and examined only disparity selective

neurons (DSI > 0.1) (Fig. 4.5). Except for ipsilateral-biased neurons (0.2 < OD < 0.6), there were no differences in response amplitude to the preferred binocular stimulus between normal and deprived animals ($p > 0.15$, Mann-Whitney test). We did find that pre-CP animals exhibited weaker preferred disparity responses, compared to post-CP and deprived animals ($p < 0.02$, Mann-Whitney for all groups except ipsilaterally-biased). This was also reflected in the average preferred binocular disparity response amplitude across all cells (Normal post-CP = 0.13 ± 0.08; MD = 0.12 ± 0.06; Normal Pre-CP = 0.10 ± 0.05; mean ± s.d. ΔF/F). An identical trend was found when comparing the mean binocular response across all cells without excluding unselective cells (Normal post-CP = 0.07 ± 0.04; MD = 0.07 ± 0.03; pre-CP = 0.5 ± 0.03; mean ± s.d. ΔF/F). These results suggest that the loss of disparity selectivity following MD cannot be attributed to a strong change in monocular or binocular response amplitudes, particularly because neurons receiving ipsilateral input are shown to have equivalent response amplitudes to binocular stimulation.

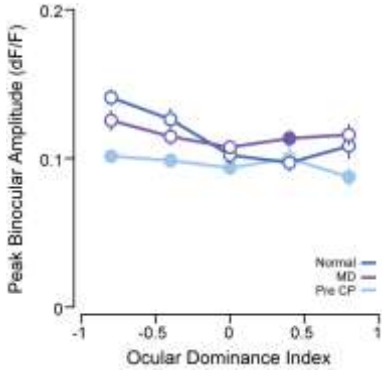

Figure 4.5: Response amplitude for preferred binocular disparity.

Magnitude of calcium responses to the preferred binocular disparity for cells from normal pre-critical period (light blue), normal post-critical period (dark blue), and deprived animals (purple), shown for different ocular dominance groups. Each point represents mean and standard error. Filled circles represent significantly different values as comparted to normal post-critical period animals. (Fig. 4.5. continued).

Our working model postulates that changes in the receptive field properties of ipsilateral inputs could underlie the loss of binocular integration following MD. One possibility is that the ipsilateral receptive fields lose spatial acuity, potentially through aberrant synaptic plasticity during MD. We tested this prediction by measuring the spatial frequency selectivity of individual neurons in normal and deprived animals. Using a vertical drifting grating, we first analyzed the responses of individual neurons to characterize their SF tuning (Fig. 4.6). Individual neurons responding to ipsilateral visual stimulation in normal animals had a broad range of spatial frequency preferences that extended to high spatial frequencies for the mouse visual system (Niell and Stryker, 2008), while ipsilateral neurons in animals with MD often responded to the lower spatial frequencies used (Fig. 4.6A). These examples followed the global trend across our population of cells, where we found a decrease in spatial resolution (high spatial frequency cutoff) caused by MD for cells responding to ipsilateral stimulation (Normal: mean resolution = 0.07 ± 0.05 s.d. cycles per degree, n = 70; MD: mean resolution = 0.05 ± 0.02 s.d. cycles per degree, n = 103; $p < 0.01$, Mann-Whitney test; Fig. 4.6B, right). In contrast, we found little difference for contralaterally dominated neurons (Normal: mean resolution = 0.10 ± 0.04 s.d. cycles per degree, n = 146; MD: mean resolution = 0.09 ± 0.04 s.d. cycles per degree, $p = 0.09$, n = 112; Fig. 4.6B, left). These trends were also observed in the spatial frequency preferences of neurons following MD but were not

significant (Fig. 4.6C). The geometric mean peak spatial frequency for the ipsilateral eye was 0.023 ± 0.01 (n = 103), lower than that found in normal animals (0.03 ± 0.03). These data indicate that ipsilateral receptive fields have been altered by monocular deprivation, shifting toward lower spatial resolution for the non-deprived eye. Such a mismatch in receptive field parameters is consistent with the reduction in disparity selectivity we uncovered following MD.

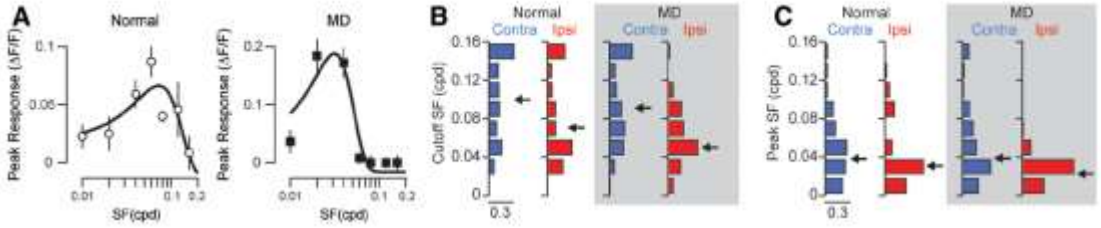

Figure 4.6: Loss of spatial acuity in the non-deprived eye

(a) Spatial frequency tuning of example neurons from normal (left, open circles) and deprived (right, filled squares) animals. Responses shown here are for ipsilateral eye visual stimulation with a vertical grating. Mean and standard error of peak ΔF/F along with fits for spatial frequency selectivity (see Methods). (b) The spatial resolution for the contralateral (blue) and ipsilateral (red) eye stimulation. Histograms of the spatial resolution are shown for both normal animals as well as animals following MD (gray background). (c) The peak spatial frequency for the contralateral (blue) and ipsilateral (red) eye stimulation. Histograms of the preferred spatial frequency are shown for both normal animals as well as animals following MD (gray background).

DISCUSSION

Experience-dependent plasticity during the critical period guides maturation of sensory cortical circuits, both in anatomical and functional response properties of individual neurons. Neurons in the mouse V1 binocular zone shift their preference toward the ipsilateral eye if the contralateral eye is

occluded during the critical period, causing increased binocularity as measured by ocular dominance (OD) (Drager, 1975; Wagor et al., 1980; Gordon and Stryker, 1996; Hanover et al., 1999; Tagawa et al., 2005; Mrsic-Flogel et al., 2007; Hofer et al., 2009). We assessed how this increased binocularity in feedforward input transforms ocular integration as measured by binocular disparity selectivity using dichoptic stimulation of mouse V1 neurons in the binocular zone (Scholl et al., 2013a; Scholl et al., 2015). We hypothesized two possible outcomes: increased disparity tuning from enhancement of non-deprived excitatory inputs, maintenance of disparity tuning through proportional changes between each eye (e.g. no change), or decreased tuning resulting from non-deprived eye inputs with mismatched spatial-temporal profiles. Using two-photon calcium imaging we measured OD and the disparity selectivity index (DSI) in populations of neurons from normal, deprived animals, and normal pre-critical period (CP) animals. Increased binocularity, evident in an OD shift, was monocular deprivation (MD). Further, neurons receiving input from the ipsilateral (non-deprived) eye displayed the greatest loss of selectivity, and a loss of spatial resolution or high spatial frequency cutoff. In comparing pre- and post-CP animals we observe no difference in DSI distributions, demonstrating that MD was not impairing normal development of disparity selectivity. Our data suggest OD plasticity mediated enhancement of binocularity drives a misalignment of synaptic inputs from the two eyes disrupting existing binocular integration accompanied by a decrease in DSI in animals that underwent contralateral (Fig. 4.7).

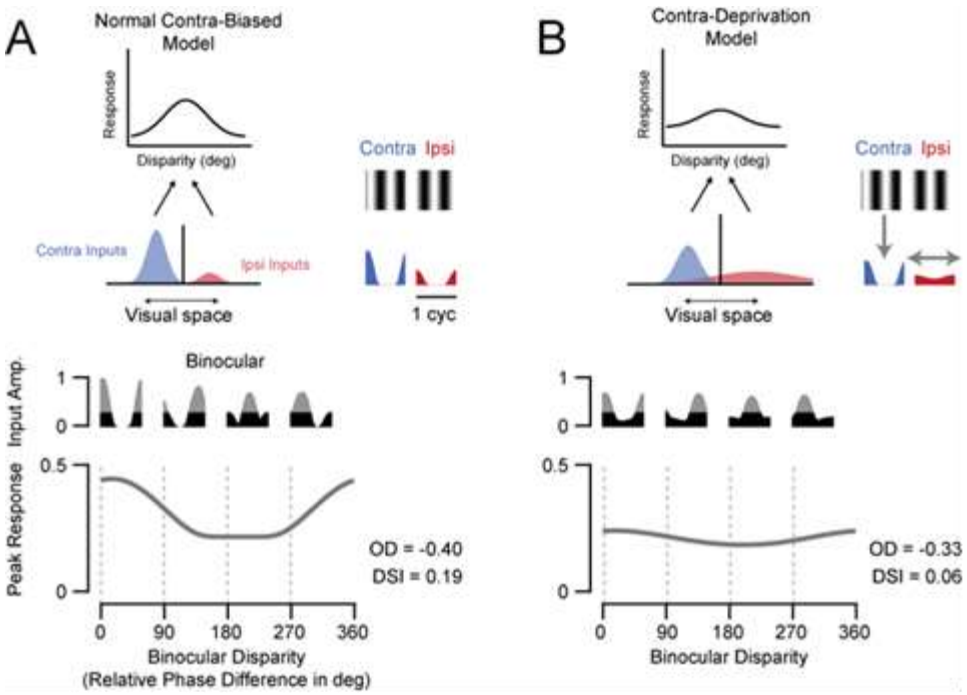

Figure 4.7: Monocular deprivation can drive decreased disparity selectivity through requirement of nonfunctional ipsilateral inputs.

(a) Model of a normal, contra-biased neuron. An individual cortical neuron receives inputs from monocular thalamic relay cells with distinct spatial preferences (top left). The aggregate thalamic afferent responses to drifting gratings presented to the left and right eye are shown to the right. This neuron has spatially disparate receptive fields for left and right eyes, so the grating phases that maximally drive the monocular thalamic inputs are distinct. These monocular thalamic afferents are then used to construct the binocular responses for the disparity conditions shown below. Suprathreshold binocular responses result from rectification of those subthreshold inputs (gray). Peak (F1 + DC) suprathreshold binocular responses are shown in the plot below (gray line). (b) Model predictions for changes following contralateral eye deprivation. As in a, a cortical neuron receives inputs from monocular relay cells. The ipsilateral eye inputs span a broader spatial extent, which disrupts the alignment required for disparity selectivity. The spatial extent of the ipsilateral eye inputs decreases the modulation to an ipsilateral grating and the weaker contralateral eye input decreases the modulation to a contralateral grating (top, right). Both of these effects lead to weaker disparity selectivity in the target cortical neuron (bottom).

How can we reconcile the paradoxical increase in the population of neurons receiving input from both eyes with decreased disparity selectivity? We propose that the specificity of spatial inputs coming from each eye is disrupted, and that this disruption leads to a decrease in disparity selectivity. It is known that MD causes changes in the synaptic connectivity within V1, and those changes could lead to a reduction in the spatial alignment responsible for disparity selectivity. Contralateral MD should increase the number of ipsilateral eye inputs projecting to individual neurons, but their spatial receptive field may be distinct. Therefore, the overall ipsilateral receptive field may be more diffuse in visual space following MD. To gain insight into how a change in the receptive field would impact disparity tuning, we constructed a simple model of a disparity selective mouse V1 neuron biased for the contralateral eye (Fig. 4.7, see Methods). Inputs from the two eyes were generated from two distinct populations of simple (phase selective) cells. Summing monocular responses across interocular phase differences (following our experiments) shows that the greatest binocular responses occur near the optimal disparity (0 deg in this case, Fig. 4.7A, top). Rectifying the summed monocular input further enhances the disparity selectivity in this model neuron (Fig. 4.7A, bottom). We then simulated how MD would change disparity selectivity in this model neuron by (1) decreasing the cells contributing to the contralateral input of inputs, (2) increasing the number of cells contributing to the ipsilateral input, and (3) additional cells contributing to ipsilateral input were drawn from a broader distribution of spatial preferences (e.g. phase selectivity here). Binocular responses from the convergence of these

two inputs showed less modulation across interocular phase differences both in subthreshold input and rectified responses (Fig. 4.7B).

Several predictions fall out of this simple model. First, as described above, disparity selectivity decreases, as measured by binocular gratings with interocular phase differences. This predicted decrease captures our observations of calcium responses from deprived mouse V1 neurons. Second, neuronal responses become more binocular following MD, which is also shown in our data. Third, binocular responses decrease following MD. This aspect of the model fails to capture our measurements, where we found the response amplitude at the preferred disparity was no different between normal and deprived, particularly in OD groups susceptible to MD (Fig. 4.5). Possible mechanisms which could account for this discrepancy include homeostatic mechanisms such as changes in the synaptic drive from other neurons, or intrinsic changes in excitability of the neurons (Mrsic-Flogel et al., 2007; Turrigiano, 2011). Finally, this model predicts that the ipsilateral spatial receptive field of mouse V1 binocular neurons should be diffuse, as ipsilateral synaptic input would be pooled from presynaptic neurons with a broad range of spatial location preferences. Such a shift toward larger receptive fields is also consistent with the observed decline in acuity associated with MD (Fagiolini et al., 1994; Prusky and Douglas, 2003; He et al., 2007).

Disparity selectivity, like orientation and direction selectivity, appears to be another receptive field property emerging early in development (Chino et al.,

1997; Feller and Scanziani, 2005; White and Fitzpatrick, 2007), as we find little or no difference between pre-CP and post-CP animals (Fig. 4.3). It is currently not known how early binocular disparity selectivity emerges or the exact role visual experience plays in sculpting its formation, although recent work from Gu and Cang (2016) suggests binocular matching feed-forward thalamic input onto individual neurons in pre-CP animals could provide the necessary signals(Gu and Cang, 2016). In carnivores and primates little or no disparity sensitivity is found shortly after eye opening, but this selectivity is enhanced within a few weeks of visual experience (Pettigrew, 1974; Freeman and Ohzawa, 1992; Chino et al., 1997). Interestingly, newborn lambs do exhibit modest disparity selectivity (Ramachandran et al., 1977). Thus, it is possible that disparity selectivity is developed starting near eye opening in mice, and it is close to matured near the normal CP. A potential period of time for this maturation would be during the matching of orientation preference between the two eyes (P20-P23, (Wang et al., 2010; Sarnaik et al., 2014)). Our measurements were done at a slightly later age (P25-27) and may therefore miss the important developmental period for binocular integration in mouse V1.

In carnivores and primates, the effects of MD on binocularity, as assayed by ocular dominance or disparity selectivity, reflects shifts in the same direction. There are declines in both measurements: most neurons respond only to the open eye under monocular conditions and disparity selectivity is dramatically reduced (Sclar et al., 1986; Freeman and Ohzawa, 1988; Vorobyov et al., 2007). We took advantage that MD causes a paradoxical increase in binocularity by OD

in mice to determine whether these two functional properties are linked. We find that ocular dominance and disparity selectivity, two measures of binocularity, shift in opposite directions in mice indicating that these two properties are not linked. Previous developmental work in carnivores and primates has indicated that monocular deprivation affects ocular dominance and disparity selectivity to different degrees. In conditions of partial MD, in which some binocular experience is allowed every day, disparity selectivity strongly declines whereas the monocular responses of neurons, including contrast sensitivity and ocular dominance, are only mildly affected (Sakai et al., 2006; Schwarzkopf et al., 2007; Vorobyov et al., 2007).

The relationship between ocular dominance and disparity selectivity is important to guide ongoing efforts to recover normal stereopsis in people with amblyopia. Brief monocular deprivation in people increases the perceptual strength of the deprived eye (Lunghi et al., 2011; Zhou et al., 2013a; Zhou et al., 2013b) and the strength of evoked potentials associated with cortical processing (Lunghi et al., 2015). These results raise an important question of whether monocular deprivation, or partial occlusion, could be used in adults with amblyopia to assist a recovery of binocular function (Zhou et al., 2013c; Zhou et al., 2013b; Hess and Thompson, 2015). Indeed, Hess and colleagues have demonstrated that changes in the strength of input from the weak eye are possible with brief periods of deprivation in people with amblyopia. It is not clear, however, whether these changes in the input strength driven by deprivation will

induce the emergence of stereopsis, though strengthening the weakened eye may be the first step to recovering normal binocular function.

Chapter 5: Conclusion

Across the evolutionary tree, animals have evolved distinct nervous systems in response to their distinct evolutionary pressures and their respective lineages. Yet, in the early visual pathway across mammalian species, there are certain visual transformations that appear to be common. In face of the existing singularities in the circuit across different species, to what extent are the circuit mechanisms underlying these generic transformations preserved? In this dissertation, I have studied two such transformations in the mouse visual system, orientation selectivity and binocular disparity tuning.

In carnivores and primates, the basis for the emergence of orientation selectivity is the precise convergence of ON and OFF inputs to cortical cells. This leads to an emergence of orientation tuning at the junction of the thalamic inputs to the cortex. A fallout of such arrangement is the positional specificity in the receptive fields for these input layer cortical cells. The generation of spatial-invariant orientation selectivity happens at the next stage of processing. I have demonstrated that the mouse visual system may not follow the same rules, which I have highlighted in the main text. In chapter 2, I present an alternate model to explain the emergence of orientation selectivity in the mouse visual cortex. This model is based on the notion that random connectivity between feedforward thalamic and recurrent inputs can explain the emergence of orientation selectivity, to the degree that it exists in the mouse. A specific prediction of the model was that orientation preference for such cells would be dependent on the spatial frequency of the stimulus. I have used optical imaging and intracellular

recordings to test this prediction. I show evidence for spatial frequency dependence of orientation preference across mouse V1 cells. The degree of this dependence is weaker than suggested in the original model and that perhaps reflects the existence of connection specificity, also demonstrated by multiple studies. Our results highlight the intricacies of receptive fields in mouse V1, which stand out from the receptive field profiles in carnivores and primates. The observation of such distinct receptive fields suggests the existence of non-standard connectivity patterns in mouse visual pathway.

I then studied the basis for the next step of processing, generation of complex cells, in chapter 3. Using a combination of intracellular recordings and optogenetics, I have analyzed the input differences for mouse V1 cells with varying degrees of linearity. In contrast to the hierarchical connectivity scheme observed in cats and primates, here as well I observe distinct features in the mouse V1. We demonstrate that thalamic inputs in mice can also exhibit nonlinearity which is then inherited by the incident cortical cell. The complexity could arise from a convergence of orientation selective LGN cells observed in mice. We also evaluated the possibility of these orientation selective LGN inputs contributing to the orientation selective responses of V1 cells. This is a matter of some debate in the literature and our results favor the idea that orientation selective LGN cells guide the orientation selectivity of cortical V1 cells. From our current experiments, we do not know the basis for nonlinearity of LGN responses. There are multiple approaches to obtaining complex thalamic responses, such as by a convergence of ON-OFF type of LGN cells, or by a

convergence of orientation selective LGN cells similar to the hierarchical motif, or by a loss of precision in connectivity of LGN to V1 causing overlap in the ON and OFF subfields. Our current data suggests that nonlinear thalamic responses can be based on inputs from orientation selective as well as unselective cells, but to be able to tease apart these possibilities will require more experiments in the future.

I have explored another feature computation, binocular disparity selectivity. Circuits underlying computations of many visual features are not fully formed at birth and observing the development of selectivity of these features provides another approach to study these computations. In this study, we have used the distinctive contralateral bias of ocular dominance in the mouse to test whether ocular dominance and binocular disparity tuning are linked. Manipulating ocular dominance using monocular deprivation in cats and primates causes it to shift to being monocular. It also causes a loss of disparity tuning, but the loss could be due to a decrease in binocular inputs or loss of appropriate connectivity. Contralateral deprivation in the mouse causes a paradoxical increase in binocularity and we used that to study the effect on disparity tuning. We found that the increase in binocularity caused a decrease in disparity tuning. This may be due to a change in the pattern of inputs following deprivation that is not able to maintain the structure needed for disparity tuning. This disruption is likely caused by the new inputs from open eye forming following deprivation, which may not be guided by binocular sensory experience. Our results showing a loss of spatial resolution in the open eye inputs support this idea.

The canonical circuit computation models for visual features often involve a single set of rules that define the specific connectivity between different cell groups. In the mouse visual system, is there such a single set of rules to achieve feature tuning? It appears to not be the case. One major contributing factor for this seems to be the diversity in the response profiles of cells, starting from the first stage of visual processing, in the retina. There is a great deal of functional diversity in the mouse retinal ganglion cells. While some of this diversity also exists in the primate retina, the primate retina is largely dominated by responses from midget and parasol ganglion cells. Perhaps a consequence of the mouse retinal ganglion cell diversity is a diversity in the responses of LGN cells. LGN neurons show a higher degree of orientation and direction selectivity and can show nonlinear spatial summation. A consequence of this diversity may be that there are multiple approaches to arrive at a given feature selectivity. Orientation selectivity, for example, can be inherited from the retinal ganglion cells, or generated following the hierarchical model scheme, or through random connections, or a combination of some of these approaches. Similarly, nonlinear spatial summation could emerge as suggested in the hierarchical model by Hubel and Wiesel or be due to a combination of inputs from ON-OFF cells or be a combination of multiple of these options. Rather than having few and distinct channels of information, the system appears to be relying on many intermingled ways to obtain selectivity.

It is also imperative to point out that in light of the above messy picture, there are certain aspects of the computation that are precise. It is for example remarkable that the recurrent inputs in cells are matched to the orientation preference and phase preference of the thalamic input, even as the thalamic input only contributes one third of the total inputs to the cells. Our results comparing the orientation preference between the tuned mean and modulated components of the thalamic responses also show a high correlation. Our results on the effects of MD on binocular disparity selectivity also demonstrate that a specificity between left and right eye inputs that is required for cells to be disparity selective. The system is clearly capable of achieving precision in these cases.

The mouse visual pathway has evolved in response to its own evolutionary pressures from the substrate of its evolutionary heritage. The incoming diversity of retinal inputs, either an inheritance or evolved response, is a feature the system has developed to manage. There is also a diversity in the responses of V1 responses with cells exhibiting many high order visual functions. This is perhaps due to a lack of extensive and elaborate extrastriate network of visual areas observed in primates leading to collapse of the processing stages into a single or a smaller set of regions. Given these specific constraints, it may then not be surprising that the emergent cortical computations in carnivores and primates have already emerged prior to the cortex in the mouse. It is likely that as more species across the mammalian evolutionary tree are studied, we will

discover more animals with their distinct constraints and the resultant differences in the visual system.

References

Alonso JM, Martinez LM (1998) Functional connectivity between simple cells and complex cells in cat striate cortex. Nat Neurosci 1:395-403.

Alonso JM, Usrey WM, Reid RC (2001) Rules of connectivity between geniculate cells and simple cells in cat primary visual cortex. J Neurosci 21:4002-4015.

Ayzenshtat I, Jackson J, Yuste R (2016) Orientation Tuning Depends on Spatial Frequency in Mouse Visual Cortex. eNeuro 3.

Baden T, Berens P, Franke K, Roman Roson M, Bethge M, Euler T (2016) The functional diversity of retinal ganglion cells in the mouse. Nature 529:345-350.

Bar-Yosef O, Nelken I (2007) The effects of background noise on the neural responses to natural sounds in cat primary auditory cortex. Frontiers in computational neuroscience 1:3.

Bosking WH, Zhang Y, Schofield B, Fitzpatrick D (1997) Orientation selectivity and the arrangement of horizontal connections in tree shrew striate cortex. J Neurosci 17:2112-2127.

Brainard DH (1997) The Psychophysics Toolbox. Spatial Vision 10:443-446.

Bullier J, Mustari MJ, Henry GH (1982) Receptive-field transformations between LGN neurons and S-cells of cat- striate cortex. J Neurophysiol 47:417-438.

Cang J, Kalatsky VA, Lowel S, Stryker MP (2005) Optical imaging of the intrinsic signal as a measure of cortical plasticity in the mouse. Vis Neurosci 22:685-691.

Carandini M, Ferster D (2000) Membrane potential and firing rate in cat primary visual cortex. J Neurosci 20:470-484.

Chance FS, Nelson SB, Abbott LF (1999) Complex cells as cortically amplified simple cells. Nat Neurosci 2:277-282.

Chino YM, Smith EL, 3rd, Hatta S, Cheng H (1997) Postnatal development of binocular disparity sensitivity in neurons of the primate visual cortex. J Neurosci 17:296-307.

Cossell L, Iacaruso MF, Muir DR, Houlton R, Sader EN, Ko H, Hofer SB, Mrsic-Flogel TD (2015) Functional organization of excitatory synaptic strength in primary visual cortex. Nature 518:399-403.

Cruz-Martin A, El-Danaf RN, Osakada F, Sriram B, Dhande OS, Nguyen PL, Callaway EM, Ghosh A, Huberman AD (2014) A dedicated circuit links direction-selective retinal ganglion cells to the primary visual cortex. Nature 507:358-361.

Cumming BG, Parker AJ (1999) Binocular neurons in V1 of awake monkeys are selective for absolute, not relative, disparity. J Neurosci 19:5602-5618.

Daniels JD, Norman JL, Pettigrew JD (1977) Biases for oriented moving bars in lateral geniculate nucleus neurons of normal and stripe-reared cats. Exp Brain Res 29:155-172.

De Valois RL, Albrecht DG, Thorell LG (1982) Spatial frequency selectivity of cells in macaque visual cortex. Vision Res 22:545-559.

DeAngelis GC, Ohzawa I, Freeman RD (1993) Spatiotemporal organization of simple-cell receptive fields in the cat's striate cortex. II. Linearity of temporal and spatial summation. J Neurophysiol 69:1118-1135.

DeAngelis GC, Ohzawa I, Freeman RD (1995) Neuronal mechanisms underlying stereopsis: how do simple cells in the visual cortex encode binocular disparity? Perception 24:3-31.

Drager UC (1975) Receptive fields of single cells and topography in mouse visual cortex. J Comp Neurol 160:269-290.

Drager UC, Hubel DH (1975) Responses to visual stimulation and relationship between visual, auditory, and somatosensory inputs in mouse superior colliculus. J Neurophysiol 38:690-713.

Enroth-Cugell C, Robson JG (1966) The contrast sensitivity of retinal ganglion cells of the cat. J Physiol (Lond) 187:517-552.

Espinosa JS, Stryker MP (2012) Development and plasticity of the primary visual cortex. Neuron 75:230-249.

Fagiolini M, Pizzorusso T, Berardi N, Domenici L, Maffei L (1994) Functional postnatal development of the rat primary visual cortex and the role of visual experience: dark rearing and monocular deprivation. Vision Res 34:709-720.

Feller MB, Scanziani M (2005) A precritical period for plasticity in visual cortex. Curr Opin Neurobiol 15:94-100.

Ferster D, Lindström S (1983) An intracellular analysis of geniculocortical connectivity in area 17 of the cat. J Physiol (Lond) 342:181-215.

Freeman RD, Ohzawa I (1988) Monocularly deprived cats: Binocular tests of cortical cells reveal functional connections from the deprived eye. J Neurosci 8:2491-2506.

Freeman RD, Ohzawa I (1992) Development of binocular vision in the kitten's striate cortex. J Neurosci 12:4721-4736.

Garaschuk O, Milos RI, Konnerth A (2006) Targeted bulk-loading of fluorescent indicators for two-photon brain imaging in vivo. Nat Protoc 1:380-386.

Girman SV, Sauve Y, Lund RD (1999) Receptive field properties of single neurons in rat primary visual cortex. J Neurophysiol 82:301-311.

Golshani P, Portera-Cailliau C (2008) In vivo 2-photon calcium imaging in layer 2/3 of mice. J Vis Exp.

Gordon JA, Stryker MP (1996) Experience-dependent plasticity of binocular responses in the primary visual cortex of the mouse. J Neurosci 16:3274-3286.

Gu Y, Cang J (2016) Binocular matching of thalamocortical and intracortical circuits in the mouse visual cortex. eLife 5.

Hammond P, Pomfrett CJ (1990) Influence of spatial frequency on tuning and bias for orientation and direction in the cat's striate cortex. Vision Res 30:359-369.

Hanover JL, Huang ZJ, Tonegawa S, Stryker MP (1999) Brain-derived neurotrophic factor overexpression induces precocious critical period in mouse visual cortex. J Neurosci 19:RC40.

Hansel D, van Vreeswijk C (2012) The mechanism of orientation selectivity in primary visual cortex without a functional map. J Neurosci 32:4049-4064.

Hawken MJ, Parker AJ (1987) Spatial properties of neurons in the monkey striate cortex. Proc R Soc Lond B Biol Sci 231:251-288.

He HY, Ray B, Dennis K, Quinlan EM (2007) Experience-dependent recovery of vision following chronic deprivation amblyopia. Nat Neurosci 10:1134-1136.

Heimel JA, Van Hooser SD, Nelson SB (2005) Laminar organization of response properties in primary visual cortex of the gray squirrel (Sciurus carolinensis). J Neurophysiol 94:3538-3554.

Hess RF, Thompson B (2015) Amblyopia and the binocular approach to its therapy. Vision Res 114:4-16.

Hillier D, Fiscella M, Drinnenberg A, Trenholm S, Rompani SB, Raics Z, Katona G, Juettner J, Hierlemann A, Rozsa B, Roska B (2017) Causal evidence

for retina-dependent and -independent visual motion computations in mouse cortex. Nat Neurosci 20:960-968.

Hirsch JA (1992) The first stage of synaptic integration in striate cortex. Soc Neurosci Abstr 18:209.

Hirsch JA, Alonso JM, Reid RC, Martinez LM (1998) Synaptic integration in striate cortical simple cells. J Neurosci 18:9517-9528.

Hochstein S, Shapley RM (1976) Quantitative analysis of retinal ganglion cell classifications. J Physiol (Lond) 262:237-264.

Hofer SB, Mrsic-Flogel TD, Bonhoeffer T, Hubener M (2009) Experience leaves a lasting structural trace in cortical circuits. Nature 457:313-317.

Howarth M, Walmsley L, Brown TM (2014) Binocular integration in the mouse lateral geniculate nuclei. Curr Biol 24:1241-1247.

Hubel D, Wiesel TN (1961) Integrative action in the cat's lateral geniculate body. J Physiol (Lond) 155:385-398.

Hubel DH, Wiesel TN (1962) Receptive fields, binocular interaction and functional architecture in the cat's visual cortex. J Physiol (Lond) 160:106-154.

Hubel DH, Wiesel TN (1970) The period of susceptibility to the physiological effects of unilateral eye closure in kittens. J Physiol 206:419-436.

Hubel DH, Wiesel TN (1977) Functional architecture of macaque visual cortex. Proc R Soc London Ser B 198:1-59.

Hubel DH, Wiesel TN, LeVay S (1977) Plasticity of ocular dominance columns in monkey striate cortex. Philos Trans R Soc Lond B Biol Sci 278:377-409.

Jin J, Wang Y, Swadlow HA, Alonso JM (2011) Population receptive fields of ON and OFF thalamic inputs to an orientation column in visual cortex. Nat Neurosci 14:232-238.

Jones JP, Palmer LA (1987) The two-dimensional spatial structure of simple receptive fields in cat striate cortex. J Neurophysiol 58:1187-1211.

Jones JP, Stepnoski A, Palmer LA (1987) The two-dimensional spectral structure of simple receptive fields in cat striate cortex. J Neurophysiol 58:1212-1232.

Joshua DE, Bishop PO (1970) Binocular single vision and depth discrimination. Receptive field disparities for central and peripheral vision and binocular interaction on peripheral single units in cat striate cortex. Exp Brain Res 10:389-416.

Julesz B (1971) Foundations of Cyclopean Perception. Chicago: Univ. Chicago Press.

Kalatsky VA, Stryker MP (2003) New paradigm for optical imaging: temporally encoded maps of intrinsic signal. Neuron 38:529-545.

Kameyama K, Sohya K, Ebina T, Fukuda A, Yanagawa Y, Tsumoto T (2010) Difference in binocularity and ocular dominance plasticity between GABAergic and excitatory cortical neurons. J Neurosci 30:1551-1559.

Kara P, Boyd JD (2009) A micro-architecture for binocular disparity and ocular dominance in visual cortex. Nature 458:627-631.

Katz LC, Crowley JC (2002) Development of cortical circuits: lessons from ocular dominance columns. Nat Rev Neurosci 3:34-42.

Kerr JN, Greenberg D, Helmchen F (2005) Imaging input and output of neocortical networks in vivo. Proc Natl Acad Sci U S A 102:14063-14068.

Ko H, Hofer SB, Pichler B, Buchanan KA, Sjostrom PJ, Mrsic-Flogel TD (2011) Functional specificity of local synaptic connections in neocortical networks. Nature 473:87-91.

Ko H, Cossell L, Baragli C, Antolik J, Clopath C, Hofer SB, Mrsic-Flogel TD (2013) The emergence of functional microcircuits in visual cortex. Nature 496:96-100.

Kondo S, Ohki K (2016) Laminar differences in the orientation selectivity of geniculate afferents in mouse primary visual cortex. Nat Neurosci 19:316-319.

Kremkow J, Jin J, Wang Y, Alonso JM (2016) Principles underlying sensory map topography in primary visual cortex. Nature 533:52-57.

Kuffler SW (1953) Discharge patterns and functional organization of mammalian retina. J Neurophysiol 16:37-68.

Kuhlman SJ, Tring E, Trachtenberg JT (2011) Fast-spiking interneurons have an initial orientation bias that is lost with vision. Nat Neurosci 14:1121-1123.

Lee BB, Creutzfeldt OD, Elepfandt A (1979) The responses of magno- and parvocellular cells of the monkey's lateral geniculate body to moving stimuli. Exp Brain Res 35:547-557.

Lee KS, Huang X, Fitzpatrick D (2016a) Topology of ON and OFF inputs in visual cortex enables an invariant columnar architecture. Nature 533:90-94.

Lee WC, Bonin V, Reed M, Graham BJ, Hood G, Glattfelder K, Reid RC (2016b) Anatomy and function of an excitatory network in the visual cortex. Nature 532:370-374.

LeVay S, Voigt T (1988) Ocular dominance and disparity coding in cat visual cortex. Vis Neurosci 1:395-414.

Li YT, Ibrahim LA, Liu BH, Zhang LI, Tao HW (2013) Linear transformation of thalamocortical input by intracortical excitation. Nat Neurosci 16:1324-1330.

Lien AD, Scanziani M (2013) Tuned thalamic excitation is amplified by visual cortical circuits. Nat Neurosci 16:1315-1323.

Lien AD, Scanziani M (2018) Cortical direction selectivity emerges at convergence of thalamic synapses. Nature 558:80-86.

Liu BH, Li P, Sun YJ, Li YT, Zhang LI, Tao HW (2010) Intervening inhibition underlies simple-cell receptive field structure in visual cortex. Nat Neurosci 13:89-96.

Longordo F, To MS, Ikeda K, Stuart GJ (2013) Sublinear integration underlies binocular processing in primary visual cortex. Nat Neurosci 16:714-723.

Lunghi C, Burr DC, Morrone C (2011) Brief periods of monocular deprivation disrupt ocular balance in human adult visual cortex. Curr Biol 21:R538-539.

Lunghi C, Emir UE, Morrone MC, Bridge H (2015) Short-Term Monocular Deprivation Alters GABA in the Adult Human Visual Cortex. Curr Biol 25:1496-1501.

Malone BJ, Ringach DL (2008) Dynamics of tuning in the Fourier domain. J Neurophysiol 100:239-248.

Martinez LM, Alonso JM (2001) Construction of complex receptive fields in cat primary visual cortex. Neuron 32:515-525.

Martinez LM, Wang Q, Reid RC, Pillai C, Alonso JM, Sommer FT, Hirsch JA (2005) Receptive field structure varies with layer in the primary visual cortex. Nat Neurosci 8:372-379.

Mechler F, Ringach DL (2002) On the classification of simple and complex cells. Vision Res 42:1017-1033.

Metin C, Godement P, Imbert M (1988) The primary visual cortex in the mouse: receptive field properties and functional organization. Exp Brain Res 69:594-612.

Miller KD (2016) Canonical computations of cerebral cortex. Curr Opin Neurobiol 37:75-84.

Movshon JA, Thompson ID, Tolhurst DJ (1978a) Spatial and temporal contrast sensitivity of neurones in areas 17 and 18 of the cat's visual cortex. J Physiol (Lond) 283:101-120.

Movshon JA, Thompson ID, Tolhurst DJ (1978b) Spatial summation in the receptive fields of simple cells in the cat's striate cortex. Journal of Physiology (London) 283:53-77.

Mrsic-Flogel TD, Hofer SB, Ohki K, Reid RC, Bonhoeffer T, Hubener M (2007) Homeostatic regulation of eye-specific responses in visual cortex during ocular dominance plasticity. Neuron 54:961-972.

Murphy EH, Berman N (1979) The rabbit and the cat: a comparison of some features of response properties of single cells in the primary visual cortex. J Comp Neurol 188:401-427.

Nauhaus I, Nielsen KJ, Callaway EM (2012) Nonlinearity of two-photon Ca2+ imaging yields distorted measurements of tuning for V1 neuronal populations. J Neurophysiol 107:923-936.

Niell CM, Stryker MP (2008) Highly selective receptive fields in mouse visual cortex. J Neurosci 28:7520-7536.

Ohki K, Reid RC (2007) Specificity and randomness in the visual cortex. Curr Opin Neurobiol 17:401-407.

Ohki K, Chung S, Ch'ng YH, Kara P, Reid RC (2005) Functional imaging with cellular resolution reveals precise micro-architecture in visual cortex. Nature 433:597-603.

Ohzawa I, Freeman RD (1986) The binocular organization of simple cells in the cat's visual cortex. J Neurophysiol 56:221-242.

Pattadkal JJ, Mato G, Van Vreeswijk C, Priebe NJ, Hansel D (2018) Emergent Orientation Selectivity from Random Networks in Visual Cortex. Cell Reports 24:2042-2050.

Pehlevan C, Sompolinsky H (2014) Selectivity and sparseness in randomly connected balanced networks. PLoS One 9:e89992.

Pelli DG (1997) The VideoToolbox software for visual psychophysics: transforming numbers into movies. Spat Vis 10:437-442.

Pettigrew JD (1974) The effect of visual experience on the development of stimulus specificity by kitten cortical neurones. J Physiol 237:49-74.

Pettigrew JD, Nikara T, Bishop PO (1968) Binocular interaction on single units in cat striate cortex: simultaneous stimulation by single moving slit with receptive fields in correspondence. Exp Brain Res 6:391-410.

Piscopo DM, El-Danaf RN, Huberman AD, Niell CM (2013) Diverse visual features encoded in mouse lateral geniculate nucleus. J Neurosci 33:4642-4656.

Poggio GF, Fischer B (1977) Binocular interaction and depth sensitivity in striate and prestriate cortex of behaving rhesus monkey. J Neurophysiol 40:1392-1405.

Press WH (1992) Numerical recipes in C : the art of scientific computing, 2nd Edition. Cambridge ; New York: Cambridge University Press.

Priebe NJ (2008) The relationship between subthreshold and suprathreshold ocular dominance in cat primary visual cortex. J Neurosci 28:8553-8559.

Priebe NJ, Ferster D (2012) Mechanisms of neuronal computation in mammalian visual cortex. Neuron 75:194-208.

Priebe NJ, Mechler F, Carandini M, Ferster D (2004) The contribution of spike threshold to the dichotomy of cortical simple and complex cells. Nat Neurosci 7:1113-1122.

Prusky GT, Douglas RM (2003) Developmental plasticity of mouse visual acuity. Eur J Neurosci 17:167-173.

Ramachandran VS, Clarke PG, Whitteridge D (1977) Cells selective to binocular disparity in the cortex of newborn lambs. Nature 268:333-335.

Reid RC, Alonso JM (1995) Specificity of monosynaptic connections from thalamus to visual cortex. Nature 378:281-284.

Reyes A, Sakmann B (1999) Developmental switch in the short-term modification of unitary EPSPs evoked in layer 2/3 and layer 5 pyramidal neurons of rat neocortex. J Neurosci 19:3827-3835.

Ringach DL (2004) Haphazard wiring of simple receptive fields and orientation columns in visual cortex. J Neurophysiol 92:468-476.

Ringach DL, Shapley RM, Hawken MJ (2002) Orientation selectivity in macaque V1: diversity and laminar dependence. J Neurosci 22:5639-5651.

Ringach DL, Mineault PJ, Tring E, Olivas ND, Garcia-Junco-Clemente P, Trachtenberg JT (2016) Spatial clustering of tuning in mouse primary visual cortex. Nat Commun 7:12270.

Sakai E, Bi H, Maruko I, Zhang B, Zheng J, Wensveen J, Harwerth RS, Smith EL, 3rd, Chino YM (2006) Cortical effects of brief daily periods of unrestricted vision during early monocular form deprivation. J Neurophysiol 95:2856-2865.

Sanes JR, Masland RH (2015) The types of retinal ganglion cells: current status and implications for neuronal classification. Annu Rev Neurosci 38:221-246.

Sarnaik R, Chen H, Liu X, Cang J (2014) Genetic disruption of the On visual pathway affects cortical orientation selectivity and contrast sensitivity in mice. J Neurophysiol 111:2276-2286.

Scholl B, Burge J, Priebe NJ (2013a) Binocular integration and disparity selectivity in mouse primary visual cortex. J Neurophysiol 109:3013-3024.

Scholl B, Tan AY, Priebe NJ (2013b) Strabismus disrupts binocular synaptic integration in primary visual cortex. J Neurosci 33:17108-17122.

Scholl B, Tan AY, Corey J, Priebe NJ (2013c) Emergence of orientation selectivity in the Mammalian visual pathway. J Neurosci 33:10616-10624.

Scholl B, Pattadkal JJ, Rowe A, Priebe NJ (2016) Functional characterization and spatial clustering of visual cortical neurons in the predatory grasshopper mouse Onychomys arenicola. J Neurophysiol:jn 00779 02016.

Scholl B, Pattadkal JJ, Dilly GA, Priebe NJ, Zemelman BV (2015) Local Integration Accounts for Weak Selectivity of Mouse Neocortical Parvalbumin Interneurons. Neuron 87:424-436.

Scholl B*, Pattadkal JJ*, Priebe NJ, (2017) Binocular Disparity Selectivity Weakened after Monocular Deprivation in Mouse V1. J Neurosci 37:6517-6526.

Scholl B, Rylee J, Luci JJ, Priebe NJ, Padberg J (2017) Orientation selectivity in the visual cortex of the nine-banded armadillo. J Neurophysiol:jn 00851 02016.

Schwarzkopf DS, Vorobyov V, Mitchell DE, Sengpiel F (2007) Brief daily binocular vision prevents monocular deprivation effects in visual cortex. Eur J Neurosci 25:270-280.

Sclar G, Ohzawa I, Freeman RD (1986) Binocular summation in normal, monocularly deprived, and strabismic cats: visual evoked potentials. Exp Brain Res 62:1-10.

Shapley R, Hochstein S (1975) Visual spatial summation in two classes of geniculate cells. Nature 256:411-413.

Skottun BC, De Valois RL, Grosof DH, Movshon JA, Albrecht DG, Bonds AB (1991) Classifying simple and complex cells on the basis of response modulation. Vision Res 31:1079-1086.

Song S, Sjostrom PJ, Reigl M, Nelson S, Chklovskii DB (2005) Highly nonrandom features of synaptic connectivity in local cortical circuits. PLoS Biol 3:e68.

Soodak RE (1987) The retinal ganglion cell mosaic defines orientation columns in striate cortex. Proc Natl Acad Sci U S A 84:3936-3940.

Stosiek C, Garaschuk O, Holthoff K, Konnerth A (2003) In vivo two-photon calcium imaging of neuronal networks. Proc Natl Acad Sci U S A 100:7319-7324.

Sun W, Tan Z, Mensh BD, Ji N (2016) Thalamus provides layer 4 of primary visual cortex with orientation- and direction-tuned inputs. Nat Neurosci 19:308-315.

Suresh V, Ciftcioglu UM, Wang X, Lala BM, Ding KR, Smith WA, Sommer FT, Hirsch JA (2016) Synaptic Contributions to Receptive Field Structure and Response Properties in the Rodent Lateral Geniculate Nucleus of the Thalamus. J Neurosci 36:10949-10963.

Tagawa Y, Kanold PO, Majdan M, Shatz CJ (2005) Multiple periods of functional ocular dominance plasticity in mouse visual cortex. Nat Neurosci 8:380-388.

Tan AY, Brown BD, Scholl B, Mohanty D, Priebe NJ (2011) Orientation selectivity of synaptic input to neurons in mouse and cat primary visual cortex. J Neurosci 31:12339-12350.

Tan AY, Chen Y, Scholl B, Seidemann E, Priebe NJ (2014) Sensory stimulation shifts visual cortex from synchronous to asynchronous states. Nature 509:226-229.

Tao L, Shelley M, McLaughlin D, Shapley R (2004) An egalitarian network model for the emergence of simple and complex cells in visual cortex. Proc Natl Acad Sci U S A 101:366-371.

Turrigiano G (2011) Too many cooks? Intrinsic and synaptic homeostatic mechanisms in cortical circuit refinement. Annu Rev Neurosci 34:89-103.

Uka T, DeAngelis GC (2004) Contribution of area MT to stereoscopic depth perception: choice-related response modulations reflect task strategy. Neuron 42:297-310.

Van den Bergh G, Zhang B, Arckens L, Chino YM (2010) Receptive-field properties of V1 and V2 neurons in mice and macaque monkeys. J Comp Neurol 518:2051-2070.

Van Hooser SD, Roy A, Rhodes HJ, Culp JH, Fitzpatrick D (2013) Transformation of receptive field properties from lateral geniculate nucleus to superficial v1 in the tree shrew. J Neurosci 33:11494-11505.

van Vreeswijk C, Sompolinsky H (1996) Chaos in neuronal networks with balanced excitatory and inhibitory activity. Science 274:1724-1726.

van Vreeswijk C, Sompolinsky H (1998) Chaotic balanced state in a model of cortical circuits. Neural Comput 10:1321-1371.

von der Malsburg C (1973) Self-organization of orientation sensitive cells in the striate cortex. Kybernetik 14:85-100.

Vorobyov V, Schwarzkopf DS, Mitchell DE, Sengpiel F (2007) Monocular deprivation reduces reliability of visual cortical responses to binocular disparity stimuli. Eur J Neurosci 26:3553-3563.

Wagor E, Mangini NJ, Pearlman AL (1980) Retinotopic organization of striate and extrastriate visual cortex in the mouse. J Comp Neurol 193:187-202.

Wang BS, Sarnaik R, Cang J (2010) Critical period plasticity matches binocular orientation preference in the visual cortex. Neuron 65:246-256.

Wang X, Lu T, Snider RK, Liang L (2005) Sustained firing in auditory cortex evoked by preferred stimuli. Nature 435:341-346.

Wang XJ, Buzsaki G (1996) Gamma oscillation by synaptic inhibition in a hippocampal interneuronal network model. J Neurosci 16:6402-6413.

Webster MA, De Valois RL (1985) Relationship between spatial-frequency and orientation tuning of striate-cortex cells. J Opt Soc Am A 2:1124-1132.

White LE, Fitzpatrick D (2007) Vision and cortical map development. Neuron 56:327-338.

Wiesel TN, Hubel DH (1963a) Single cell responses in striate cortex of kittens deprived of vision in one eye. J Neurophysiol 26:1003-1017.

Wiesel TN, Hubel DH (1963b) Single-Cell Responses in Striate Cortex of Kittens Deprived of Vision in One Eye. J Neurophysiol 26:1003-1017.

Wiesel TN, Hubel DH (1965) Comparison of the effects of unilateral and bilateral eye closure on corticla unit responses in kittens. J Neurophysiol 28:1029-1040.

Wilson DE, Whitney DE, Scholl B, Fitzpatrick D (2016) Orientation selectivity and the functional clustering of synaptic inputs in primary visual cortex. Nat Neurosci 19:1003-1009.

Yunzab M, Choi V, Meffin H, Cloherty SL, Priebe NJ, Ibbotson MR (2019) Synaptic Basis for Contrast-Dependent Shifts in Functional Identity in Mouse V1. eNeuro 6.

Zhao X, Chen H, Liu X, Cang J (2013) Orientation-selective responses in the mouse lateral geniculate nucleus. J Neurosci 33:12751-12763.

Zhou J, Clavagnier S, Hess RF (2013a) Short-term monocular deprivation strengthens the patched eye's contribution to binocular combination. J Vis 13.

Zhou J, Thompson B, Hess RF (2013b) A new form of rapid binocular plasticity in adult with amblyopia. Scientific reports 3:2638.

Zhou J, Jia W, Huang CB, Hess RF (2013c) The effect of unilateral mean luminance on binocular combination in normal and amblyopic vision. Scientific reports 3:2012.